

Viscoelastic and Inertial Focusing of Asymmetric Cells in Spiral Channels

BY

HUA GAO

B.S., University of Cincinnati, Cincinnati, 2016

M.S., University of Cincinnati, Cincinnati, 2016

DISSERTATION

Submitted as partial fulfillment of the requirements
for the degree of Doctor of Philosophy in Biomedical Engineering
in the Graduate College of the
University of Illinois Chicago, 2022

Chicago, Illinois

Defense Committee:

Ian Papautsky, Chair and Advisor

David Eddington

Zhangli Peng

Jie Xu, Mechanical and Industrial Engineering

Gopakumar Kamalakshakurup, Genus PLC

I dedicate my dissertation work to my family, especially my parents Baoan Gao and Ping Miao, for being my first teachers and supporting me in study abroad. Their endless love and encouragement are the best gift I ever had.

I also dedicate my dissertation to my lovely wife Yiren Weng, who has stood by me through all my travails and impatience. Without her this work would not be made possible.

ACKNOWLEDGMENTS

First of all, I would like to express my sincerest gratitude to my advisor, Dr. Ian Papautsky, for his great guidance, patient, and encouragement throughout my Ph.D. studies. His passion and expertise for research has always influenced and inspired me to discover the root cause of this novel and interesting research field. Moreover, he is also a cheerful and gentle professor who always makes joyful and nurturing working environment for the lab and my personal development. Without his support and advice, this work would not have been possible.

I would also like to express my sincere thanks to my dissertation committee members, Dr. David Eddington, Dr. Gopakumar Kamalakshakurup, Dr. Zhangli Peng, and Dr. Jie Xu, for their support , guidance, and willingness to review my dissertation. Thanks for valuable and timely feedbacks at key stages in my prelim proposal, annual evaluation, and the dissertation defense.

A special thanks to Dr. Zhangli Peng and his student Moein Naderi for providing an excellent simulation model of particle migration in elasto-inertial fluids in spiral channel and contributions to our publication, “Evolution of Focused Streams in Viscoelastic Flow in Spiral Microchannels”, in *Microsystem and Nanoengineering*. Also, a special thanks to Dr. Gopakumar Kamalakshakurup from Genus PLC for providing an excellent project to collaborate on. It was a great opportunity to work along with him and learn from his industrial team, including Zheng Xia, and Wujun Zhao. I would like to acknowledge the financial support of University of Illinois Chicago, NSF/CADMIM (Center for Advanced Design and Manufacturing of Integrated

Microfluidics).

Many thanks to my lab mates and colleagues from the Papautsky's lab over these years, including Dr. Jian Zhou, Dr. Zhizhen Wu, Dr. Prithviraj Mukherjee, Elena Boselli, Dr. Zhehao Zhang, Qiyue Luan, and Celine Macaraniag. Especially, thanks to Dr. Jian Zhou and Dr. Prithviraj Mukherjee who provided me with fabrication techniques and experimental advisement whenever needed. I would like to express my thanks to students I have worked with Filippo Amadeo and Federico Nebuloni for their contributions on previous fabrication projects.

I would like to acknowledge the financial support of NSF Center for Advanced Design and Manufacturing of Integrated Microfluidics (NSF I/UCRC award IIP-1841473) and the UIC Center for Clinical and Translational Science (CCTS), which is supported by the National Center for Advancing Translational Sciences (NCATS).

Finally, I would like to express my deepest gratitude to my parents for their unconditional love, encourage and support. Their constant support gives me strength to achieve my dreams. Most importantly, I would like to thank my wife Yiren Weng. She is the most precious gift from God and most important person in my life. Her love, care and comfort always surround me and help me overcome every difficulty in life.

CONTRIBUTION OF AUTHORS

Chapters 2 include sections from a previously published review paper (Jian Zhou, Prithviraj Mukherjee, Hua Gao, Qiyue Luan, and Ian Papautsky. “Label-free microfluidic sorting of microparticles”. *APL Bioeng.* 3, 041504 (2019)). I contributed sections on viscoelastic separation, which are used in this document. Dr. Jian Zhou, Dr. Prithviraj Mukherjee, and Qiyue Luan wrote the remaining sections. Dr. Ian Papautsky was the senior author and edited the manuscript.

Chapter 3 contains results from an unpublished manuscript, in which Moein Naderi contributed simulations of Dean vortices. These results are presented in Figure 6-7 and 14a of this document.

TABLE OF CONTENTS

<u>CHAPTER</u>		<u>PAGE</u>
1.	INTRODUCTION	1
1.1.	Microfluidic Sorting Techniques	1
1.2.	Particle and Asymmetrical Cell Focusing.....	2
1.3.	Motivation.....	4
1.4.	Scope of Work	5
1.5.	Chapter Summaries	6
2.	BACKGROUND	8
2.1.	Viscoelastic Microfluidics	8
2.2.	Inertial Microfluidics	11
2.3.	Physical Mechanism and Hydraulic Forces.....	13
2.4.	Viscoelastic Focusing and Separation	20
2.5.	Viscoelastic Focusing and Separation with Dean Coupling	22
2.6.	Asymmetric Cell Sorting	24
2.7.	Summary	25
3.	EVOLUTION OF FOCUSED STREAMS IN VISCOELASTIC FLOW IN SPIRAL CHANNEL.....	26
3.1.	Introduction.....	26
3.2.	Experimental Methods	26
3.3.	Results and Discussion	33
3.4.	Summary	51
4.	ASYMMETRIC SPERM CELL DYNAMICS IN SPIRAL CHANNEL	53
4.1.	Introduction.....	53
4.2.	Experimental Methods	54
4.3.	Results and Discussion	60
4.4.	Summary	76
5.	CONCLUSIONS AND FUTURE WORK	78
5.1.	Summary	78
5.2.	Future Work	81
	REFERENCES	82
	APPENDIX.....	92
	VITA.....	95

LIST OF TABLES

<u>TABLE</u>		<u>PAGE</u>
I.	Rheological characteristics of Newtonian and non-Newtonian fluid	29
II.	Morphology parameters of bovine spermatozoa.....	60

LIST OF FIGURES

<u>FIGURE</u>	<u>PAGE</u>
1.	Viscoelastic focusing and sorting of particles. (a) Viscoelastic focusing creates a single equilibrium position along the central axis of a circular capillary. In square channels, there are (b) five focusing positions when flow is elasticity dominant and (c) a single position at the centerline when flow is elasto-inertial. (d) Size based sorting of particles using elasticity dominant flow in a device with a combination of circular and square cross-sections.10
2.	Inertial focusing in microchannels. (a) Two lift forces orthogonal to the flow direction act to equilibrate microparticles near the wall. The shear-induced lift force F_S is directed down the velocity gradient and drives particles toward channel walls. The wall-induced lift force F_W directs particles away from the walls and drives particles toward the channel centerline. The balance of these two lift forces causes particles to equilibrate. (b) Inertial focusing creates an annulus in cylindrical capillaries and four symmetric positions in square channels. In both cases, the equilibrium positions are approximately at $\sim 0.4Dh$ from the sidewall. (c) In a rectangular channel, there are two preferred equilibrium positions. A two-stage model describes inertial migration of microparticles first from the channel bulk toward equilibrium positions near long walls under the influence of F_{SG} and F_{WI} and then parallel to channel walls into wall-centered equilibrium positions under the influence of the rotation-induced lift force (F_Q). (d) Schematic of the spiral microparticle separator. The randomly dispersed particles equilibrate at different equilibrium positions along the inner wall of the spiral microchannel under the influence of F_L and F_D . Separation between individual particle streams is enhanced by opening the spiral channel into a wider straight channel before extracting the individual streams using a multiple outlet design. Microchannel cross-section illustrating effects of F_L and F_D on particles. The ratio of forces (F_L/F_D) is the determining factor in where a particle of given size (diameter) equilibrates.12
3.	Schematic of hydraulic forces in Newtonian and non-Newtonian flows. (a) Wall induced force. C_W is the coefficient of wall induced force, ρ is the fluid density, a is the particle diameter and D_h is the channel hydraulic diameter.(b) Shear gradient lift force. C_S is the coefficient of shear gradient lift force. (c) Dean drag force.(d) Elastic force. C_E is elastic lift coefficient. λ is the time of the fluid. ω is the width of the channel. Q is the flow rate.17

4. Viscoelastic microfluidics for particle sorting and other applications. (a) Separation of 1 μm and 5 μm diameter particles in a square co-flow microchannel using viscoelastic flow. (b) Three co-flow channels used for separation of 500 and 100 nm diameter particles, 1 μm and 2 μm diameter particles, and MCF-7 and blood cells. (c) Combination of viscoelastic flow and pinched flow fractionation (PFF) for size-based and shape-based particle separation. (d) Sheathless separation of particles in viscoelastic flow using a microchannel with round and square cross-sections. (e) Separation of malaria parasites from WBCs in a two-segment channel with a high aspect-ratio cross-section. (f) Particle filtration in a square microchannel using elastic and inertial forces. (g) Sheathless separation of particles and cells in viscoelastic flow. (h) Measurements of monitoring cell deformability using viscoelastic single-stream focusing. (i) DNA focusing in a rectangular channel based on elastic force and flexibility-induced force.21
5. Details of device design. (a) Schematic layout of spiral channel. (b) Table summarizing details of the four devices of different initial radii of curvature. Loop radius is given at position a for each device.27
6. Model mesh configuration. Finer mesh was used in the cross-section of interest.32
7. Dependency of simulation results on the number of mesh elements and the spiral segment length by plotting radial velocity along half the channel height. (a) three different mesh configurations with 15000, 126000, and 204000 number of elements were evaluated, and the mesh-independency was observed beyond 126K elements. (b) Segment lengths of $\pi/10$, $\pi/20$ and $\pi/40$ were simulated; channel length of $\pi/20$ ensured independence of the results from the domain length and provided longest possible channel segment for the flow to develop32
8. Downstream evolution of particle focusing. (a) Stacked fluorescent streak images illustrating downstream evolution of particle focusing in R2 spiral channel (aspect ratio $AR = 0.2$) at 50-350 $\mu\text{L}/\text{min}$ flow rate. The ± 125 scale indicates the normalized width of the 250 μm wide channel. Downstream position is indicated at the bottom of the panel set. (b) Heat map illustrates lateral migration of particles in R2 channel. Each cell reports focusing quality ($FQ = a/\text{FWHM}$) of fluorescent streams. The color of each cell indicates the unfocused (X), three streams (3), transition (T) or single stream (1) regions.35
9. Flow direction effects on particle lateral migration. Fluorescent streak images illustrating downstream evolution of particle focusing for opposite flow directions in R2 at (a) 100 $\mu\text{L}/\text{min}$ and (b) 250 $\mu\text{L}/\text{min}$. Downstream position label is at the bottom, while the corresponding Dean number (De) is at the top of each panel set. Device icons on left indicate flow direction. Lateral position of particle streams evolving downstream of the microchannel at (c) 100 $\mu\text{L}/\text{min}$ and (d) 250 $\mu\text{L}/\text{min}$ flows. Blue is the inner stream, red is the central stream, and yellow is the outer stream. Circles represent data for inside-out flow direction, while triangles

	represent data for outside-in flow direction.	38
10.	Vertical migration of particles. (a) Vertical position probability in R2 channel for particles flown inside-out at 50-250 $\mu\text{L}/\text{min}$. The particle vertical position is measured from the particle center to the bottom of the channel. Each plot corresponds to the particle vertical position probability based on $n=455$, $n=301$, $n=268$, and $n=291$ individual measurements, respectively. Inset illustrates a representative bright field image obtained using side view imaging at 150 $\mu\text{L}/\text{min}$. For flown outside-in, the vertical position of particle is not measurable due to the out range of microscope working distance and the reflection and refraction from adjacent channels. (b) Gap distance (d) between particle streams as a function of flow rate. Measurements of particle vertical positions as a function of downstream position at flow rates of (c) 100 $\mu\text{L}/\text{min}$ and (d) 250 $\mu\text{L}/\text{min}$. The vertical positions were measured from particle probability peaks from 100 individual measurements along the channel downstream length. The red, orange, and blue lines represent the particle position in the focal planes near the center, outer wall, and inner wall respectively. Due to channel deformation, empirical $\pm 2 \mu\text{m}$ systematical error bars added in (b), (c), and (d).	41
11.	Curvature effects on particle focusing. (a) Fluorescent images demonstrate particle trajectories in four devices (R1, R2, R4, and R6) at 8cm downstream in 500 ppm PEO at 50 - 350 $\mu\text{L}/\text{min}$. The flow parameters are at the top of each column. The corresponding De , which changes with curvature, is at the top of the fluorescent images. (b) Bar plots illustrating downstream migration distance to evolve three or one streams for 50 - 250 $\mu\text{L}/\text{min}$. Error bars indicate $\frac{1}{4}$ loop length from the observed position.	43
12.	Particle migration and focusing in R1, R2, R4, and R6. Heat map illustrates the evolution of particle focusing streams. Each cell reports focusing quality ($\text{FQ} = a/\text{FWHM}$) of fluorescent streams. The color of each cell indicates the unfocused (X), three stream (3), transition (T) or single stream (1) regions.	46
13.	Elasticity effects on particle focusing. (a) Fluorescent and bright-field images of particle focusing in 0 ppm, 500 ppm, and 5000 ppm PEO solutions observed at the outlet. (b) Single stream focusing lateral position as a function of elastic number. (c) Heat map illustrates evolution of particle focusing downstream the channel (indicated below) in varying PEO concentrations. In DI, DI +22% glycerin, and 50 ppm PEO, particles focus near the inner-half of the channel and progressively move toward inner-wall, illustrating inertial flow regime. In elasto-inertial flow regime, particles initially focus into three streams, then transition into two streams, and finally focus into a single stream. In viscoelastic flow regime, at 5000 ppm PEO, particles rapidly evolve into a single stream.	47
14.	Evolution of particle migration in elasto-inertial flow in spiral microchannel. Numerical results of the velocity fields of secondary flows due to Dean and elastic forces (left) and schematic diagram (right) illustrating positions of focused	

	particles and the force balance in R2 channel with aspect ratio $AR = 0.2$. Results are for low flow rate (100 $\mu\text{L}/\text{min}$) at (a) 3 cm, (b) 9 cm, and (c) Outlet downstream positions, as well as for high flow rate (250 $\mu\text{L}/\text{min}$) at (d) 3 cm, (e) 9 cm, and (f) Outlet downstream positions. Blue, red, and orange arrows indicate inertial lift FL , elastic force F_E , and drag force F_D , respectively. Only bottom half of the channel in the schematic is shown due to symmetry.....	50
15.	Downstream evolution of focusing for 7.32 μm , 15 μm , and 25 μm diameter beads. Stacked fluorescent streak images illustrating downstream evolution of particle focusing in R2 spiral channel (aspect ratio $AR = 0.2$) at 250 $\mu\text{L}/\text{min}$ flow rate in 500 ppm PEO solution. The +/-125 scale indicates the normalized width of the 250 μm wide channel. Downstream position is indicated at the bottom of the panel set.....	52
16.	Schematics of soft lithography. (a) master fabrication by align dry film on silicon substrate. (b) Top-view device fabrication by casing PDMS and oxygen plasma bonding on glass substrate. (c) Side-view device fabrication by bonding a flat PDMS and vertically cured inside of a Petri Dish.	57
17.	Bovine spermatozoa morphology. (a) Bright-field image of a bovine sperm cell in 100 \times magnification. The head major axis, minor axis, and tail length were measured by using CellSense software. (b) Schematic of the sperm head (c) Box plots of sperm head major and minor axis (d) size from Day 1 to Day 4 with $N=291$	59
18.	Live/Dead stain of sperm cells. (a) The live and (b) dead sperm cells were fluorescent labeled by Calcein AM and PI with green and red color respectively. (c) The composed image of live and dead.(d) Viability of the sperm cells at 60000 s^{-1} was not significantly lower than 0 s^{-1} ($n=3$). * $p < 0.05$	61
19.	Tail-off sperm cell preparation from raw spermatozoa. (a) Bright field image of the tail-off cells after isolation from microtip sonicator. (b) The corresponded fluorescent stain image. The isolation efficiency is $94.4\% \pm 3.2\%$ by measuring 1684 cells ($n=10$).	62
20.	Top view focusing dynamics of spherical particles and asymmetrical sperm cells. (a) Stacked fluorescent streak images illustrate spherical particles, tail-off cells, and sperm cells focusing dynamics at outlet. Teal and orange dash lines indicates the inner wall and outer wall of the channel. Spherical particles with diameters of 7.32 μm , and 2.01 μm labeled as green and 4.16 μm as red. The asymmetrical intact sperm cells and tail-off cells were labeled as blue. The left column indicates the flow rates of the experiments. The light blue and orange dash lines represent the inner wall and outer wall of the channel. (b) Measured fluorescent intensity profiles of sperm cells across the channel width at selected De from 0.77 to 10.26, clearly illustrating the lateral migration evolution. (c) Particles, tail-off cell, and sperm cell lateral migration as function of Dean number.....	65

21. Side-view focusing evolution of spherical particles and asymmetrical sperm cells. (a) Stacked fluorescent streak images illustrate spherical particles, tail-off cells, and sperm cells focusing dynamics at outlet. White dash lines labeled the channel top and bottom walls. (b) Vertical position as function of Dean number. The ± 12.5 indicates the normalized vertical position of the $25\text{ }\mu\text{m}$ channel height. (c) Gap distance of particles, tail-off cells, and sperm cells as a function of Dean number. The red, orange, teal, and dark blue represents the $7\text{ }\mu\text{m}$, $4\text{ }\mu\text{m}$, tail-off cell, and sperm cells respectively. Each point of the plots collected from a triple measurement at outlet. Due to channel deformation, empirical $\pm 2\text{ }\mu\text{m}$ systematical error bars added in (d).....69

22. Cells orientation distribution in spiral channel.(a) High-speed camera bright field image of sperm cell at $De \sim 5.13$ illustrate sperm cell orientation and schematic of the flat-on, edge-on, and misaligned orientations of sperm cells.(b) The sperm cell orientation distribution at range of Dean number.(c) Sperm cell and tal-off cell orientation distribution at $De \sim 10.26$. Flat-on, Edge-on, and Misaligned orientations are labeled as blue, orange, and red respectively. The total measured number of sperm cells is $N= 3362$71

23. General force mechanics on sperm cell migration depending on the critical Dean number. Schematics images illustrate the sperm cells focusing positions and the corresponded force balance in low aspect ratio spiral channel with dimension of $75\text{ }\mu\text{m} \times 25\text{ }\mu\text{m}$ at (a) $De < De_c$, (b) $De = De_c$, and (c) $De > De_c$. Blue, orange, and red arrows indicate the inertial lift force F_L , Dean drag force F_D , and lift force with no rotation F_{LNR} , respectively. The schematics of sperm cell orientations are same as in Fig.21.....74

24. Plot of the normalized lateral positions of sperm cell streams in spiral channels. The orange, red, and blue color represent the spiral channel with dimensions of $150\text{ }\mu\text{m} \times 25\text{ }\mu\text{m}$, $100\text{ }\mu\text{m} \times 25\text{ }\mu\text{m}$, and $75\text{ }\mu\text{m} \times 25\text{ }\mu\text{m}$, respectively.76

LIST OF ABBREVIATIONS

a	Diameter
AR	Aspect Ratio
C_E	Elastic Lift Coefficient
C_S	Lift Coefficient for the Shear Gradient Force
CTC	Circulating Tumor Cell
C_W	Lift Coefficient for the Wall Interaction Force
d	Gap Distance Between Particle Streams
De	Dean Number
D_h	Hydraulic Diameter
DI	Deionized Water
DLD	Deterministic Lateral Displacement
DNA	Deoxyribonucleic Acid
El	Elastic Number
F_D	Dean Drag Force
F_E	Elastic Force
F_S	Shear Induced Lift Force
F_W	Wall Induced Lift Force
FWHM	Full Width at Half Maximum
F_Ω	Rotation-induced Lift Force

h	Channel Height
HA	Hyaluronic Acid
I	Identity Matrix
L	Velocity Gradient Tensor
M	Major Axis of Sperm Head
m	Minor Axis of Sperm Head
N_I	First Normal Stress Difference
NA	Numerical Aperture
PEO	Polyethylene Oxide
PFF	Pinched Flow Fractionation
PVP	Polyvinylpyrrolidone
Q	Flow Rate
R	Radius of Curvature
RBC	Red Blood Cell
Re	Reynolds Number
Re_p	Particle Reynolds Number
T_e	Extra Elastic Stress Tensor
\dot{T}_e	Upper-convective Time Derivative
u	Velocity Vector
U_f	Average Fluid Flow Velocity
U_{Max}	Maximum velocity of fluid
U_{SF}	Secondary-flow Velocity
w	Channel Width

WBC	White Blood Cell
Wi	Weissenberg Number
α	Mobility Factor Related to Shear-thinning
β	Blockage Ratio
γ	Shear Rate
λ	Fluid Relaxation Time
μ	Viscosity
μ_P	Viscosity of Polymer Part of Fluid
μ_S	Solvent Viscosity
ρ	Density
σ_{xx}	Streamwise Normal Stress
σ_{yy}	Transverse Normal Stress

SUMMARY

Explosive growth of microfluidics has triggered numerous advances in focusing, separating, ordering, and concentrating of cells. Microfluidic systems capable of performing these functions are rapidly finding applications in clinical and biomedical fields. However, most microfluidic methods have been demonstrated using spherical particles in Newtonian fluids. Yet, fluids such as blood, saliva, and cytoplasm are non-Newtonian, and cells such as red blood cells and spermatozoa cells are asymmetrical in shape. These key differences can reduce effectiveness of the microfluidic separation methods. In this work, we use spiral inertial microfluidic devices to investigate migration dynamics and focusing evolution of beads in non-Newtonian, elasto-inertial flows. Coupling of Dean flow that arises from the spiral channel geometry with fluid elasticity yields complex migration behavior. The flow rate, device curvature, and medium viscosity were found to influence lateral migration of cells or particles within these channels. In addition, we used spermatozoa cells to investigate the mechanism of asymmetric shape effects on lateral migration in the spiral channel. The sperm cell migration direction and alignment were found to depend on the flow parameters, leading to differences in focusing equilibrium as compared with spherical particles. Ultimately, insights from this work offer a useful guide to microfluidic device design for improving efficiency of 3D focusing in cell sorting and cytometry applications.

CHAPTER 1

INTRODUCTION

1.1. Microfluidic Sorting Techniques

Particle and cell sorting is a critical technique in fluid research, clinical diagnostics, and biomedical applications¹⁻⁴. The laminar flow nature of these devices permits manipulation of fluid and suspended cells or particles with remarkable spatial and temporal precision. Both biophysical and biochemical properties of the cells and particles are widely exploited in these devices as markers for generating differentiated spatial positioning inside the devices by adding either external⁵ or internal differentiating fields^{6,7}. With the emergence of microfluidics, extensive devices have been invented for particle and cell sorting, owing to significantly minimize the size of the system, rapid sample processing and analyzing, higher spatiotemporal precision, and lower cost⁸⁻¹². The microfluidic particle and cell sorting techniques can be divided into active and passive methods. Active microfluidic methods rely on the external forces to manipulate particle and cells in microchannel, including magnetic^{13,14}, electrophoretic^{15,16}, dielectrophoretic^{17,18}, acoustic^{19,20}, and optical forces^{21,22} for differentiating particles and cells flowing in a microfluidic channel. Typically, active microfluidic methods offer precise control of particle and cell spatial distribution which is beneficial for sorting of highly heterogeneous sample. However, these methods limited throughput and required sophisticated device architecture.

Passive microfluidic methods rely on intrinsic hydrodynamic forces due to the geometry

of the microchannels to position and spatially order particle and cells positions without external actuators, power sources, or fields. A wide range of devices using passive methods, such as pinched flow fractionation (PFF)²³, deterministic lateral displacement (DLD)²⁴ and inertial filtration^{3,4}, is generally achieved in Newtonian fluids by manipulating the inherent hydrodynamic force or channel geometry. Passive microfluidic methods offer attractive advantages over the active methods, including the simplicity design, fabrication, low cost, and high-throughput, with most approaches being label-free. Although the passive microfluidic techniques achieve sorting and focusing of particle and cells with remarkable advantages, most of these methods are demonstrated by spherical particles and performed in Newtonian fluids. However, biological cells such as red blood cells (RBCs) and sperm cells are asymmetrical in shape and fluids such as blood⁵, salivar⁶ and cytoplasm⁷, are non-Newtonian fluids which can void the effectiveness of aforesaid methods for particle separation.

1.2. Particle and Asymmetrical Cell Focusing

Particle and cell focusing is the essential step of microfluidic techniques for sorting and separation, which determine the efficiency and performance of the devices. Spiral microchannels have been widely used in the application of particle and cell sorting. Microfluidic devices have been widely applied to using spherical particles and spherical cells in sorting²⁵⁻²⁷, focusing²⁸⁻³⁰, and trapping³¹⁻³³ applications in Newtonian fluids. However, the underlying mechanism of the intrinsic hydraulic forces that induce focusing, especially in viscoelastic fluids and with asymmetrical cells, are not completely understood.

Viscoelastic fluids are non-Newtonian, and often found in biofluids, such as whole blood^{34,35}, semen³⁶, and cytoplasm³⁷. Compared with Newtonian fluidics, the viscoelastic flow

includes elastic force³⁸ in addition to the inertial shear stress, which can impact device performance and cell separation effectiveness. These biofluids are generally viscoelastic in nature, making cell sorting challenging. Fortunately, recent publications^{39–41} have suggested that fluid viscoelasticity can offer unique opportunities to focus cells into different cross-sectional locations in straight microfluidic channels, depending on their size, while investigators have focused on applications of such devices, little attention has been paid to the underlying principles. This is especially true in curved channels, where curvature induces an additional Dean force which results in complex interplay of elastic, inertial and Dean forces as particles or cells migrate within flow. Xiang *et al.*⁴² attempted to explain the observed migration behavior using a complex six-step model. However, evolution of particle migration along the channel downstream length was not well described, leading to an incomplete model. Lee *et al.*⁴³ investigated particle lateral position dynamics along the channel downstream, but in a single spiral channel and narrow flow rate range (0.83 to 12.5 $\mu\text{L}/\text{min}$). In a more recent study, Kumar *et al.*⁴⁴ showed that the hydrodynamic force balance in cross-section, with particles reaching stable 3D focusing at high Re . However, the lack of direct observation of particle vertical position in flow puts in question the accuracy of the inferred viscoelastic migration mechanism in 3D in spiral channel. Thus, despite these efforts, a clear understanding of 3D migration of particles in spiral channels in elasto-inertial flows is still lacking.

In Newtonian fluids, a secondary flow occurs due to the centrifuge effects and the pressure gradient near the inner and outer walls, leading to form two counter rotating vortices named the Dean vortices at the top and bottom halves of the channel^{45,46} when the Dean number (De) is smaller than the critical Dean number (De_c) for low aspect ratio spiral channel⁴⁷. The current focusing model for spiral devices is performed by spherical particles. This model does

not appropriately explain the focusing behavior of cell/particles with asymmetrical shape in spiral channel. Hur *et al.*⁴⁸ demonstrated that the inertial effects alternated the equilibrium positions of the particle with various shapes, such as cylindrical, ellipse, disk-shaped, and doublet shape. Masaeli *et al.*⁴⁹ found that particle rotation is a necessary component in altering the equilibrium position across the channel depending on the rotation diameter. Li *et al.*⁵⁰ developed a inertial to separate *E. gracilis* by their shape aspect ratio. However, most of the studies on asymmetrical cell focusing are in straight channels. Hence, asymmetrical cell focusing studies in spiral channel to date are limited due to complexity of interaction of the hydraulic forces, resulting the asymmetrical cell focusing dynamics less understood in spiral channel.

1.3. Motivation

Spiral is the most frequently used channel geometry to induce secondary Dean flow. Recent studies^{51–54} demonstrate that the fluid elasticity and cell shape have significant impact on migration of cells within flow in microfluidics devices. Particle focusing behaviors have been studied in viscoelastic fluids in spiral microchannels. However, the underlying mechanism of particle migration in curved channel is not completely understood. In part, this is due to challenges associated with investigating particle migration in 3D in spiral channels. The three major challenges include (1) variation of force balance in the downstream direction due to the planar spiral geometry, (2) complex interaction between inertial lift, elastic, and Dean drag forces, and (3) lack of direct observation from side-view. Hence, there is a need for the study of particle focusing in viscoelastic in spiral channel. Thus, illustrating the full focusing pattern along the downstream channel length, with side view imaging yielding observations on vertical migration of focused streams will offer a useful guide on viscoelastic microfluidics device design

for improving efficiency of 3D focusing in cell sorting and cytometry applications.

Although shape-based sorting has not been considered in conventional techniques, such as centrifugation and filtration, recent studies show that particle/cell shape effects have been considered in microfluidics techniques for sorting and separation. However, most of the asymmetrical particle focusing studies were investigated in the straight channel. It is not clear how the cell with asymmetrical shape focusing by the secondary vortices induced F_D in spiral channel. Thus, there is an urgent need to investigate particle migration in viscoelastic fluids and asymmetrical cell flow dynamics in inertial fluids in order to develop an improved understating and better design guidelines to realize more efficient spiral microfluidic devices for cell-based applications in biofluids.

1.4. Scope of Work

In this work, spiral microchannel are fabricated and optimized to observe the particle and asymmetrical cell focusing behaviors in both Newtonian and non-Newtonian fluids. To improve the understanding of the underlying physics, the goal of this study is to investigate evolution of migration dynamics for particles and cells, including their shape and size effects, and to establish a model that offer a useful guide for viscoelastic microfluidics and inertial microfluidics device design. This study allows fast growth of microfluidics application, ultimately leading to improved performance and broader acceptance of the viscoelastic and inertial microfluidic devices for real biofluid samples. Two specific aims were investigated to address these goals. The first aim investigated particle focusing evolution in viscoelastic fluid in spiral microchannels. With direct observation and evaluation of viscoelastic focusing behavior in spiral microchannels, it enables to elucidate the underlying fluid physics of particle migration along the

channel width and height. Based on the concepts of inertial microfluidics in spiral channels, particle migration in purely Newtonian fluids and viscoelastic fluids were compared, which provides an improved understanding and a model of particle migration in spiral microchannels in viscoelastic flows.

Second aim focused to explicate the asymmetrical shape effects on cell migration in spiral microchannels. Due to the limited source of asymmetrical and cell-like shape particles, it is difficult to explore the shape effects and not ideally to mimic cells migration by using the spherical particles. Therefore, spermatozoa cells, consisting of asymmetrical head and long tail, will be used in viscoelastic and inertial fluids and to investigate the mechanism of asymmetrical shape effects on migration in spiral channel. This study found that asymmetric cell shape and long-thin tail affects interaction of hydrodynamic forces and will result in altering of the equilibrium positions within the spiral microchannel.

1.5. Chapter Summaries

Following this introduction, Chapter 2 will summarize the physics of viscoelastic fluids and will discuss passive microfluidic methods for particle and cell sorting in viscoelastic fluids. The chapter will also review of the advantages and challenges of Dean coupled elasto-inertial focusing. Chapter 3 will introduce the investigation of particle migration dynamics in viscoelastic fluids in spiral channels. Firstly, the particle lateral migration evolution along the channel downstream will be discussed and a three-regime migration model will be introduced. Next, influence of coupled Dean drag, elastic, and inertial lift forces acting on particles in both lateral and vertical directions will be described. Chapter 4 will introduce the focusing dynamics of asymmetrical cells (sperm) in Newtonian fluid in spiral channels. The shape and tail effects on

sperm cell lateral and vertical migration will be discussed and a critical Dean number that defines the transition from outward to inward migration will be introduced. Chapter 5 will summarize and conclude this work, along with a discussion of the potential future directions.

CHAPTER 2

BACKGROUND

(Parts of this chapter were previously published as Jian Zhou, Prithviraj Mukherjee, Hua Gao, Qiyue Luan, and Ian Papautsky. “Label-free microfluidic sorting of microparticles”. APL Bioeng. 3, 041504 (2019). Permission statements are included in Appendix.)

2.1. Viscoelastic Microfluidics

The tremendous clinical potential of circulating tumor cells (CTCs)^{25,55,56} and circulating extracellular vesicles (e.g., exosomes)⁵⁷ for liquid biopsy in cancer diagnostics and precision medicine has been driving the burgeoning development of microfluidic devices for cell sorting and isolation. Recent, particle separation utilizing the intrinsic viscoelasticity has been successfully demonstrated that viscoelastic focusing of particle is preferable in forming a 3D single stream focusing^{58,59} and in enrichment of sub-micrometer particles^{57,60}, which is generally challenging in inertial microfluidic devices. In a circular microchannel, particles tend to focus into a single position (3D-focusing) located in the channel central axis of the channel where the shear rate is the lowest⁵² (**Fig.1a**). In a square straight channels, due to the asymmetric shear distribution, particles focus at the channel the four corners also exhibit a stable equilibrium position near the channel central axis⁶¹ (**Fig.1b**). Therefore, five equilibrium positions are observed as shown by Seo *et al.*⁵² and Yang *et al.*⁶¹ In a rectangular channel, Lenshansky *et al*⁶² in 2007 demonstrated that particles become confined into a broad band near the central plane of the channel in a low aspect ratio channel. Particle separation was demonstrated using elastic

force in a device consisting of both circular and square channel segments (**Fig. 1d**), but throughput was low ($<0.05 \mu\text{L}/\text{min}$).

Adding inertial force into a viscoelastic microfluidic device offers benefits in terms of particle focusing and separation. On one hand, non-negligible inertia means a higher flow rate and thus higher processing throughput. On the other hand, the interaction of inertial and elastic forces determines the focusing pattern of particles and therefore provides distinct particle focusing behaviors that can be useful for separation (elasto-inertial focusing and separation)⁶¹. When fluid inertia is not negligible (i.e., elasto-inertial flows), multiple equilibrium positions can be reduced to a single 3D position by regulating the synergetic combination of the elasticity and inertial effects on particles (**Fig.1c**)^{58,61}. Due to the wall induced lift force, particles near the four corners of a square channel are pushed toward the channel center, leading to the elimination of the four focusing positions and entrainment of all particles in the channel axis (3D-focusing).

The non-Newtonian fluids are usually made by dissolving macromolecular powder into Newtonian medium. Typical macromolecules used for enhancing fluid elasticity include hyaluronic acid⁶³ (HA), poly(ethylene oxide)⁶⁴ (PEO), deoxyribonucleic acid⁶⁵ (DNA), and poly(vinylpyrrolidone)⁶⁶ (PVP). Many groups have been intense attention to PEO recently years, because of its excellent abilities of water solubility⁶⁷, biocompatibility⁶⁸, and low toxic⁶⁹. Due to the capability to form hydrogen bond, uncharged and relatively inert, PEO has been widely and mostly used in biomedical applications. These include prevention of particle aggregation⁷⁰, maintain membrane structure^{71,72}, and reduction of protein adsorption⁷³. Also, it was found that PEO aqueous solutions exhibit shear-thinning behaviors as whole blood and semen. Because of its advantages, PEO has been the medium of numerous viscoelastic microfluidics theoretical and

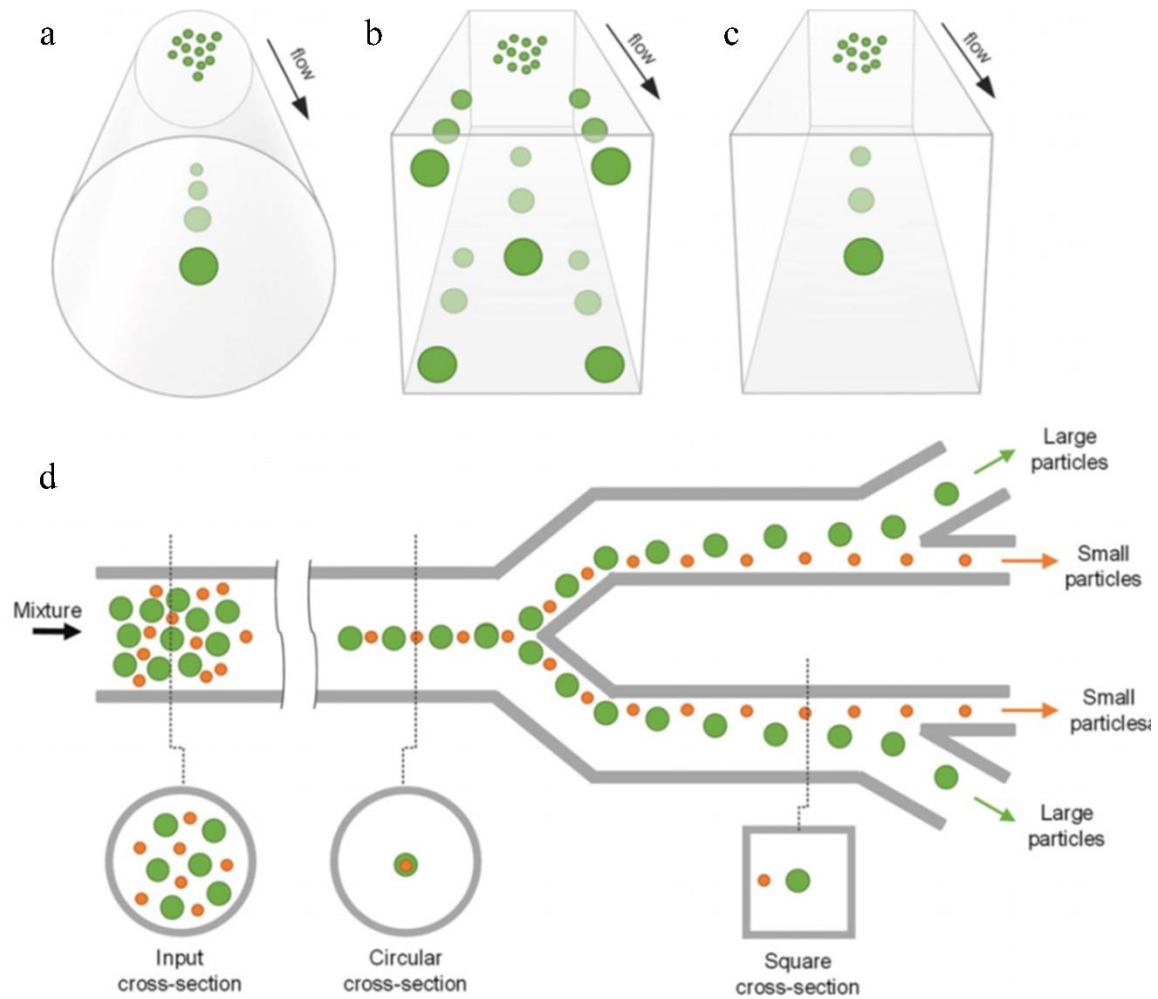


Figure.1. Viscoelastic focusing and sorting of particles. (a) Viscoelastic focusing creates a single equilibrium position along the central axis of a circular capillary. In square channels, there are (b) five focusing positions when flow is elasticity dominant and (c) a single position at the centerline when flow is elasto-inertial. (d) Size based sorting of particles using elasticity dominant flow in a device with a combination of circular and square cross-sections. Reproduced with permission from APL Bioeng. 3, 041504 (2019) Copyright 2019 APL Bioengineering.

simulation studies. Therefore, we select PEO solutions as the base medium to exploit cell migration evaluation in viscoelastic fluids.

2.2. Inertial Microfluidics

Inertial microfluidics, relying on inertia of the surrounding fluid, with inertial effects driving cells across flow streamlines into equilibrium positions, has proved to be a fascinated technique for label free, passive particle and cell sorting in microfluidic channels. It is well accepted now that the particles focused into the equilibrium positions by the shear-induced lift force (F_s) and wall-induced lift force (F_w). The number and location of particles equilibrium positions are dependent on the channel geometry and the cross-section shape (**Fig.2**). Segré and Silberberg⁷⁴ in 1960s first found that neutrally buoyant particles focused into a narrow annulus at $\sim 0.2D_h$ from the wall, where the F_s balances F_w (**Fig.2b**). In straight microfluidic channels of square cross-section, cells focus in four equilibrium positions at the center of each side wall (**Fig.2b**)⁷⁵. In channels of rectangular cross-section, the number of equilibrium positions is reduced to two near the centers of the larger side walls (**Fig.2c**)²⁸. The inertial microfluidics of particle in rectangular microchannels migrates with the lift forces and occurs into two stages²⁸. In stage I, F_s dominates the particle migration and push particles to the top and bottom walls, whereas in stage II, particles migrate to the center of the top and bottom channels by the rotation-induced lift force (F_Ω).

Introducing channel curvature disrupts this equilibrium balance due to emergence of secondary flow that forms counter-rotating Dean vortices creates two vertical equilibrium positions near inner convex side wall depending on the particle sizes^{76,77}. The flow in spiral channel is more complex than straight channels due to the secondary Dean vortices induced an

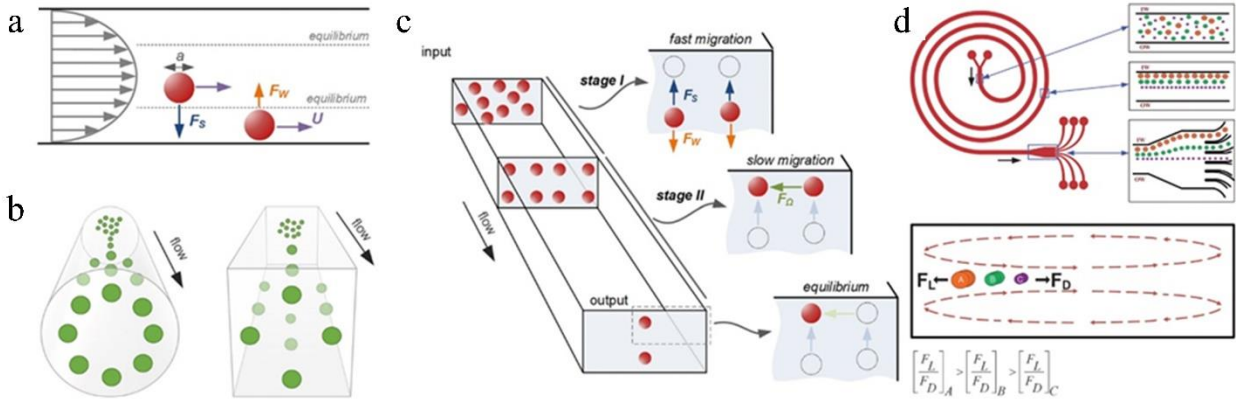


Figure.2. Inertial focusing in microchannels. (a) Two lift forces orthogonal to the flow direction act to equilibrate microparticles near the wall. The shear-induced lift force F_S is directed down the velocity gradient and drives particles toward channel walls. The wall-induced lift force F_W directs particles away from the walls and drives particles toward the channel centerline. The balance of these two lift forces causes particles to equilibrate. (b) Inertial focusing creates an annulus in cylindrical capillaries and four symmetric positions in square channels. In both cases, the equilibrium positions are approximately at $\sim 0.4Dh$ from the sidewall. (c) In a rectangular channel, there are two preferred equilibrium positions. A two-stage model describes inertial migration of microparticles first from the channel bulk toward equilibrium positions near long walls under the influence of F_S and F_W and then parallel to channel walls into wall-centered equilibrium positions under the influence of the rotation-induced lift force (F_Q)²⁸. Reproduced with permission from APL Bioeng. 3, 041504 (2019) Copyright 2019 APL Bioengineering. (d) Schematic of the spiral microparticle separator. The randomly dispersed particles equilibrate at different equilibrium positions along the inner wall of the spiral microchannel under the influence of F_L and F_D . Separation between individual particle streams is enhanced by opening the spiral channel into a wider straight channel before extracting the individual streams using a multiple outlet design. Microchannel cross-section illustrating effects of F_L and F_D on particles. The ratio of forces (F_L/F_D) is the determining factor in where a particle of given size (diameter) equilibrates⁷⁸. Reproduced with permission from Lab on a Chip. 2009,9, 2973-2980. Copyright 2009 Royal Society of Chemistry.

additional Dean force (F_D). Kuntaegowdanahalli *et al.*⁷⁸, for first time, demonstrated the sorting of particles in spiral channels with rectangular cross-sectional shape. Particles flowing near the top or bottom of the channel cross-section are subjected to Dean drag force (F_D), while the inertial lift forces are orthogonal, causing them to migrate with the Dean vortices. Near the outer wall, the net lift force (F_L) is in the same direction as F_D , and thus, particles follow the Dean vortices independent of their size. Near the inner wall, however, inertial and Dean forces act in opposite directions, leading to a possible force balance for particle focusing into their equilibrium positions. The equilibrium position of a particle is determined by the ratio of F_L/F_D , yielding distant streams near the inner wall of the channel based on the diameter of the particle (Fig.2d).

2.3. Physical Mechanism and Hydraulic Forces

Viscoelastic fluid is one of the non-Newtonian fluids that are qualitatively distinct from Newtonian fluid in behavior. As suggested by its name, viscoelastic fluid comprises both viscous and elastic components, with the later mainly responsible for the imbalanced normal stresses under shear¹⁵. As a result, the normal stress differences in viscoelastic flow are non-zero which is unlike the case in Newtonian flow. The first normal stress difference is accounted for the lateral migration of particles in such flow and it is now generally termed as elastic force (F_E)¹². This force drives particles suspended in viscoelastic flow from high shear-rate region to low shear-rate region^{12,15}. Consequently, in a circular microchannel, particles subjected to this force migrate toward the channel center-axis and eventually reach a single-file entrainment (3D-focusing)¹⁰.

More intriguingly, such phenomenal lateral migration is size dependent as the driving

elastic force is strongly correlated to particle diameter ($F_E \sim a^3$). Thus, passive separation of particles is possible in viscoelastic flows. Indeed, in the absence of other forces such as inertia, focusing and separation of particles has been successfully demonstrated by a number of groups^{8,9,16}. When fluid inertia comes into play, more complex scenario can occur. There are dimensionless numbers that help to understand the force interactions within a viscoelastic flow and to predict particle migration.

2.3.1. Reynold Number

The Navier-Stokes equations determined that the particle migration across the microchannel due to the inertial effects where the inertia and viscosity of the fluid are finite¹. When particles are flowing in un-negligible inertia fluids, the inertial effects impact their migration by inertial lift force. The inertial effect on fluid and particle motions is measured by the Reynolds number (Re):

$$Re = \frac{\rho U_f D_h}{\mu} \quad (1)$$

where U_f is the average fluid flow velocity, ρ is the fluid density, μ is the fluid viscosity, and D_h is the hydraulic diameter of the channel. The fluid inertia would become more significant on particle migration with increasing the Reynolds number, which enable the manipulation of particle migration within inertia microfluidics channel. It is well accepted now that inertial focusing occurs when particle Reynolds number $Re_p \geq 1$ ($Re_p = Re(a/D_h)^2$)³⁰, where a is diameter of cell/particle.

2.3.2. Dean Number

In a curved microchannel, Newtonian fluid undergoes centrifugal acceleration directed radially outward leading to the formation of two counter-rotating vortices known as Dean vortices which result in the inherent velocity differences in the channel cross-section where the center of the channel moves faster and pushes particle toward the outer wall^{78–80}. The magnitude of Dean flow is given by a non-dimensional parameter Dean number:

$$De = Re\left(\frac{D_h}{2R}\right)^{0.5} \quad (2)$$

where R is the radius of the curvature. Particles migration near the top or bottom half of the channel cross-section are dragged by the Dean drag force F_D , leading them flow with the Dean vortices. Thus, the magnitude of the F_D is strongly dependent on the dimensions of the channel and the radius of curvature.

2.3.3. Weissenberg number

When particles flowing in viscoelastic fluid, they are subjected to the elastic effects. The fluid elasticity can be evaluated using the Weissenberg number (Wi), which compares elastic force with viscous force acting on particles⁶¹. For rectangular cross-section, the Wi number can be expressed as:

$$Wi = \lambda \dot{\gamma} = \frac{2Q\lambda}{hw^2} \quad (3)$$

This non-dimensional number is a measure of importance of the elastic fluid properties and is defined as a function of flow shear rate $\dot{\gamma}$ and fluid relaxation time λ . The shear rate $\dot{\gamma}$ can be approximated as $\dot{\gamma} = 2Q/hw^2$ in rectangular channels, where Q is the flow rate, h is the channel

height, and w is the channel width. The viscoelasticity can be then characterized with by Wi and the elastic force is strengthened with increasing Wi .

2.3.4. Elastic number

The viscoelastic effect can also be characterized by the elasticity number⁶¹:

$$El = \frac{Wi}{Re} \quad (4)$$

It is the ratio of the Weissenberg number to Reynold number, equivalently the ratio of elastic force to inertial force. El only depends on the fluid rheological properties and the characteristic length scale. $El \gg 1$ indicates dominance of fluid elastic force while inertial stress is expected to be dominant when $El \ll 1$. In Newtonian fluids, $El = 0$ and thus the elastic force $F_E = 0$ and inertial effects dominate.

In this study, we aim to exploit a moderate range of elasticity numbers that the particle motion is influenced by both elastic and inertial effects. Therefore, three dominates forces govern on particle migration in viscoelastic microfluidic in spiral channel : inertial lift force, Dean drag force and elastic force, each schematic shown in **Fig.3**.

2.3.5. Inertial Lift Force

The inertial lift force composes wall-induced (F_W) and shear-induced force (F_S). The shear-induced force push particles away from the center to walls whereas wall-induced force push particles away from the walls to center. As particles flow downstream, they experience shear gradient lift force F_S induced by fluid shear as well as wall-induced lift force F_W generated by the interaction of particles and channel walls. These forces scale strongly with particle

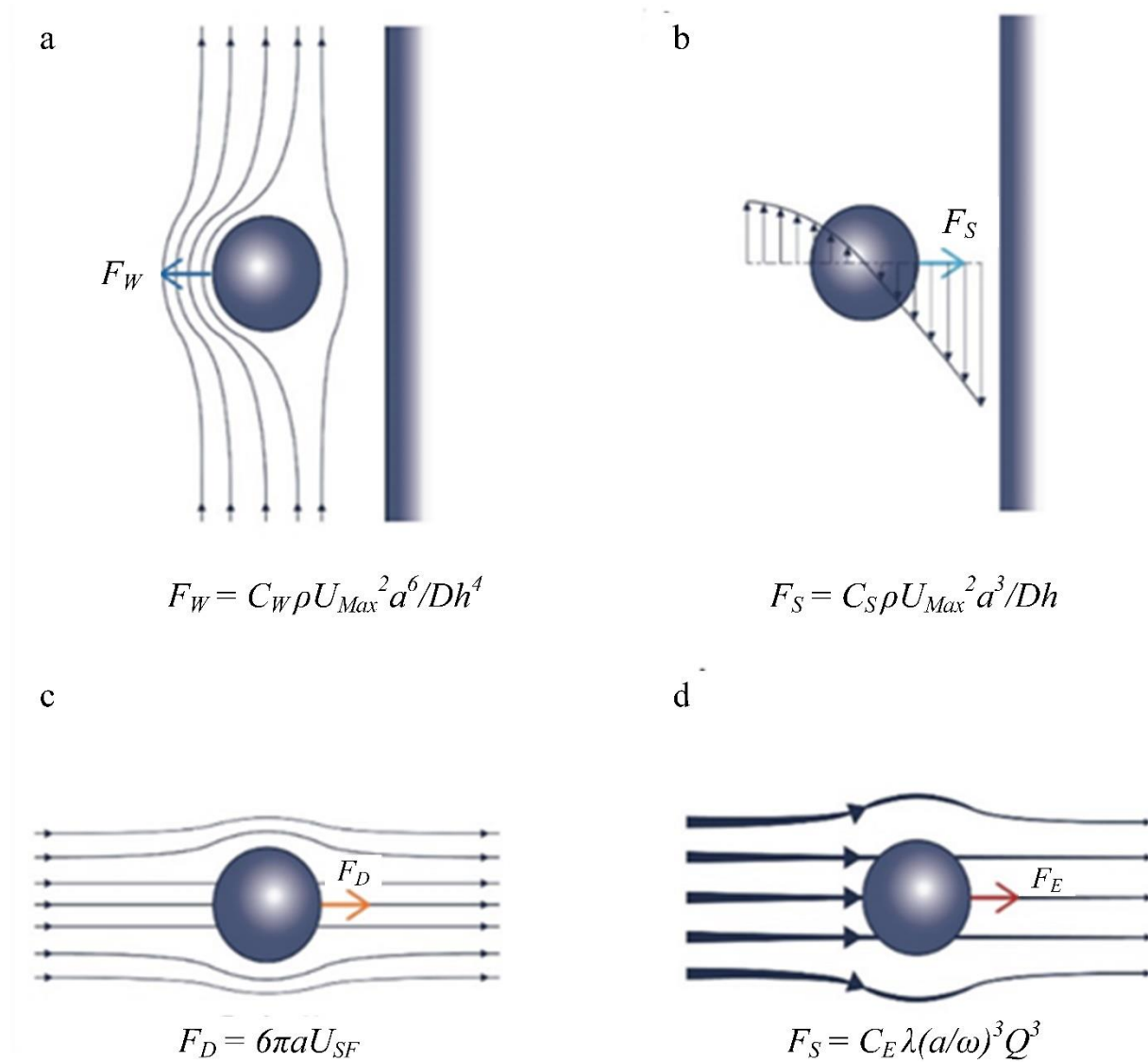


Figure.3 Schematic of hydraulic forces in Newtonian and non-Newtonian flows. (a) Wall induced force. C_W is the coefficient of wall induced force, ρ is the fluid density, a is the particle diameter and D_h is the channel hydraulic diameter. (b) Shear gradient lift force. C_S is the coefficient of shear gradient lift force. (c) Dean drag force. (d) Elastic force. C_E is elastic lift coefficient. λ is the time of the fluid. w is the width of the channel. Q is the flow rate. Reproduced with permission from Annual Reviews 2014, Annu. Rev. Biomed. Eng. 2014. 16:371–96.

diameter, as near the channel wall^{28,78,81}:

$$F_W = \frac{C_W \rho U_{Max}^2 a^6}{D_h^4} \quad (5)$$

where the C_W is the lift coefficient for the wall interaction force, which changes with Reynolds number and position⁷⁵. U_{Max} is the maximum velocity of fluid. As the interact with the walls of the channel, particle will move slightly slower than the fluid and pressure will build between the particle and walls, causing the F_W toward away from the walls as shown in **Fig.3a**.

The lift force F_S acting on particles near the channel center:

$$F_S = \frac{C_S \rho U_{Max}^2 a^3}{D_h} \quad (6)$$

where C_S is the lift coefficient for the shear gradient lift force. In plane Poiseuille flow, the parabolic shape of the velocity profile results in a shear gradient lift force with direction towards to the walls of the channel as shown in **Fig.3b**.

2.3.6. Dean Force

In spiral channel, the equilibrium positions reduced to one and particle migrates towards the concave side wall due to F_D show in **Fig.3c**. In our previous works, particle equilibrates under the combined influence of inertial lift force and Dean drag force near inner microchannel wall and the equilibrium position of particles is dependent on the ratio of inertial and Dean force based on their size⁷. The Dean drag force, F_D exerting on particle, due the two major Dean vortices and is derived by Stokes drag:

$$F_D = 6\pi\mu a U_{SF} \quad (7)$$

where the U_{SF} is the secondary-flow velocity. In our previous study^{7,78,82}, cells flowing near the top or bottom of the channel cross-section are subjected to Dean drag force F_D , while the inertial lift forces are orthogonal, causing them to migrate with the Dean vortices. Near the outer wall, the net lift force F_L is in the same direction as F_D , thus particles follow the Dean vortices independent of their size. Near the inner wall, however, inertial and Dean forces act in opposite directions, leading to a possible force balance for particle focusing into their equilibrium positions.

2.3.7. Elastic Force

The underlying mechanism of particle lateral migration in viscoelastic fluids is that the normal stress generates an elastic force which drives particle from higher shear-rate region to lower shear-rate region (**Fig.3d**). In pure viscoelastic fluid when inertial effect is negligible, elastic lift force dominates particle/cell migration, resulting in particle focused at the center of a circular channel and five equilibrium positions, at four corners and center, in rectangular channel. In viscoelastic microfluidics, particle migration depends on viscoelastic effects in addition to the inertial effects discussed above. The elastic force is proportional to the first normal stress difference (N_I) defined as the difference between the streamwise normal stress (σ_{xx}) and the transverse normal stress (σ_{yy}):

$$F_D = C_E \lambda \left(\frac{a}{w}\right)^3 Q^3 \quad (8)$$

where C_E is elastic lift coefficient. It is the strongest near the four walls of the channel and is the weakest near the center and corners⁸³. The interaction between elastic and inertial forces results in the equilibrium position near the centerline.

2.4. Viscoelastic Focusing and Separation

In viscoelastic fluids, particle migration dominated by inertial and elastic forces are highly size-dependent and been successfully used for passive particle and cell separations (**Fig.1**). Ahn *et al.*⁸⁴ took the advantage of the centripetal migration behavior of particles in a square microchannel for separating 2.3 and 4.5 μm particles. PEO solution was used to induce viscoelasticity of the medium and their flow rate was up to 80 $\mu\text{L}/\text{min}$ where inertial force acted simultaneously with elastic force to drive particles toward their equilibrium positions in the channel central axis. As smaller particles moving slower due to weaker driving forces, larger 4.5 μm particles reached channel center ahead of 2.3 μm particles, leading to good separation with 96% recovery for larger particles.

The synergetic interaction of elastic and inertial forces can also lead to distinct focusing positions of different particles in a rectangular microchannel, which can be readily employed for sheath-less particle and cell separation. Liu *et al.* showed 15 μm particles were focused into two streams flanking the central focused stream of 5 μm particles in a rectangular microchannel with aspect ratio of 2⁸⁵. Such size-based focusing pattern of particles was then utilized for separation of MCF-7 cells from red blood cells with 91% efficiency. The same scheme with smaller channel (10 μm height) was also used for separation of *E. Coli* from RBCs in PEO solution with throughput $\sim 2 \mu\text{L}/\text{min}$. Nam *et al.*⁴¹ demonstrated a co-flow microfluidic device (**Fig. 4a**) achieving a recovery rate $>99\%$ for both 1 μm and 5 μm particles at an optimal flow rate of 4.5 $\mu\text{L}/\text{min}$. In this device, PEO flow was injected into the channel and fractured the sample flow

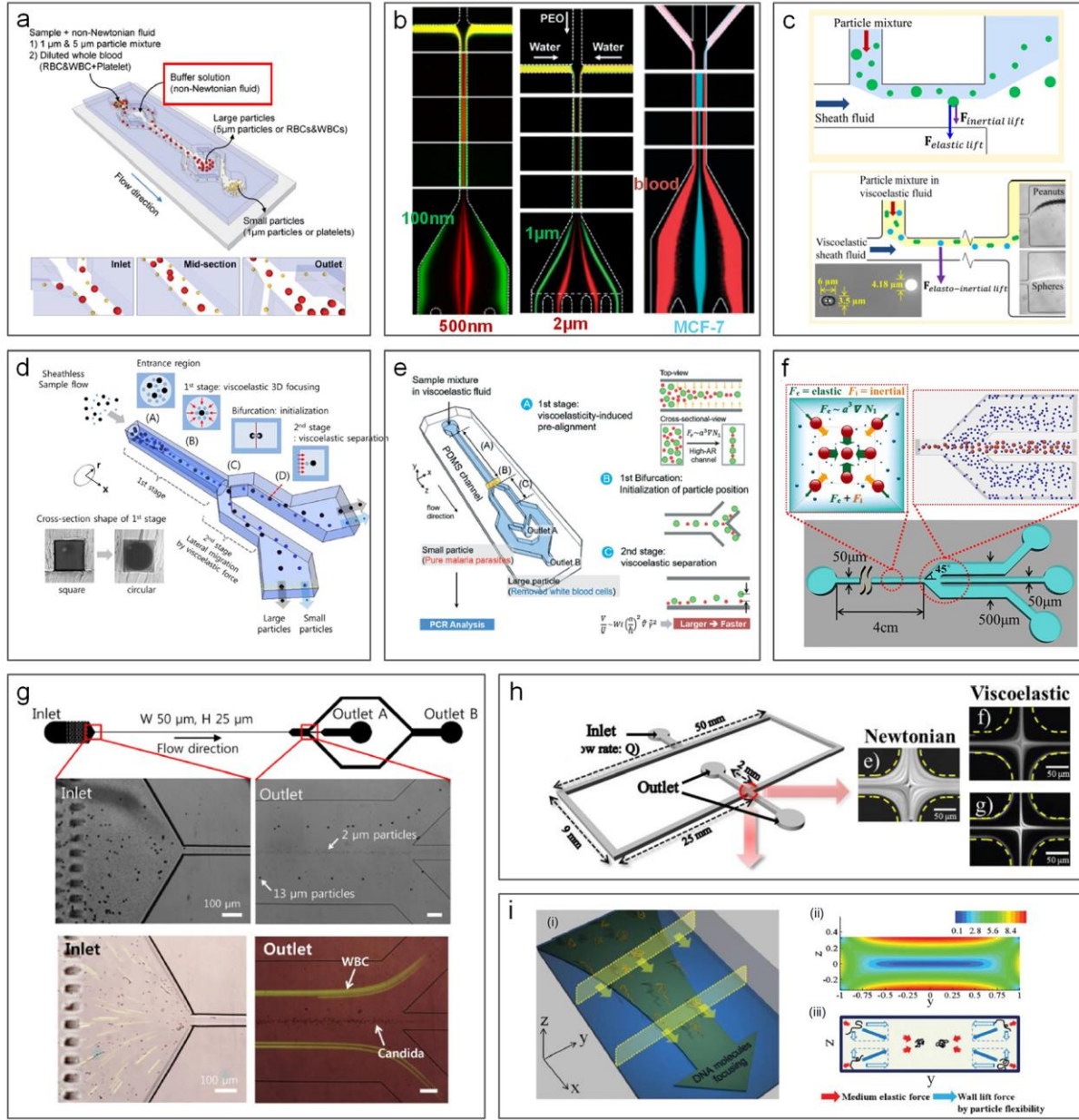


Figure. 4 Viscoelastic microfluidics for particle sorting and other applications. (a) Separation of 1 μm and 5 μm diameter particles in a square co-flow microchannel using viscoelastic flow⁴¹ (b) Three co-flow channels used for separation of 500 and 100 nm diameter particles⁵⁷, 1 μm and 2 μm diameter particles⁸⁶, and MCF-7 and blood cells⁸⁷. (c) Combination of viscoelastic flow and pinched flow fractionation (PFF) for size-based⁸⁸ and shape-based⁸⁹ particle separation. (d) Sheathless separation of particles in viscoelastic flow using a microchannel with round and square cross-sections⁹⁰. (e) Separation of malaria parasites from WBCs in a two-segment channel with a high aspect-ratio cross-section⁹¹. (f) Particle filtration in a square microchannel using elastic and inertial forces⁸⁴. (g) Sheathless separation of particles and cells in viscoelastic flow⁹². (h) Measurements of monitoring cell deformability using viscoelastic single-stream focusing⁹³ (i) DNA focusing in a rectangular channel based on elastic force and flexibility-induced force⁹⁴. Reproduced with permission from APL Bioeng. 3, 041504 (2019);

into two streams near sidewalls. In this flow configuration, the faster migration of larger particles crossed the flow interface into the clean buffer stream, leading to the clean separation of the two particles. Separation with a recovery rate of 99% was also demonstrated in separation of platelets from highly diluted blood⁴¹. Later, the same configuration was used by Tian *et al.*⁸⁶ to achieve a high-resolution separation of 1 μm and 2 μm particles and MCF-7 cells⁸⁷. A complete separation was achieved at sample flow rate 5 $\mu\text{L}/\text{min}$ (**Fig.4c**). In such device and flow configuration, separation of submicron particles (e.g., exosome) was also demonstrated with 80% recovery rate by the same group¹³. Such elasto-inertial effect has also been coupled with pinched flow fractionation (PFF) for enhanced particle separation lately^{89,95}. Additional demonstrations include the use of viscoelastic flow for particle filtration in square microchannels⁸⁴ as well as sheathless separation of particles⁹² and measurements of cell deformability⁹³. In addition to microparticles and cells, smaller biomolecules can be separated and focused as well. For example, Nam *et al.*⁹¹ reported separation of malaria parasites from WBCs in a two-segment channel, while Kim *et al.*⁹⁴ reported DNA focusing in a rectangular channel.

2.5. Viscoelastic Focusing and Separation with Dean Coupling

While most of viscoelastic work have been done in straight channels, curved channels provide additional force to the particle migration dynamics. Like in the case of Newtonian fluid flowing in a curved channel, Dean flow of two counter-rotating secondary flows in the cross-section plane is expected in viscoelastic flow in a spiral channel. The Dean flow exerts Dean force on particles in addition to elastic and inertial force. In 2013, Lee *et al.*⁹⁶ first showed focusing and separation of particles suspended in PEO solution flowing in a spiral microchannel. As opposing the general focusing position near inner wall in an inertial spiral channel, particles

entrainments were observed near the outer wall for 10 μm particles and close to the centerline for 1.5 μm particles. Dean force and elastic force were considered responsible for the displacement of focusing positions outward as compared to inertial focusing⁷. The exact physics underlying such phenomenon remains unclear despite a recent effort proposing six-stage focusing model⁶⁴. A complete separation of these two particles was readily demonstrated in this device by adding four outlets. Similar to straight channels, spiral channel with viscoelastic flows are found preferred for manipulating small particles with size down to ~ 100 nm as demonstrated in a double-spiral channel where a mixture of 100 nm and 2 μm particles were separated with $>95\%$ efficiency⁶⁰.

In summary, focusing and separation in viscoelastic flows is an important addition to the existing inventory of particle separation methods. Viscoelastic manipulation in microchannels is of great interests considering the universally non-Newtonian property of bodily fluids that are critical in healthcare management. The ability of 3D focusing which is generally difficult to achieve in other passive microfluidic systems is especially useful in cytometry applications. More importantly, size-based focusing due to elastic force remains effective for particles with size down to a few hundreds of nanometers^{57,60}, suggesting promising applications in separation of macromolecules such as DNA (**Fig.4i**) and extra-small bio-particulates such as exosome. It is advantageous over inertial separation which is preferred for microscale particle manipulation and over PFF²³ whose throughput is roughly a magnitude of order smaller than viscoelastic systems, despite that the general requirement of elasticity enhancement which contaminates and may damage sensitive samples.

However, investigations on elucidation of the underlying physics of viscoelastic focusing have been rarely reported. Especially, for spiral channels, curvature induces an additional Dean

force which results in complex interplay of hydraulic forces and less understood. In addition, spherical particle is widely used in mimicking cell migration in flow for device development and optimization, in which the nature structure of most cells is asymmetric such like red blood cells and sperm cells. Thus, the performance of the microfluidic devices for cell manipulation, which tested with spherical particles, is not conform to the theoretical results. It is eager to focus on particle migration in non-Newtonian fluids to elucidate the underlying mechanism of the equilibrium positions for asymmetric cells in spiral channels.

2.6. Asymmetric Cell Sorting

In passive microfluidic devices, the main cell separation method is depended on the cell largest diameter size and characterized by using spherical particles. However, most of cells are non-spherical and asymmetric shape, such as RBCs, spermatozoa, pathogen, and virus. Thus, size depended cell separation poses a challenge for asymmetric cells. Also, shape is a vital physical property to implement biological function and cell identification⁹⁷. For example, red blood cell is able to split from spleen filtration due to the disc-like shape. Sperm cell contains two parts, head and tail (flagellum). The head of sperm cell contains reproductive DNA and enzymes on membrane. The unsymmetrical-paddle shape provides a processing spinning top, in which head spinning around the sperm's longitudinal axis, leading to enhancing the acrosome reaction for breaking through the egg membrane⁹⁸. Shape is also important in cell division, especially in cell development processes, such as cell mitosis and clustering. In addition, shape an indicator in development of many diseases and clinical diagnostics. For example, cancer caused cell mutations make cells losing the membrane adhesions resulted in changing their morphologies and deformations. For sickle-cell and malaria diseases, red blood cells are sickle

shape and become stiffer respectively. However, cell shape has not been considered in many microfluidics devices design. Recently, Song *et al.* achieved sperm separation in spiral microchannels for collecting rare sperm cells from blood cells after TESE procedures⁹⁹. 81% sperm were collected at flow rate of 0.52 mL/min. Li *et al.*⁵⁰ developed a microfluidic device to separate *E. gracilis* by a key shape parameter-cell aspect ratio (AR), ranging from 1 to 7 in different outlets. Holm *et al.*¹⁰⁰ applied DLD methods to sort RBCs and trypanosomes based on the shape and demonstrated that the cell orientation accentuates the shape differences for sorting application. Researchers have reported that viscoelastic fluids can demonstrate effective approaches for sorting particles by the shapes¹⁰¹. However, their attention has been in straight microchannels rather than on underlying spiral microchannels. Therefore, understanding how the shape effect influences on cell migration in spiral is beneficial for improving the separation efficiency and providing a comprehensive device for the separation of cells with similar diameter but different shapes.

2.7. Summary

In this chapter, viscoelastic and inertia microfluidics were discussed from the theoretical perspective. The non-dimension parameters that characterize the inertia, Dean, and elastic effects on particle migration and hydraulic forces in Newtonian and non-Newtonian fluids in straight and curvature microchannel were elaborated. After that, the applications of viscoelastic, elasto-inertial and asymmetrical cell focusing, and sorting were comprehensively reviewed

CHAPTER 3

EVOLUTION OF FOCUSED STREAMS IN VISCOELASTIC FLOW IN SPIRAL CHANNELS

3.1 Introduction

This chapter aims to improve the understanding of the underlying mechanisms of particle elasto-inertial migration in spiral channels. This work systematically investigates evolution of neutrally-buoyant particles along the downstream length from top and side views in spiral microchannels, and explore the effects of device geometry, flow direction, and fluid elasticity on particle focusing dynamics over a wide range of flow rates. The results illustrate the full focusing pattern along the downstream channel length under these diverse conditions. In addition, the sideview imaging yields observations on vertical migration of focused streams. Ultimately, this study anticipate that these results will offer a useful guide on elasto-inertial microfluidics device design for improving efficiency of 3D focusing in cell sorting and cytometry applications.

3.2 Experimental Methods

3.2.1. Spiral Channel Design

Four Archimedean spiral devices (R1, R2, R4 and R6) were used in this work, with 1 mm, 2 mm, 4 mm and 6 mm initial radii of curvature. Channel cross-sectional dimensions were fixed at 250 μm in width and 50 μm in height, corresponding to aspect ratio $AR = 0.2$. Spacing between channels was set at 250 μm . A single outlet was located at the center of each spiral,

while a single inlet with debris filter was located at the circumference. The details of the channel layout and dimension are summarized in **Fig. 5**.

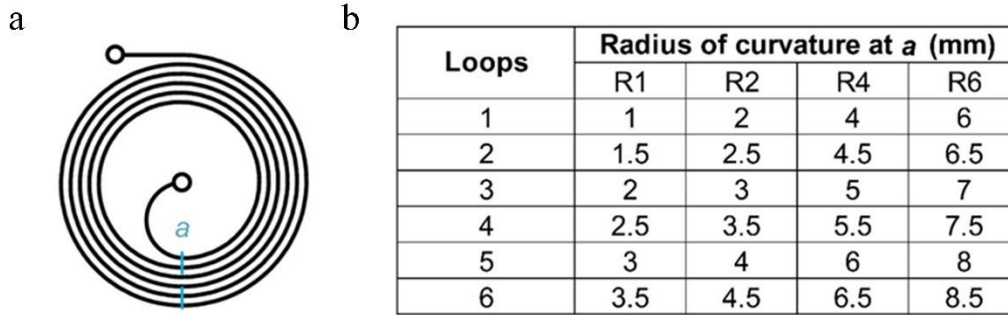


Figure. 5. Details of device design. (a) Schematic layout of spiral channel. (b) Table summarizing details of the four devices of different initial radii of curvature. Loop radius is given at position *a* for each device.

Channels were fabricated in polydimethylsiloxane (PDMS) using the standard soft lithography process with dry photoresist masters, as we detailed previously¹⁰². Briefly, 3 in silicon wafers were dehydrated for 15 min on a 225°C hotplate, laminated with a 50 μm thick film (ADEX 50, DJ Microlaminates Inc., Boston, MA, USA) and baked for 5 min on a 65°C hotplate. Next, the wafers were exposed to UV light (I-line 365 nm, Optical Associates Inc., USA) for 33 s at 10 mW/cm^2 through a mask plate in hard contact. The wafers were developed in cyclohexanone (98%, Acros Organics, USA), washed with IPA and DI water, air dried, and baked for 90 min on a 170°C hotplate (Thermo Fisher Scientific, Inc., USA). PDMS (Sylgard 184, Dow Corning, Midland, MI, USA) was mixed with curing agent in a 10:1 ratio, was cast on the fabricated master, degassed for 90 min in a vacuum oven, and cured on a hot plate at 60°C

for 4 h. PDMS replicas were peeled off and ports were cored using a 1.6 mm diameter biopsy punch (Miltex, Japan). Devices were bonded to standard microscope glass slides using oxygen plasma treatment at 10 W for 20 s (PE-50, Plasma Etch, Inc., Carson City, NV, USA), baked for 60 min on a hot plate at 80°C, and allowed to cool to room temperature before use. For side-view imaging, devices were mounted vertically; to do this edges of PDMS replicas were cut using a sharp blade orthogonal to the spiral pattern, then placed vertically on uncured PDMS in a Petri Dish (Fisher Scientific Inc., MA, USA) and cured on a hot plate at 60 °C for 4 h to improve optical transparency and resurface the cutting edge⁷⁶.

3.2.2 Viscoelastic fluids and Particle Preparation

Polyethylene oxide (PEO) was used as the viscoelastic fluid in this work. Six concentrations were prepared (50 ppm, 250 ppm, 500 ppm, 1000 ppm, 2500 ppm and 5000 ppm) by mixing PEO powder with molecular weight of 2,000,000 Da (Sigma Aldrich., USA) into 22% (w/v) glycerin (Fisher Scientific, Inc., USA) and deionized water (DI). A 5% (w) of NaCl was added to match density of polystyrene particles (1.05 g/cm³). Solutions were gently mixed on stirring plate (ThermoFisher Scientific, Inc., USA) at room temperature for 24 h. Rheological properties of the prepared solutions are summarized in **Table 1**

To investigate focusing behavior, solutions fluorescent 25 µm-diameter polystyrene beads (Polysciences Inc, USA) were prepared with final volume fraction of 0.03% (v/v). Tween 80 (Fisher Scientific, USA) was added at 0.1% (v/v) to minimize aggregation and avoid channel clogging. The larger 25 µm diameter beads (blockage ratio $\beta = a/D_h = 0.3$ since $D_h = 83.3 \mu\text{m}$) were used to observe complete evolution of focused particle streams in relatively short downstream distance due to high viscosity of PEO solutions that limited channel length.

3.2.3 Flow Experiments Setup

Particle suspensions were loaded into a 10 mL syringe with luer lock interface and connected to microfluidic devices using 0.06” PTFE tubing (Cole-Parmer). A programmable syringe pump (Legato 201, Kd Scientific, USA) was used to drive particles into devices with

TABLE 1

RHEOLOGICAL CHARACTERISTICS OF NEWTONIAN^a AND NON-NEWTONIAN^b FLUID

Rheological properties	Water solutions (%wt)		PEO solutions (ppm)					
	NaCl (5%)	Glycerol (22%)	50	250	500	1000	2500	5000
Density, ρ (g/cm ³)	1.05	1.05	1.05	1.05	1.05	1.05	1.05	1.05
Zero-shear viscosity, η (mPa·s)	1	2.05	2.08	2.46	3.12	4	16	32
Overlap concentration, c^* (ppm)			858	858	858	858	858	858
Concentration ratio, c/c^*			0.06	0.29	0.58	1.17	2.91	5.83
Effective relaxation time, λ_e (ms)			2	5.8	9.1	12.4	23	40

^a 5 wt% NaCl and 22 wt% Glycerol/ DI water based Newtonian fluid.

^b 22 wt% Glycerol/ DI water based non-Newtonian fluids^{39,43,103–105}.

preset flow rates on vibration isolation table. The flow rate was varied from 50 μ L/min to 350 μ L/min. The fluorescence imaging was accomplishing using an inverted microscope (IX83 Olympus, Inc., USA) with a 16-bit sCMOS camera (Zyla 5.5, Andor Technology Ltd, Belfast, UK). Fluorescent images of top view were taken at quarter-circle positions throughout channel length with exposure time of 150 μ s for acquiring particle flowing trajectories by using 20 \times objective with high numerical aperture (NA = 0.7). The CellSense software (Olympus, Inc.) was

used to sequentially obtain 150 images at each position. Bright-field images of top view were captured with a high-speed camera (AX 200 Mini, Photron USA, Inc.) at frame rate of up to 10,000 fps depending on flow rate, with exposure time of 1 μ s for obtaining particle distribution probability and height position along the channel height. Bright-field side view images of particles were taken using 10 \times objective with long (10 mm) working distance using procedure described above.

3.2.4 Imaging and Data Analysis

The particle migration trajectories were created by stacking the consecutive frames, and the particle lateral and downstream positions from top view and side view were manually measured using ImageJ, NIH software. The trajectories of particles migration along the downstream were created by consecutively splicing the stacked fluorescence streak images at each observation positions. Three fluorescents intensity profiles were measured per imaging position by using ImageJ then averaged in a custom Python program. Streamline width was defined as fluorescent intensity FWHM (full width at half maximum) across channel width at each position where the intensity profile above 10% threshold to avoid channel edge reflection interferences. Focusing was defined as the streamline FWHM was smaller than 2 \times the particle diameter. The particle probability density along the channel height is an empirical function plotted by kernel estimator in R software (RStudio Team) from hundreds of single particle vertical position. OriginPro (OriginLab Corporation, USA) was used to analyze data and plot results.

3.2.5 Numerical Models

COMSOL Multiphysics 5.6® was used to model evolution of flow variables. Only the steady-state flow fields without particles were modeled. To overcome convergence issues due to

high Wi number ($Wi > 9$) at flowrates $Q > 100 \mu\text{L}/\text{min}$, only a segment of spiral channel was modeled with appropriate periodic boundary condition. Due to the symmetric nature of the flow with respect to the z-axis, the simulations were performed only for the lower half of the channel using the symmetry boundary condition to reduce computational cost. Stationary laminar flow equations [Eq. 1-2] were solved with *Giesekus* model as the constitutive equation¹⁰⁶ [Eq. 11-12] to capture the viscoelastic and shear-thinning behaviors of the PEO solution^{39,107,108}:

$$\rho(\mathbf{u} \cdot \nabla)\mathbf{u} = \nabla \cdot (-p\mathbf{I} + \mu_s(\mathbf{L} + \mathbf{L}^T) + \mathbf{T}_e) \quad (9)$$

$$\nabla \cdot \mathbf{u} = 0 \quad (10)$$

$$\lambda \dot{\mathbf{T}}_e + \left(1 + \frac{\alpha\lambda}{\mu_p} \mathbf{T}_e\right) \mathbf{T}_e = \mu_p(\mathbf{L} + \mathbf{L}^T) \quad (11)$$

$$\dot{\mathbf{T}}_e = (\mathbf{u} \cdot \nabla)\mathbf{T}_e - \mathbf{L} \cdot \mathbf{T}_e - \mathbf{T}_e \cdot \mathbf{L}^T \quad (12)$$

Here, \mathbf{u} is the velocity vector; \mathbf{L} denotes velocity gradient tensor; ρ , μ_s , and \mathbf{I} are the fluid density, solvent viscosity, and identity matrix; and \mathbf{T}_e is the extra elastic stress tensor; $\dot{\mathbf{T}}_e$ is the upper-convective time derivative. In the *Giesekus* model, λ and μ_p are the relaxation time and the viscosity of polymer part of the fluid, and α is the mobility factor related to shear-thinning¹⁰⁹. A global ODE equation was added to the model to generate the desired flowrate by adjusting the pressure difference between the segment inlet and outlet. A tetrahedral mesh with 126,000 elements was used to discretize the domain and the spiral segment length was fixed at $\pi/20$ radians. Mesh configuration details are given in **Fig. 6**. Dependency of simulation results on the number of mesh elements and the spiral segment length were assessed by plotting radial velocity along half the channel height in a convergence test; these results are provided in **Fig. 7**.

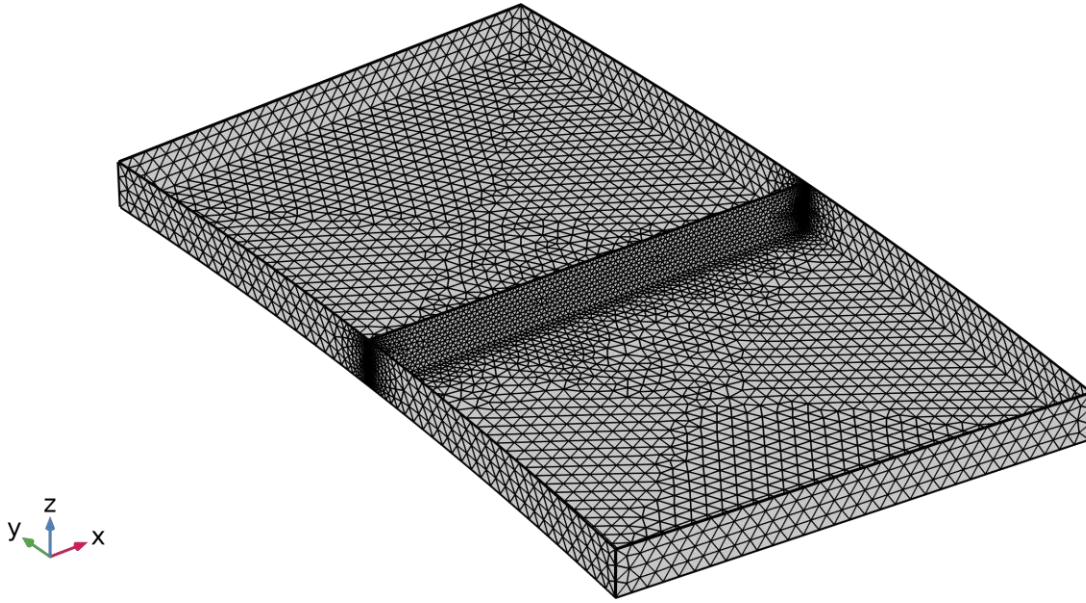


Figure 6. Model mesh configuration. Finer mesh was used in the cross-section of interest.

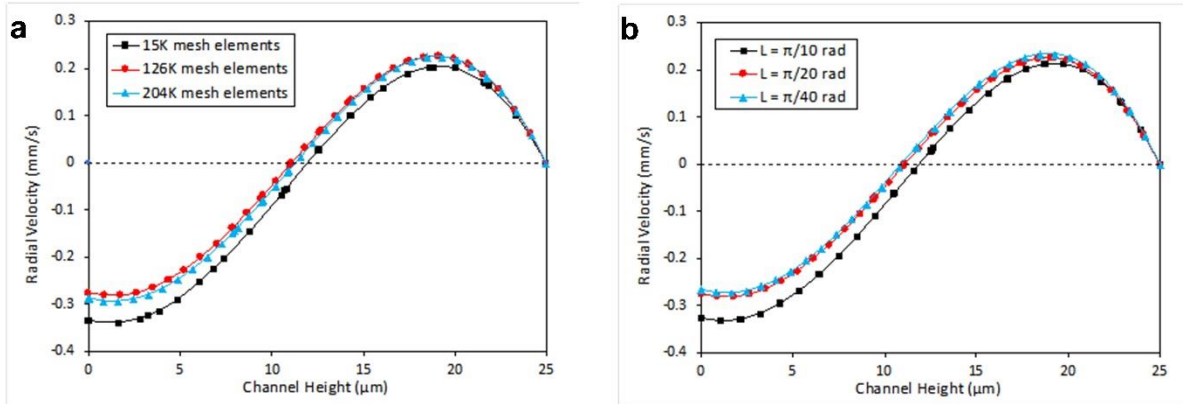


Figure 7. Dependency of simulation results on the number of mesh elements and the spiral segment length by plotting radial velocity along half the channel height. (a) three different mesh configurations with 15000, 126000, and 204000 number of elements were evaluated, and the mesh-independency was observed beyond 126K elements. (b) Segment lengths of $\pi/10$, $\pi/20$ and $\pi/40$ were simulated; channel length of $\pi/20$ ensured independence of the results from the domain length and provided longest possible channel segment for the flow to develop.

3.3 Results and Discussion

3.3.1 Operation of Spiral Devices

Particle migration in spiral channels has been reviewed by us^{17,110} and others.^{111,112} In viscoelastic fluids, it is dependent on interaction of three hydrodynamic forces: inertial lift force, curvature-induced Dean drag force, and elastic force. It is well accepted now that inertial focusing occurs when particle Reynolds number $Re_p \geq 1$ ³⁰ ($Re_p = Re(a/D_h)^2 = \rho U_f a^2 / \mu D_h$ where Re is the channel Reynolds number, U_f is the average fluid flow velocity, a is the particle diameter, ρ is the fluid density, μ is the fluid viscosity, and D_h is the hydraulic diameter of the channel). As particles flow downstream, they experience a inertial lift force F_s induced by fluid shear, as well as wall-induced lift force F_w generated by the interaction of particles and channel walls. These forces scale strongly with particle diameter and the location in channel, with the total net lift force F_L acting on particles as $F_L \propto \rho U_f^2 a^2 / D_h^2$ near the channel center, and as $F_L \propto \rho U_f^2 a^6 / D_h^4$ near the channel wall³⁰. In addition to inertial lift, particles in viscoelastic fluid are subject to the elastic force, which is the strongest at channel walls and is the weakest at the centerline and corners⁸³. The interaction between elastic and inertial forces results in an equilibrium position near channel centerline¹¹³. The non-dimensional Weissenberg number (Wi) is used to describe viscoelasticity of the fluid and is given as $Wi = \lambda \dot{\gamma}$, where $\dot{\gamma}$ is flow shear rate and λ is fluid relaxation time. The elasticity number (El) indicates the relative importance of the elastic and inertial forces in shear flows³⁵ and is given as $El = Wi/Re$. When $El \gg 1$, the fluid elastic force dominates, while inertial stress is dominant when $El \ll 1$. For Newtonian fluids, $\lambda = 0$, and thus $Wi = 0$ and consequently $El = 0$, indicating dominance of inertial effects.

Radial centrifugal acceleration of fluid in spiral microchannels leads to formation of two counter-rotating vortices, with the magnitude of flow described by the non-dimensional Dean

number (De) as $De = Re \sqrt{\frac{D_h}{2R}}$, where R is the radius of curvature. Particles entrained in these vortices are subject to Dean drag force F_D , and near the top and bottom walls in low aspect ratio channels the inertial lift forces are orthogonal, and thus do not disrupt particle migration within vortices. In Newtonian fluids, near the outer wall both F_D and F_L are in the same direction, and thus particles follow the Dean vortices. In this case, $F_D = 3\pi\mu a \bar{U}_{\text{Dean}} = 5.4 \times 10^{-4} \pi\mu a De^{1.63}$ (where \bar{U}_{Dean} is the average Dean velocity $\bar{U}_{\text{Dean}} = 1.8 \times 10^{-4} De^{1.63}$)^{7,82,114,115}. Near the inner wall, however, in Newtonian fluids the inertial and Dean forces act in opposite directions, leading to a possible force balance for particle focusing. In viscoelastic fluids, the elastic force is orthogonal to channel walls and thus near top and bottom walls particles too get entrained in Dean vortices. Near the inner wall, however, elastic force and Dean drag overcome the inertial lift force, and thus particles continue to follow the vortex flow. At the outer wall, the Dean drag is now counteracted by the elastic force instead of the shear-induced lift force, leading to a possible force balance for particle focusing near the center of the outer wall.^{26,27}

3.3.2 Effects of Flow Rates

Particle migration in spiral microchannels in viscoelastic fluid yields a single focusing stream at the outlet. The particle migration trajectories were collected from fluorescent streak velocimetry images of in wide range of flow rates from 50 to 350 $\mu\text{L}/\text{min}$ in the R2 spiral channel in 500 ppm PEO solution. The top-view fluorescent images in **Fig. 8** illustrate that randomly distributed particles at the inlet develop into a single stream at the outlet. Since 500 ppm PEO solution is viscoelastic, the outlet focused stream is near the channel centerline. Another key observation is that the randomly distributed particles at the inlet evolve into 3 streams within the first loop for all flow rates, although the transition occurs earlier at higher

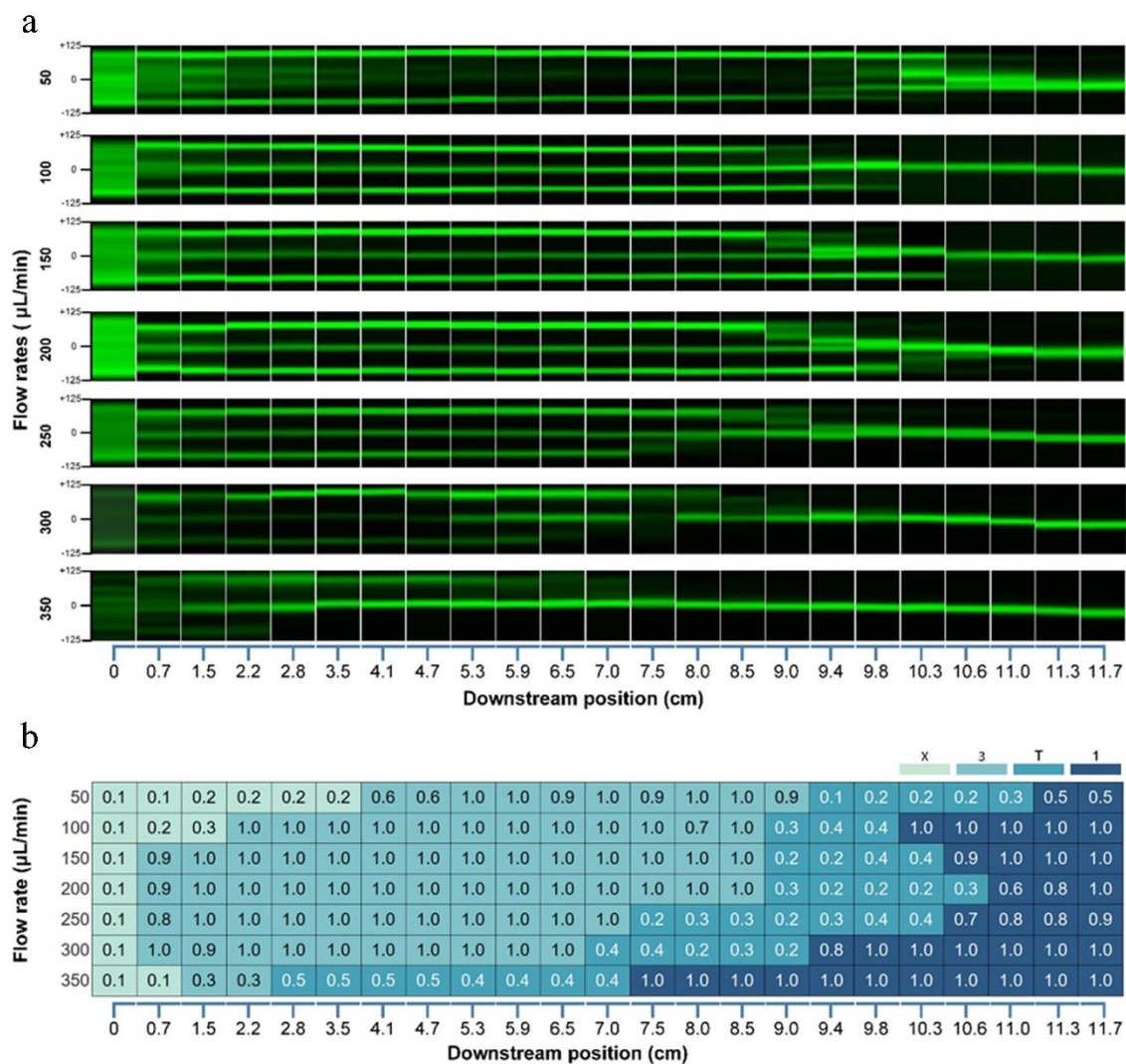


Figure. 8. Downstream evolution of particle focusing. (a) Stacked fluorescent streak images illustrating downstream evolution of particle focusing in R2 spiral channel (aspect ratio $AR = 0.2$) at 50-350 $\mu\text{L}/\text{min}$ flow rate. The ± 125 scale indicates the normalized width of the 250 μm wide channel. Downstream position is indicated at the bottom of the panel set. (b) Heat map illustrates lateral migration of particles in R2 channel. Each cell reports focusing quality ($FQ = a/\text{FWHM}$) of fluorescent streams. The color of each cell indicates the unfocused (X), three streams (3), transition (T) or single stream (1) regions.

flow rates (and thus higher De and Re). Before the 3 streams then transition into 1 at the outlet, they undergo a transition region where streams appear to merge and disappear.

While fluorescent images aid in visualizing particle trajectories at different flow rates, this work presents a heat map to quantitatively investigate focusing quality and stream evolution. Focusing quality (FQ) is the ratio of particle diameter to full width at half maximum (FWHM) of the stream intensity, and approaches zero when particles are dispersed throughout channel cross-section and reaches unity for perfect focusing. The heat map in **Fig. 8b** allows us to visualize the evolution of particle streams from random distribution (X) at the inlet, to 3 streams, and thorough a transition region (T) to a single stream, all of which appear to depend on the flow rate. Specifically, the initial transition to 3 steams is inversely proportional to flow rate, taking 5.3 cm downstream at 50 $\mu\text{L}/\text{min}$ but only 0.7 cm at 350 $\mu\text{L}/\text{min}$. This emergence of 3 distinct streamlines has been reported previously in low aspect-ratio straight¹¹⁶ and spiral⁴² channels. Further downstream, the onset of the transition to single stream appears to maintain the inverse relationship with flow rate. Transition to single stream takes place at 11.3 cm downstream at 50 $\mu\text{L}/\text{min}$ but occurs much earlier at 7.5 cm at 350 $\mu\text{L}/\text{min}$. Interestingly, although evolution to transition region (T) occurs later at low flowrate, the length of the transition region appears to be much shorted than at the higher flowrates.

3.3.3 Effects of Flow Direction

The Dean number is inversely proportional to the square root of the radius of curvature. In a planar spiral channel, the De of the inner loop is higher than De of the outer loop. Consequently, particles that enter channel at the center inlet will experience a slowly decreasing Dean number. Conversely, particles that enter channel from the outside loop will experiences a slowly increasing Dean number. Since Dean drag force magnitude is dependent on the Dean

number, as $F_D \sim De^{1.63}$,²⁹ the balance of inertial, viscous, and Dean forces that determines the particle stream lateral position and focusing quality changes with downstream position. Most of the inertial spiral devices reported in literature used for cell or particle sorting flow sample from inside out, often due to device design that must accommodate large multifaceted outputs. However, devices that do not require large output structures and are used primarily for cell or particle focusing, can flow sample in either direction. Indeed, the outside-in flow direction maybe advantageous as gradually increasing Dean number may improve focusing quality and thus device performance.

To investigate impact of the flow direction, the particles were flowed in inside-out and outside-in directions (inlet and outlet reversed) in R2 spiral device at 100 $\mu\text{L}/\text{min}$ (low) and 250 $\mu\text{L}/\text{min}$ (high) flowrates. Comparing evolution of particle streams in both channel directions at the two flowrates, presented in **Fig. 9a-b**, a number of observations emerge. First, for the increasing Dean number flow (outside-in), lateral position of the single particle stream near the end of the channel gradually shifts towards the inner-wall at both flowrates, whereas the lateral position of the single particle stream slightly shifts toward the outer-wall for the decreasing Dean number flow (inside-out). Second, in the transition region of the increasing Dean number flow (outside-in), the outer stream is the first to migrate toward the center at low 100 $\mu\text{L}/\text{min}$ flowrate. Increasing flowrate to 250 $\mu\text{L}/\text{min}$ causes the reverse – the inner stream is the first to migrate to the center, with the outer stream beginning its migration nearly 2 cm downstream. For the decreasing Dean number flow (inside-out), the reverse occurs at each flowrate. Specifically, at 100 $\mu\text{L}/\text{min}$ the inner stream migrates toward the center first, while the outer stream is the first to migrate at 250 $\mu\text{L}/\text{min}$.

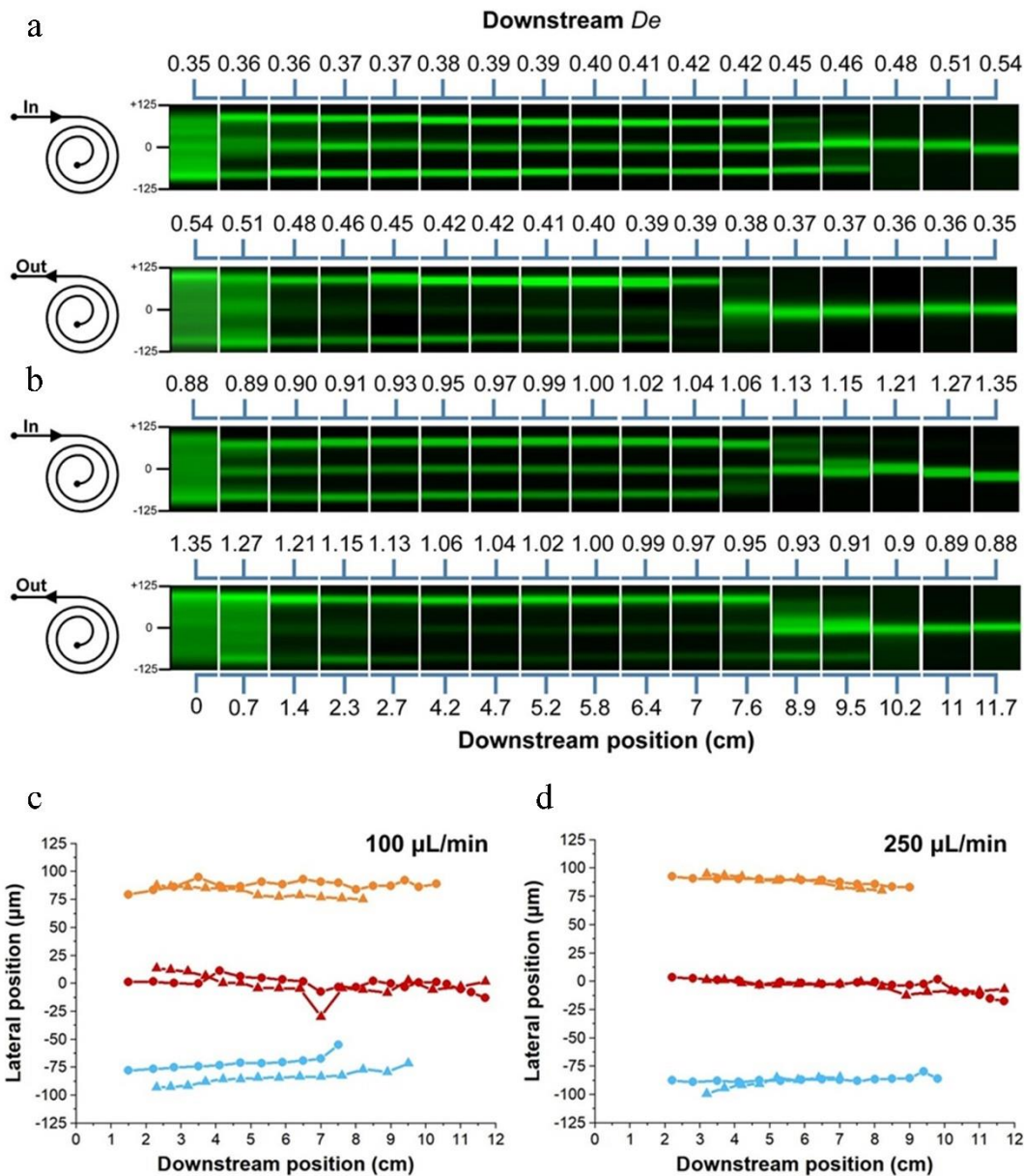


Figure 9. Flow direction effects on particle lateral migration. Fluorescent streak images illustrating downstream evolution of particle focusing for opposite flow directions in R2 at (a) 100 $\mu\text{L}/\text{min}$ and (b) 250 $\mu\text{L}/\text{min}$. Downstream position label is at the bottom, while the corresponding Dean number (De) is at the top of each panel set. Device icons on left indicate flow direction. Lateral position of particle streams evolving downstream of the microchannel at (c) 100 $\mu\text{L}/\text{min}$ and (d) 250 $\mu\text{L}/\text{min}$ flows. Blue is the inner stream, red is the central stream, and yellow is the outer stream. Circles represent data for inside-out flow direction, while triangles represent data for outside-in flow direction.

To better compare impact of flow direction, **Fig. 9c-d** illustrates the position of the streams in the downstream direction at 100 $\mu\text{L}/\text{min}$ (low) and 250 $\mu\text{L}/\text{min}$ (high) flow rates for both increasing and decreasing Dean number flows. The data were plotted as circles for inside-out flow direction and as triangles for outside-in flow direction. The inner, central and outer streams are represented with blue, red and yellow lines, respectively. These data illustrate that at both flowrates and regardless of flow direction, the randomly distributed particles at the inlet form three streams that subsequently merge into a single central stream at the outlet. At low flowrate, the streams near channel sidewalls appear at approximately 100 μm away from centerline, with both merging into the central stream by 10 cm downstream. Increasing the flow rate causes these side streams to shift closer to the center, to approximately 75 μm away from centerline, with both again merging into the central stream by 10 cm downstream. Thus, we conclude that reversing direction of flow in these spiral microfluidic devices yields the same overall focusing behavior at the outlet.

3.3.4 Particle Migration along the Channel Height

This work next investigated migration of particles along channel height near outlet. It has been suggested by Toner¹¹⁷ and others¹¹⁸ that two focusing positions near each other are present at the outlet in inertial flows. In viscoelastic flows, however, this remains unclear due to lack of direct observations. Additionally, the side-view imaging can aid in explaining the observed 3-T-1 focusing behavior. Thus, the spiral microchannels were vertically mounted to visualize particle focusing along channel sidewalls at the outlet. A similar approach was used by us¹⁰ and others¹¹⁸ in the past to visualize particle focusing in the side view. Due to the bonding strength of the vertical mount, the flow rates were limited to below 250 $\mu\text{L}/\text{min}$. To investigate the particle focusing behavior in 500 ppm PEO ($El = 2.6$) along the channel height, it is necessary to collect

the particle probability density (PPD) obtained from bright field side-view images, which is analogous to line scan in fluorescent images, is presented in **Fig. 10a** for the R2 channel at 50-250 $\mu\text{L}/\text{min}$ inside-out flows. The stacked bright-field image inset at 100 $\mu\text{L}/\text{min}$ confirms the presence of two streams for each of the streams observed in top view images in **Fig. 8a**, suggesting 6 positions in the 3-stream stage and 2 positions at the 1-stream stage in the cross-section. At a lower flow rate, the particles appear as a board and poorly focused $\sim 30\ \mu\text{m}$ wide stream. At flow rate $>100\ \mu\text{L}/\text{min}$, the two distinct streams migrate closer to the centerline, with gap distance between the streams reducing from $\sim 10\ \mu\text{m}$ at 100 $\mu\text{L}/\text{min}$ to $\sim 2.5\ \mu\text{m}$ at 250 $\mu\text{L}/\text{min}$. These results confirm presence of two vertical streams in viscoelastic flow for each top view stream and differ from the existing literature that assumes single stream in the vertical center plane. This is a key new finding that helps explain the evolution of the focusing streams.

Fig. 10b presents gap distance between the vertical peaks, suggesting that streams shift exponentially closer to the centerline with increasing flowrate at the outlet of the 11.7 cm long channel. The correlation equation for gap distance is $d\ (\mu\text{m}) = 25 e^{-0.009 Q}$ where Q ($\mu\text{L}/\text{min}$) is flowrate ($R^2 = 0.999$). The expression suggests that at $<50\ \mu\text{L}/\text{min}$ ($Re < 2$) flowrates, the gap distance would be $>15\ \mu\text{m}$, with particles located less than $5\ \mu\text{m}$ from top and bottom walls. At low flowrate, inertial lift F_L is weak and thus the particles are not vertically focused to form gaps, which matches the experimental data in **Fig. 10a** that shows particles being unfocused at the lowest flowrate. Interestingly, these data also suggest that at $>350\ \mu\text{L}/\text{min}$ ($Re > 15$) flowrate, the gap distance will reduce to $d < 0.5\ \mu\text{m}$, and thus essentially yield single stream focusing.

To explore downstream evolution of particle migration, it is necessary to measure the vertical positions of the two particle streams along channel length. The data in **Fig. 10 c-d**

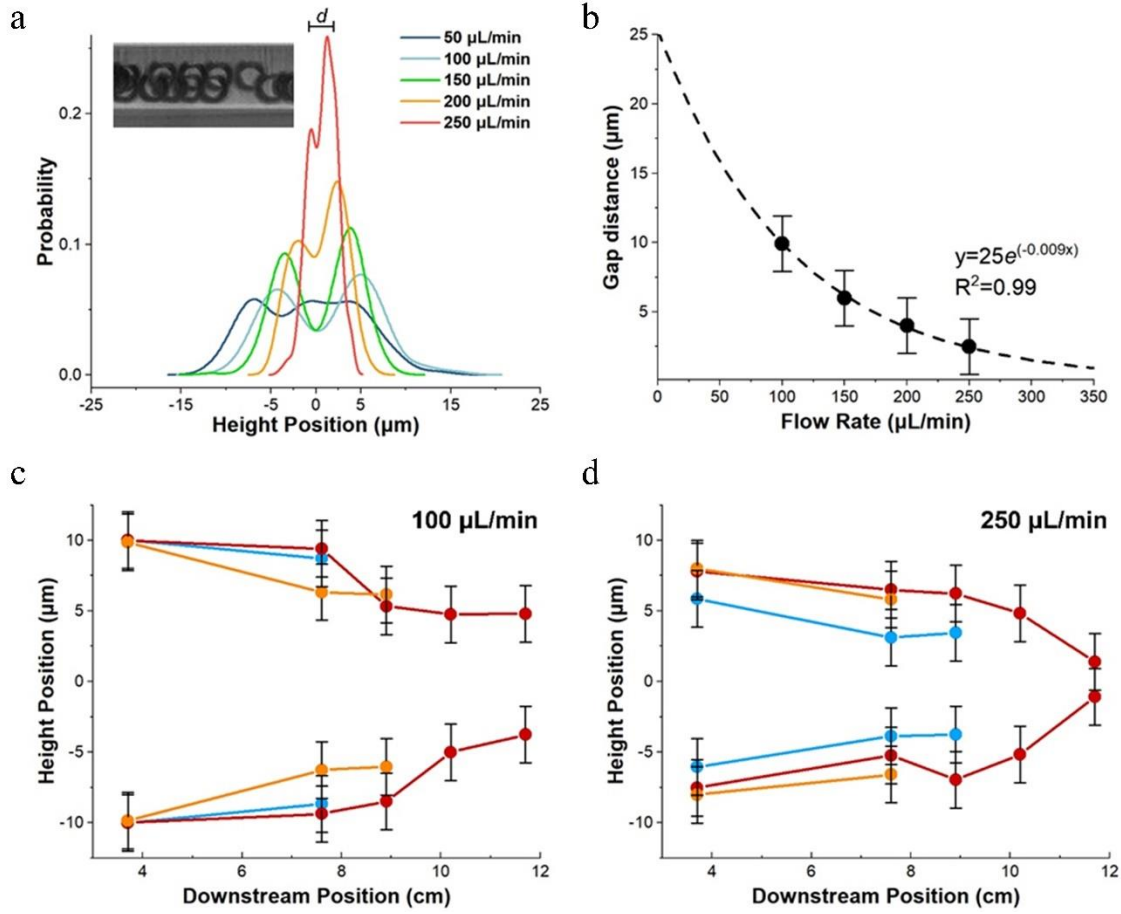


Figure.10. Vertical migration of particles. (a) Vertical position probability in R2 channel for particles flown inside-out at 50-250 $\mu\text{L/min}$. The particle vertical position is measured from the particle center to the bottom of the channel. Each plot corresponds to the particle vertical position probability based on $n=455$, $n=301$, $n=268$, and $n=291$ individual measurements, respectively. Inset illustrates a representative bright field image obtained using side view imaging at 150 $\mu\text{L/min}$. For flown outside-in, the vertical position of particle is not measurable due to the out range of microscope working distance and the reflection and refraction from adjacent channels. (b) Gap distance (d) between particle streams as a function of flow rate. Measurements of particle vertical positions as a function of downstream position at flow rates of (c) 100 $\mu\text{L/min}$ and (d) 250 $\mu\text{L/min}$. The vertical positions were measured from particle probability peaks from 100 individual measurements along the channel downstream length. The red, orange, and blue lines represent the particle position in the focal planes near the center, outer wall, and inner wall respectively. Due to channel deformation, empirical $\pm 2 \mu\text{m}$ systematical error bars added in (b), (c), and (d).

illustrate that particle streams progressively migrate toward channel centerline in the downstream direction for all the three streams observed from top view. Interestingly, the results show different toward center migration speeds at low and high flow rates for the streams near inner wall and outer wall, which coincides with opposing disappearing order of the side streams observed in the top view (**Fig. 9**). At 100 $\mu\text{L}/\text{min}$, the side streams near outer wall migrate faster toward the center vertically than those near the inner wall. Note that near the vertical center plane the Dean drag is toward the outer wall, which prevents the disappearance of the outer streams and leads to the later merging of the outer streams. On the other hand, at higher flowrate, these side streams near the outer wall are closer to the top and bottom wall where Dean drag is toward the center, which leads to the fast merging of these streams to the center streams observed from top view. Additionally, these results indicate that the two particle streams migrate toward centerline at a faster rate at higher flow. The results also suggest that longer spiral channels will yield vertical streams closer to each other. For example, for the two particle streams to migrate to only 1 μm separation, at 100 $\mu\text{L}/\text{min}$ full 25 cm downstream will be required but at 250 $\mu\text{L}/\text{min}$ only 17 cm is necessary.

3.3.5 Effects of Curvature

Fluorescent streak velocimetry illustrates that curvature, as expected, significantly impacts particle migration in spiral channels (**Fig. 11a**). This work tested the devices with radii of curvature ranging from 1 mm (R1) to 6 mm (R6) with the same cross-section (250 μm wide \times 50 μm high) at 50~350 $\mu\text{L}/\text{min}$ in 500 ppm PEO ($El \sim 2.6$). To decouple the downstream and curvatures effects on particle lateral migration, channel length was fixed at 8cm. The results demonstrated that in larger curvature devices (R4 and R6), the smaller effects of F_D , particles are

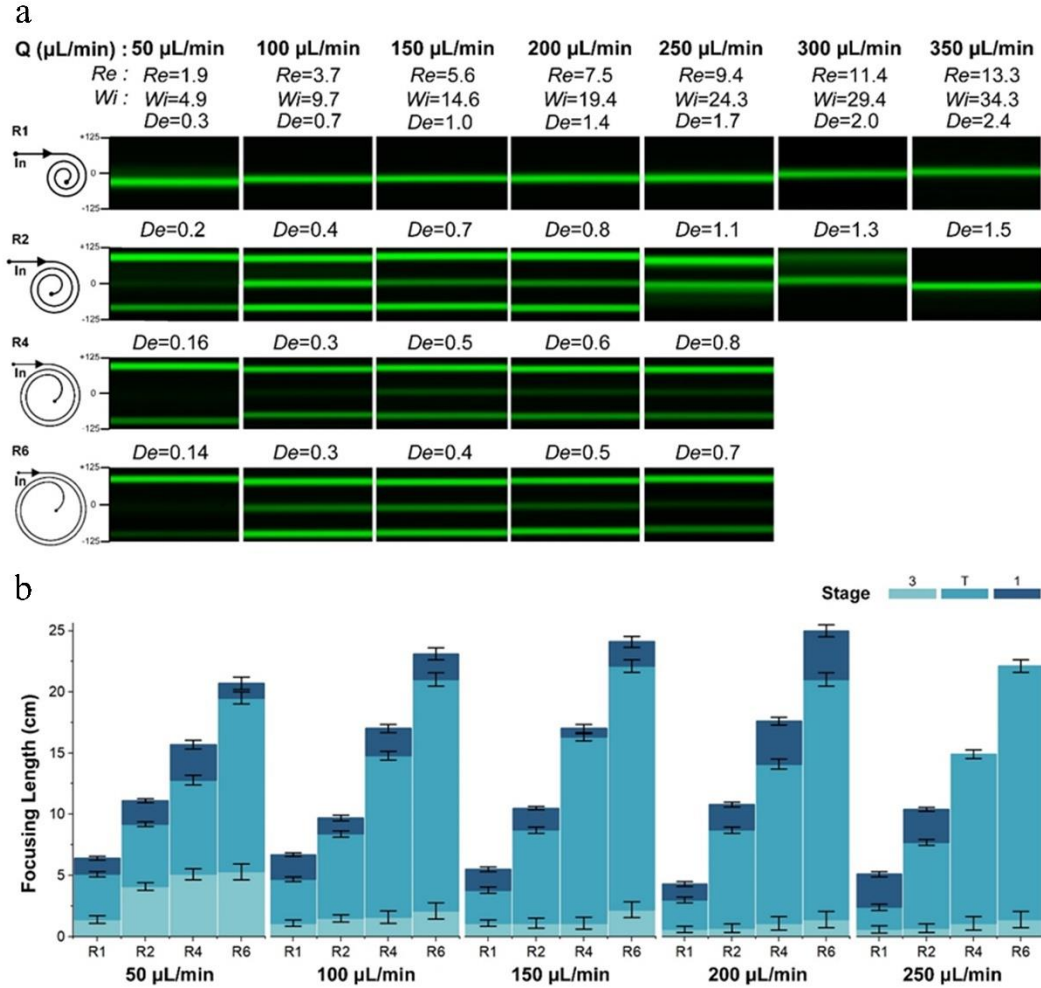


Figure. 11. Curvature effects on particle focusing. (a) Fluorescent images demonstrate particle trajectories in four devices (R1, R2, R4, and R6) at 8cm downstream in 500 ppm PEO at 50 - 350 μL/min. The flow parameters are at the top of each column. The corresponding De , which changes with curvature, is at the top of the fluorescent images. (b) Bar plots illustrating downstream migration distance to evolve three or one streams for 50 - 250 μL/min. Error bars indicate $\frac{1}{4}$ loop length from the observed position.

streams near the sidewalls dismissed and refocused near the centerline of the channel with confined in three distinct streams near channel sidewalls and centerline for flowrates 50 to 250 $\mu\text{L}/\text{min}$. In smaller curvature devices (R1 and R2), the stronger effects of F_D , particle streams reduce to a single one near the centerline. However, in the larger curvature devices (R4 and R6), where migration is at the same Re but at smaller De , particles persist in three streams. This suggests that the persistent three streams are resulted by the inertial-elastic interaction. These results agree with observations reported by Xiang *et al.*⁴². In R1 device, particle equilibrium progressively shifts from the inner wall to the outer wall with increasing flow rate. This suggests that curvature induced Dean effect contributed to the particle lateral migration, yielding particle increasing De (smaller radius of curvature).

Examining focusing length at 50 $\mu\text{L}/\text{min}$ to 250 $\mu\text{L}/\text{min}$ for each device curvature (**Fig. 11b**) reveals that smaller curvature devices require shorter downstream length to produce a single stream. This suggests particles rapidly move into three streams from random distribution at the inlet, indicating fast lateral migration velocity occurring at first. At fixed length of the spiral channel, the smaller inner-most curvature provides stronger Dean effects and the multiple stream positions reduce to one. At 250 $\mu\text{L}/\text{min}$, we found that at same flow rate and downstream length with increasing De , particles initially migrated into three streamlines transitionally appeared two streams near the centerline in R2, finally migrated into a single stream near the channel centerline in device R1. This matches the results discussed above where increasing De leads to reduction of multiple streamlines to one and improvement in focusing quality.

Examining focusing length at 50 $\mu\text{L}/\text{min}$ to 250 $\mu\text{L}/\text{min}$ for each device curvature (**Fig. 11b**) reveals that smaller curvature devices require shorter downstream length to produce a single stream. This suggests particles rapidly move into three streams from random distribution

at the inlet, indicating fast lateral migration velocity occurring at first. At fixed length of the spiral channel, the smaller inner-most curvature provides stronger Dean effects and the multiple stream positions reduce to one. At 250 $\mu\text{L}/\text{min}$, we found that at same flow rate and downstream length with increasing De , particles initially migrated into three streamlines transitionally appeared two streams near the centerline in R2, finally migrated into a single stream near the channel centerline in device R1. This matches the results discussed above where increasing De leads to reduction of multiple streamlines to one and improvement in focusing quality.

To explore evolution in a larger curvature device, we extended the downstream length from inlets to outlets and plotted the particle trajectories heat map of devices R1, R4 and R6 in **Fig. 12**. At high flow rates, particles begin migrating to their final equilibrium position near centerline in R4 and R6. This observation was similar to the R2 device at low flow rates. As discussed above, the particle rapidly migrated from the channel bulk toward the centerline under the influence of elastic force and inertial lift force. The dominated elastic force along channel height pre-focused and aligned particle near centerline. On the other hand, because of the velocity profile, the shear gradient lift force pushed the particles away from the center towards the channel walls and the particles were finally focused at both the side walls. This confirmed that the particle equilibrium position strongly depended on device curvature and that Dean effects played an important role on particle migration, which is in agreement with earlier observations in **Fig. 8**.

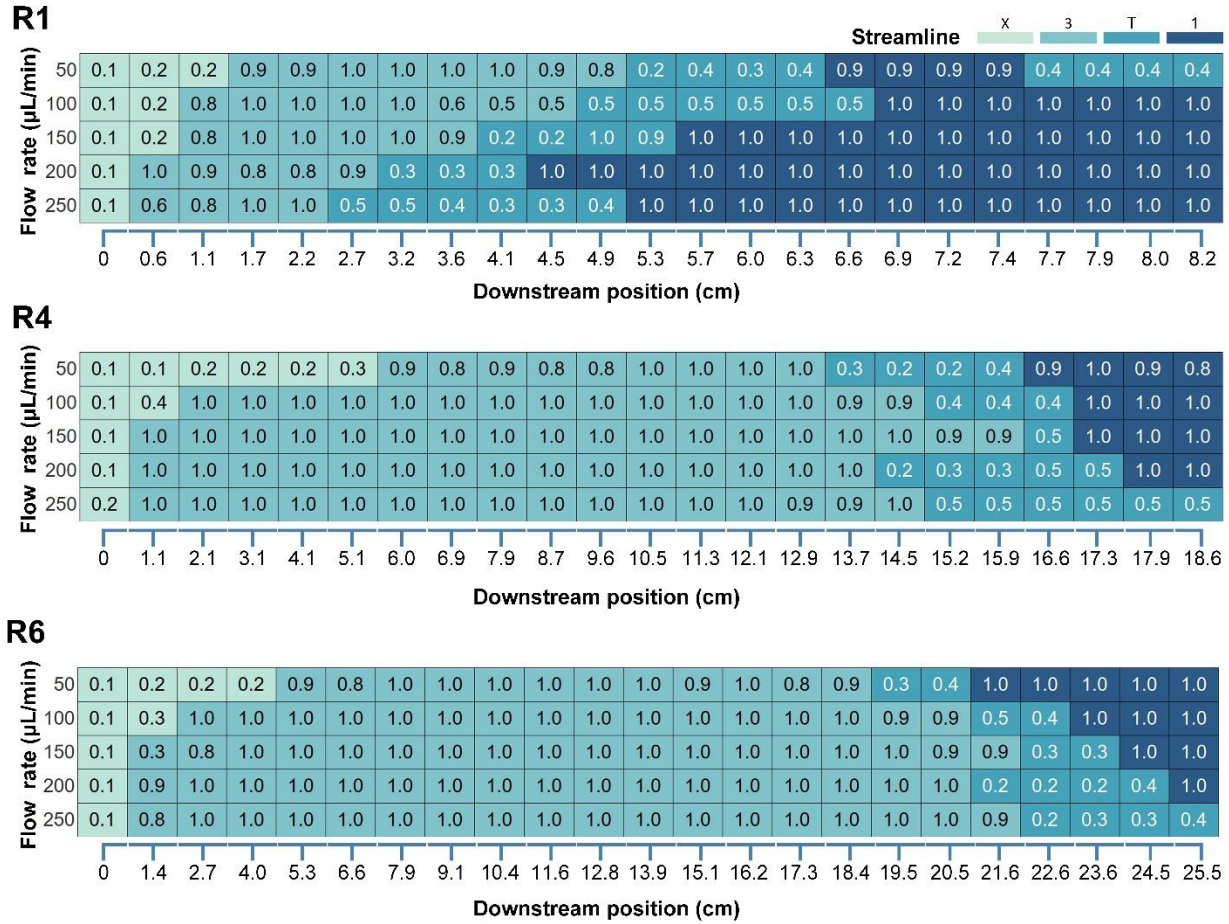


Figure.12. Particle migration and focusing in R1, R2, R4, and R6. Heat map illustrates the evolution of particle focusing streams. Each cell reports focusing quality ($FQ = a/FWHM$) of fluorescent streams. The color of each cell indicates the unfocused (X), three stream (3), transition (T) or single stream (1) regions.

3.3.6 Effects of Elasticity

Viscoelastic migration and equilibrium position of particles is strongly associated with the medium elasticity^{39,41}. The elastic number is independent of flow rate and only depends on fluid properties and device geometry. To investigate effects of fluid elasticity, we evaluated particle migration in DI water with 5% NaCl (pure inertial flow, $El = 0$), and PEO solutions at 0 - 5000 ppm ($El = 0 - 117$) with 22% glycerol representing elasto-inertial and purely viscoelastic

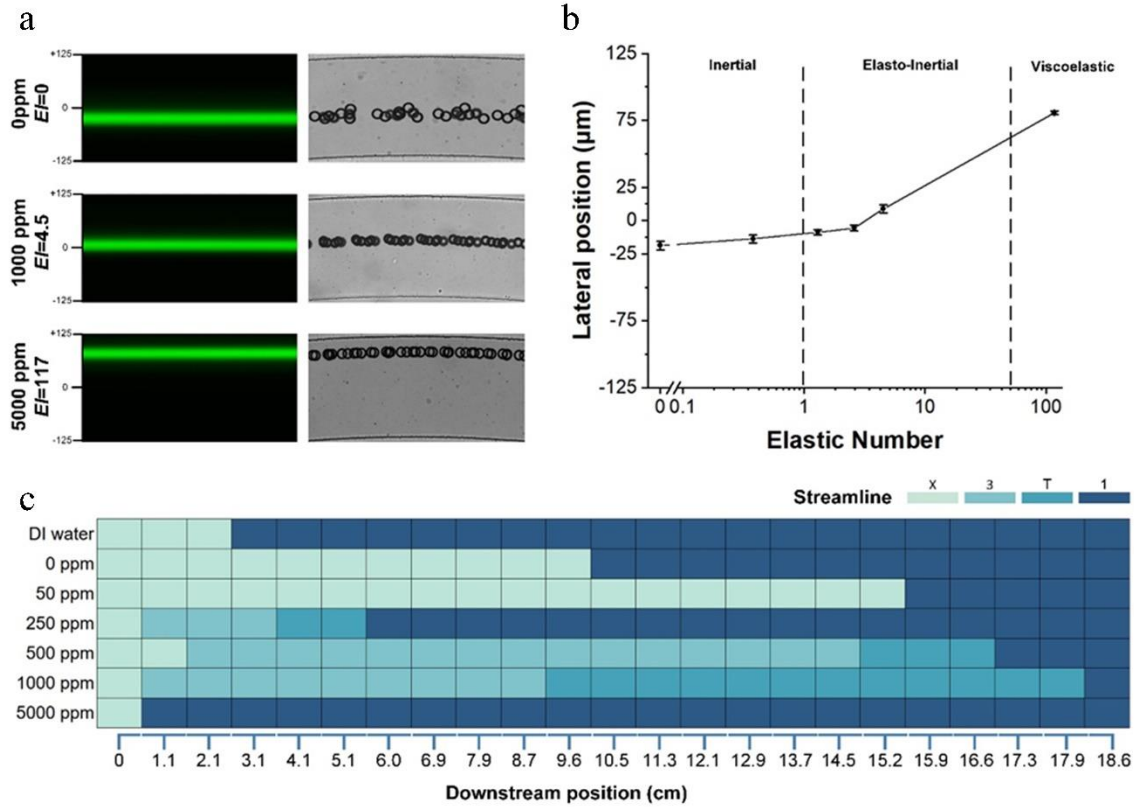


Figure. 13. Elasticity effects on particle focusing. (a) Fluorescent and bright-field images of particle focusing in 0 ppm, 500 ppm, and 5000 ppm PEO solutions observed at the outlet. (b) Single stream focusing lateral position as a function of elastic number. (c) Heat map illustrates evolution of particle focusing downstream the channel (indicated below) in varying PEO concentrations. In DI, DI +22% glycerin, and 50 ppm PEO, particles focus near the inner-half of the channel and progressively move toward inner-wall, illustrating inertial flow regime. In elasto-inertial flow regime, particles initially focus into three streams, then transition into two streams, and finally focus into a single stream. In viscoelastic flow regime, at 5000 ppm PEO, particles rapidly evolve into a single stream.

flows ($El = 117$). The PEO concentration was used to adjust elasticity rather than scaling device geometries in order to decouple these effects. The fluorescent streak velocimetry images and the corresponding bright field images of particle distribution at the outlet of a R4 device at 100 $\mu\text{L}/\text{min}$ in low (0 ppm PEO at $Re=5.7$, $Wi=0$, $De=0.6$), medium (1000 ppm PEO at $Re=2.9$, $Wi=13.2$, $De=0.3$), and high (5000 ppm PEO at $Re=0.36$, $Wi=42.7$, $De=0.04$) elastic media are illustrated in **Fig. 13a**. The results show that at 0 ppm PEO (pure inertial flow, $El = 0$), as expected the particles focus off-center towards the inner wall. In the elasto-inertial flow at 1000 ppm PEO ($El = 2.6$), the focused stream is at the channel centerline. Increasing fluid elasticity to 5000 ppm PEO (purely viscoelastic flow, $El = 117$) shifts the focused stream toward the outer channel wall. Measurements of lateral positions of particles as a function of El over a broader range in **Fig. 13b** confirm this observation. These measurements also suggest that elastic force begins to influence particle migration at approximately $El > 1$, with inertial effects mostly dissipating at $El > 10$. We then conclude that $1 < El < 50$ is the range for the elasto-inertial flow. The heat map of particle lateral position along the channel downstream in varying concentration of PEO solution is shown in **Fig. 13c**. When $El < 1$ (for < 50 ppm PEO solutions), the heat map shows that particles progressively form two streams along the channel downstream. In this inertial fluid regime, the oppositely directed Dean drag F_D and inertial lift F_L forces equilibrate off-center, closer to the inner half of the channel.⁸⁰ When $1 < El < 50$, particles initially focused into three streams transition to one stream. In this elasto-inertial fluid regime, the elastic force F_E balances inertial lift F_L and Dean drag F_D , resulting in equilibrium position at the channel centerline. When $El > 50$, particles rapidly migrate into a single stream (at 0.7 cm downstream) and gradually move toward the outer wall along the downstream length, as De gradually increases. In this viscoelastic fluid regime, the elastic force F_E completely dominates in the

vertical direction as inertial force is negligible ($Re = 0.36$ and $El = 117$ for 5000 ppm PEO), leading to the particle focusing in the vertical center plane where Dean drag F_D continuously drives the particles toward the outer wall.

3.3.7 General Focusing Mechanics

Fig. 14 illustrates numerical predictions of the velocity fields of secondary flows due to Dean and elastic forces in the spiral channel cross-sections, with the diagrams indicating the key forces involved in particle equilibration. As these numerical results show, the secondary flow in the elasto-inertial case is different from that in the inertial flow where two counter-rotating vortices are developed. Here, vortices are modified due to the fluid elasticity (due to N_2), leading to lateral asymmetry of velocity magnitude in secondary flow. The secondary flow is stronger near the inner wall. Note that the blockage ratio is relatively large in this work. Therefore, particles span both arms of the vortex and thus it is the net force of the two opposing Dean drag forces must be considered to determine the lateral position of the focused stream.

Particle focusing in spiral channels manifests in three major stages in the elasto-inertial flow. Randomly distributed particles rapidly form three distinct streams observed from the top of the channels (Stage 3 in **Fig. 8**). In this stage, the three streams persist, while the side streams gradually migrate toward the center. Here, presence of the elastic force modifies the focusing patterns in the cross-section by balancing the shear induced lift force in the vertical direction. This is illustrated in **Fig. 14a**. Next, in the transition stage (Stage T in **Fig. 8**), the side streams rapidly merge into the central stream, marking the beginning of the final stage where particles appear in the single stream. This evolution of the 3-stage particle focusing throughout the spiral channel is result of the interaction of inertial, drag, and elastic forces. For

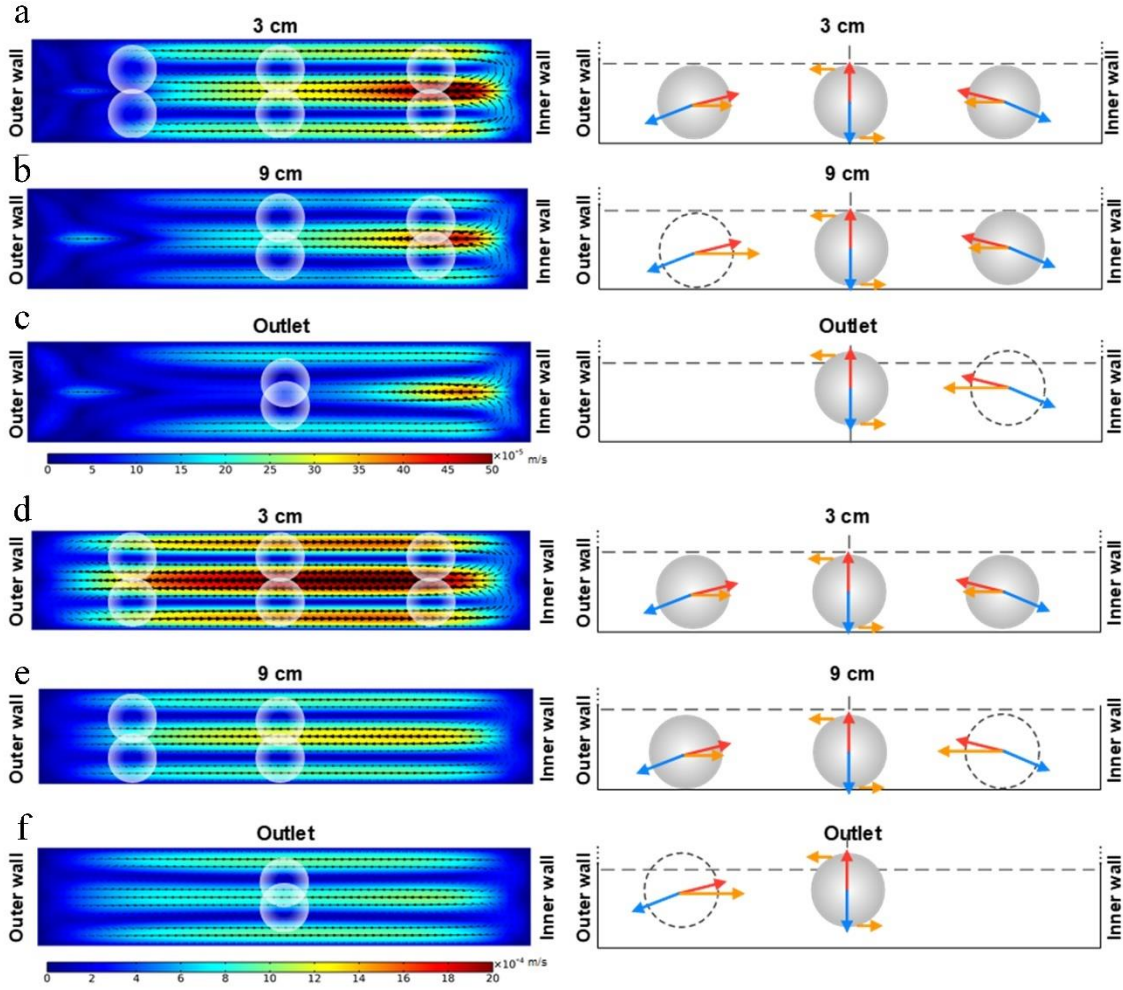


Figure. 14. Evolution of particle migration in elasto-inertial flow in spiral microchannel. Numerical results of the velocity fields of secondary flows due to Dean and elastic forces (left) and schematic diagram (right) illustrating positions of focused particles and the force balance in R2 channel with aspect ratio $AR = 0.2$. Results are for low flow rate ($100 \mu\text{L}/\text{min}$) at (a) 3 cm, (b) 9 cm, and (c) Outlet downstream positions, as well as for high flow rate ($250 \mu\text{L}/\text{min}$) at (d) 3 cm, (e) 9 cm, and (f) Outlet downstream positions. Blue, red, and orange arrows indicate inertial lift F_L , elastic force F_E , and drag force F_D , respectively. Only bottom half of the channel in the schematic is shown due to symmetry.

the particles focused in the stream near the outer wall, the net drag force is toward the channel center. This net force is responsible for the toward-center migration of the outer streams observed in top view (**Fig. 8**). According to the simulation, Dean flow dominates at higher flow rate (e.g., 250 $\mu\text{L}/\text{min}$) while the modification of the secondary flow due to fluid elasticity is significant at low flow rate (e.g., 100 $\mu\text{L}/\text{min}$). Such change of the secondary flow alters the relative intensity of F_D near channel center and near channel bottom/top. And due to high blockage ratio, particles near channel sidewalls experience differing degrees of drag, leading to different disappearance sequences of the side streams observed in the transition stage between the low and high flow rate cases (**Fig. 14 b/e**). The high blockage ratio of the 25 μm beads in our 50 μm high channel ($\beta = 0.3$ since $D_h = 83.3 \mu\text{m}$) means that beads span both the top and bottom portion of each of the Dean vortices, as illustrated in numerical results of **Fig. 15**. The smaller 15 μm beads, which occupy 60% of channel half height and have a blockage ratio of $\beta = 0.18$, still follow the same pattern of focusing dynamics (**Fig. 15**). The smaller 7.32 μm beads, which span only 29% of channel half height and have a blockage ratio of $\beta = 0.088$, no longer follow the described pattern.

3.4. Summary

In this work, for the first time, we experimentally demonstrated evolution of particle focusing behavior along channel downstream length at high blockage ratio. We discovered that the vertically movement of the particles closely coordinated with their lateral migration, leading to slightly different focusing behavior depending on the flowrate and flow direction. We found that flow rate, device curvature, minimum De , and medium viscosity play an important role in particle lateral migration. Our results illustrate the full focusing pattern along the downstream

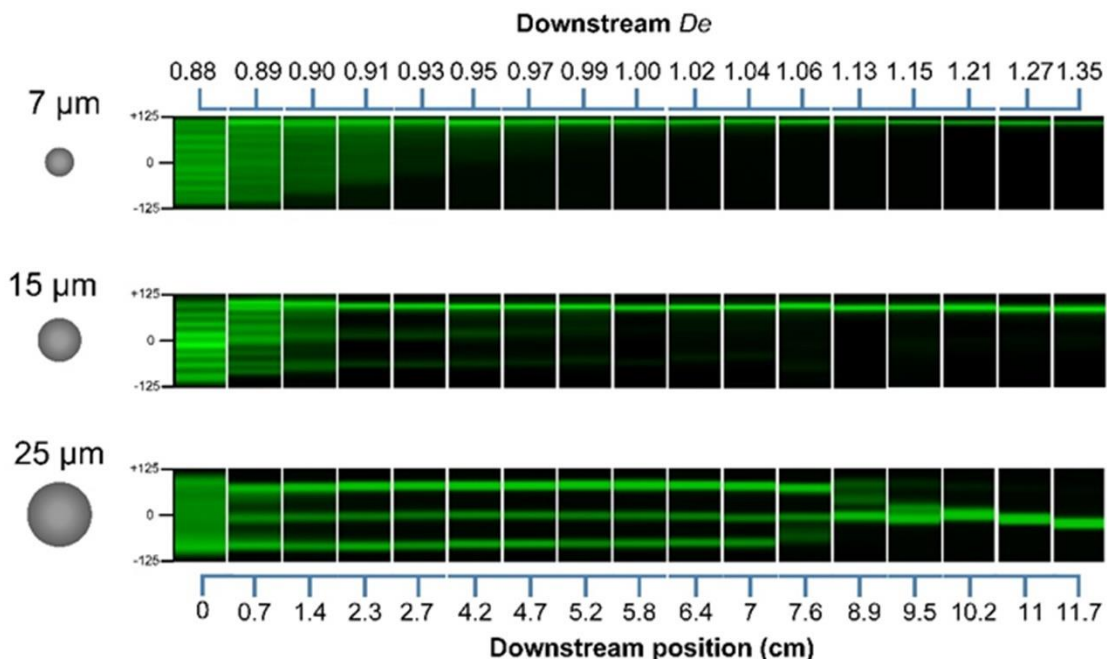


Figure. 15. Downstream evolution of focusing for 7.32 μm , 15 μm , and 25 μm diameter beads. Stacked fluorescent streak images illustrating downstream evolution of particle focusing in R2 spiral channel (aspect ratio $AR = 0.2$) at 250 $\mu\text{L}/\text{min}$ flow rate in 500 ppm PEO solution. The ± 125 scale indicates the normalized width of the 250 μm wide channel. Downstream position is indicated at the bottom of the panel set.

channel length. Additionally, the simulation results sequentially predict that secondary flow dynamics in channel cross-section is due to the combined effects of the Dean and N2-induced secondary vortices along the channel downstream. Analyses of the particle lateral and vertical migration evolution demonstrated the underlying hydraulic forces balance. Ultimately, we anticipate that these results will offer a useful guide on elasto-inertial microfluidics device design for improving efficiency of 3D focusing in cell sorting and cytometry applications.

CHAPTER 4

FOCUSING DYNAMICS OF ASYMMETRIC CELLS IN SPIRAL CHANNELS

4.1 Introduction

The conventional semen analysis on sperm cell number, morphology, and motility is evaluated by light microscopy. Flow cytometers and the wide range of biomarkers for cell structure and function have allowed to measure more critical parameters in sperm, such as viability, fertilization capacity, or chromosomal sex¹¹⁹. However, due to the asymmetric shape and the high index of refraction of sperm cells, the emission intensity from the narrow edge is approximately twice that of the flat face and the edge intensity varies sharply with angle¹²⁰. Therefore, precise manipulation of sperm cell position, focusing, and alignment are essential for *in vitro* fertilization (IVF) and artificial insemination.

Microfluidics based particle and cell sorting devices have been utilized in sperm cell sorting¹²¹, isolation¹²² and enrichment¹²³. However, their attention has been on applications rather than on the underlying principles of sperm cell migration. Further, the majority of the previous work on cell sorting were demonstrated by spherical particles. However, the sperm cell consists a larger asymmetrical head and long-thin tail which alternates the focusing dynamics in flow and impacts the sorting efficiencies¹²². . Therefore, it is important to improve the understanding of mechanism of the sperm cell migration in spiral microchannels, including the shape, size, and orientation effects, which offer a useful guide for inertia microfluidics device

design.

Further, the majority of the previous work on cell sorting has been demonstrated by symmetric particles. However, large portion of cells are asymmetric. Due to the limited source of asymmetrical and cell-like shape particles, it is difficult to explore the shape effects and not ideally to mimic cells migration by using the spherical particles. Therefore, spermatozoa cells will be used in viscoelastic and inertial fluids and to investigate the mechanism of asymmetrical shape effects on lateral migration. In this work, we aim to improve the understanding of the underlying mechanisms of sperm cells migration in spiral channels. Using spiral microfluidic channels described earlier, we investigate migration of sperm cells, both laterally and vertically, over a wide range of flow parameters. Spherical polymer particles are used as controls. Our results demonstrate that a critical Dean number determines the migration direction of sperm cells as well as their orientation. Ultimately, we anticipate that these results will offer a useful guide on microfluidic device design for improving efficiency of 3D focusing in sperm cells sorting and cytometry applications.

4.2 Experimental Methods

4.2.1 Sperm Cell Morphology

Sixteen adult male bovine spermatozoa samples (n=16) were used to measure morphology of the bovine sperm cells. The raw bovine samples post collection were kept in 10 mL plastic tubes and shipped overnight in temperature insulated box (ThermoSafe, Inc., USA). Upon receipt, samples were warmed to 34 °C in a water bath for 45 min. Then, the sperm samples with cell concentration >519 M/mL were diluted in PBS to cell concentration of 2 M/mL measured from hemocytometry. Subsequently, 10 µL of diluted sperm sample was added

to a hemocytometer (Bulldog Bio, Boston, MA, USA) and bright field images were taken at 100× magnification by an inverted microscope (IX83 Olympus, Inc., USA). CellSense software (Olympus, Inc.) was used to measure morphology of sperm cells.

4.2.2 Fluorescent Label

Hoechst 33342 is a highly permeable DNA fluorescent dye, which is not intercalated with DNA helix and binds to the minor groove of the adenine-thymine regions¹²⁴. Vazquez JM *et al.* showed that Hoechst 33342 does not affect motility of spermatozoa or fertility after artificial insemination¹²⁵. To visualize migration of sperm cell within flow in microchannel, Hoechst 33342 was used to fluorescently label cell nuclei. Sperm cell loss the motility at temperature below 4 °C and loss the motility and viability at temperature above 37 °C. To maintain the motility and retain the viability of sperm cells¹²⁶, received samples were warmed to 34 °C in a water bath for 45 min and diluted to 200 M/mL using Tyrode's albumin lactate pyruvate (TALP) medium (Genus PLC, Inc.). Next, a 50 µm cell strainer (ThermoFisher Scientific, Inc.) was used to filter out large aggregates. the unexpected contamination. After filtration, Hoechst 33342 (20 mM, ThermoFisher Scientific, Inc.) was mixed with cells for 45 min at 34 °C.

4.2.3 Cell Viability

Viability of the spermatozoa before and after flow experiments was evaluated using Calcein AM/ propidium iodide (PI). The spermatozoa were incubated for 30 min at 34 °C. The spermatozoa were then diluted to 10 M/mL in PBS. To stain the sperm for viability, the diluted sample were incubated in a 600× dilution of Calcein AM (1mM, ThermoFisher Scientific, Inc.) and 3000× dilution of PI (ThermoFisher Scientific, Inc.) for 15 min at room temperature. Sample viability was calculated as the ratio of live fluorescence (green) to total live and dead

fluorescence (green + red).

4.2.4 Sperm Cell Head and Tail Isolation

A sperm cell consists of a large head and a long-thin tail. To investigate the effects of the head and tail on sperm migration in flow, we need to cleave sperm tails from the head. First, spermatozoa from adult bovine were washed twice in PBS at pH 7.4 then centrifuged at 300g (Thermo Fisher Scientific, Inc.,) for 20 min. For isolation of the tail from sperm head, the washed samples were sonicated at 25 KHz for 10s by using a microtip sonicator (Qsonica Sonicator Q500, Fisher Scientific, Inc.,). After sonication, the sample was centrifuged at 750g for 10 min at 34 °C. Next, the supernatant of the sample was removed then diluted the sample to desired concentrations in PBS.

4.2.5 Device Principle and Fabrication

Focusing sperm cells in inertial fluids is dependent on the balance of inertial lift forces. Shear gradient induced lift force, F_S , drags cells to the channel walls. As they approached closer to the channel wall, this force is balanced by the wall repulsive force, F_W , near the channel walls. In straight rectangular channel, sperm cells focused into two broad streams near the center of the channel at $Re = 88.7^{122}$.

As discussed in chapter 2, cell in spiral channel experiences two counter-rotating Dean vortices, which induced an additional transverse Dean drag force, F_D . The Dean effect on cell migration can be characterized by the Dean number (De). The F_D alternates the cell lateral equilibrium positions, leading to reduce two streams to one from top-view¹²².

Three Archimedean spiral devices were used in this work, with 150 μm , 100 μm and 75 μm width of the channel. The inner most radius of curvature (R) was 1 mm and height of the channels was fixed at 50 μm . The corresponding aspect ratio of the devices are 0.33, 0.5, and

0.67. Spacing between inner walls was set at 500 μm . A single outlet was located at the center of each spiral, while a single inlet with debris filter was located at the circumference.

Spiral devices were fabricated in polydimethylsiloxane (PDMS) using the standard soft lithography process with dry photoresist masters, as applied in previous chapter. Briefly, master mold with the designed spiral channel structures were obtained by following the dry film fabrication procedure shown in **Fig.16**. The mixed PDMS was mixed with curing agent in a 10:1

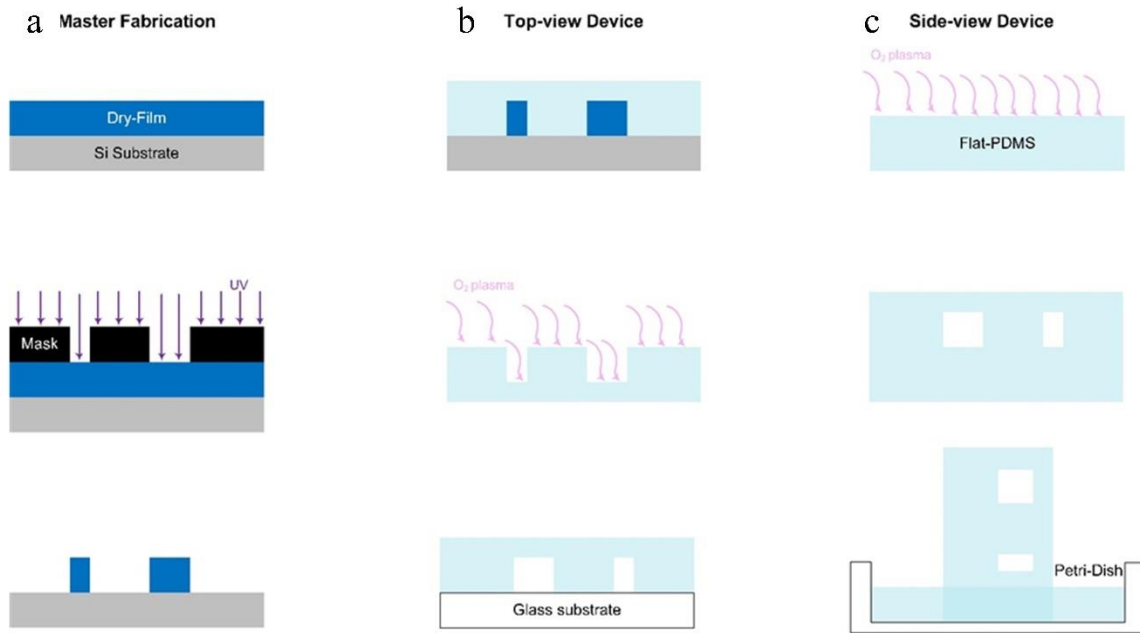


Figure. 16. Schematics of soft lithography. (a) master fabrication by align dry film on silicon substrate. (b) Top-view device fabrication by casing PDMS and oxygen plasma bonding on glass substrate. (c) Side-view device fabrication by bonding a flat PDMS and vertically cured inside of a Petri Dish.

ratio, was cast on the fabricated master mold and cured on a hot plate at 60°C for 4 h. PDMS replicas with the spiral structure were obtained. Then, the PDMS were bonded to standard microscope glass slides using oxygen plasma treatment. For side-view imaging, devices were mounted vertically and the edges of PDMS replicas were cut using a sharp blade orthogonal to the spiral pattern, then placed vertically on uncured PDMS in a Petri Dish and cured on a hot plate at 60 °C for 4 h to improve optical transparency and flatten the cutting edge.

4.2.6 Flow Experiment

Sperm, tail-off, and particle samples were separately loaded into a 10 mL syringe with luer lock interface and connected to microfluidic devices using 0.06" PTFE tubing. A programmable syringe pump (Legato 201, Kd Scientific, USA) was used to drive particles into devices with preset flow rates. The flow rate was varied from 10 $\mu\text{L}/\text{min}$ to 350 $\mu\text{L}/\text{min}$. The fluorescence imaging was accomplishing using an inverted microscope (IX83 Olympus, Inc., USA) with a 16-bit sCMOS camera (Zyla 5.5, Andor Technology Ltd, Belfast, UK). Fluorescent images of top view were taken at quarter-circle positions throughout channel length with exposure time of 150 μs for acquiring the flowing trajectories by using 20 \times objective with high numerical aperture (NA = 0.7). The CellSense software (Olympus, Inc.) was used to sequentially obtain 150 images at each position. Streamline width was defined as fluorescent intensity FWHM across channel width. Bright-field images of top view were captured with a high-speed camera (AX 200 Mini, Photron USA, Inc.) at frame rate of up to 10,000 fps depending on flow rate, with exposure time of 1 μs for obtaining particle distribution probability and height position along the channel height. Bright-field side view images of particles were taken using 20 \times objective with long (10 mm) working distance using procedure described above. ImageJ was used to measure the lateral and vertical position of sperm cells.

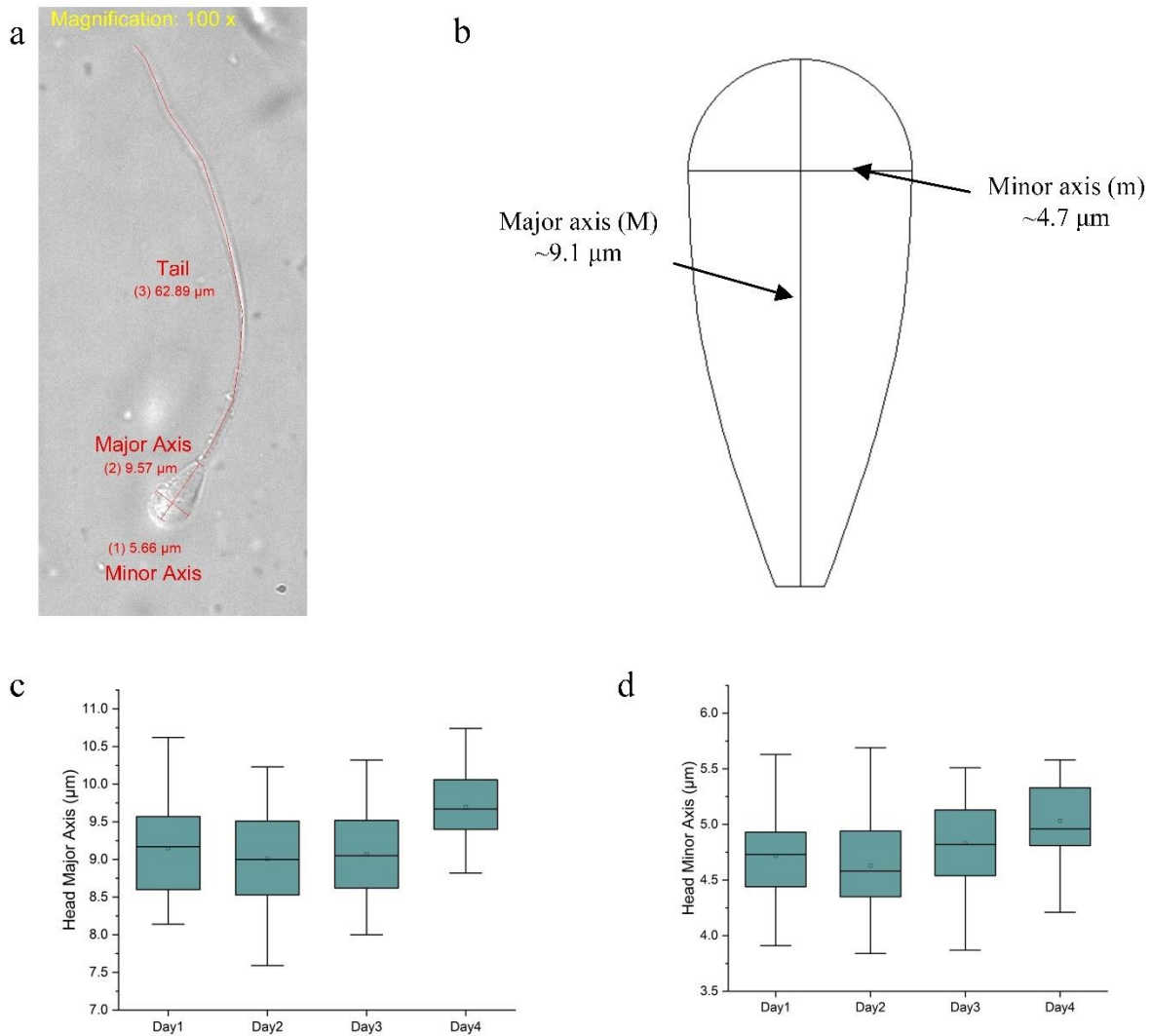


Figure.17 Bovine spermatozoa morphology. (a) Bright-field image of a bovine sperm cell in 100 \times magnification. The head major axis, minor axis, and tail length were measured by using CellSense software. (b) Schematic of the sperm head (c) Box plots of sperm head major and minor axis (d) size from Day 1 to Day 4 with N= 291

4.3 Results and Discussion

4.3.1 Sperm Cell Morphology

Inertial microfluidic techniques are highly dependent on particle size^{78,127} and shape^{54,128}. Thus, morphological measurement of spermatozoa is essential for microfluidic device design. A sperm cell consists of an asymmetrical paddle shape head and a long-thin motile tail¹²⁹ shown in **Fig.17a**. The major axis (a) of the sperm head is defined as the distance starting from the top of the head to the tail and the minor axis (b) is defined as the length of the chord connecting the arc ending points (**Fig.17b**).

Table II shows the statistical results of the morphology parameters of bovine sperm cells. The major axis was $9.08 \pm 0.56 \mu\text{m}$ and minor axis was $4.73 \pm 3.78 \mu\text{m}$. The length of tail was $62.44 \pm 3.04 \mu\text{m}$. Next, we preserved the raw sperm sample ($n=16$) in 4°C for four days and measured the major and minor axis every day. The box plots in **Fig.17c** and **d** shows that the sperm head enlarged after two days. The results suggest the experiments need to be done within two days for focusing sperm cells.

TABLE II
MORPHOLOGY PARAMETERS OF BOVINE SPERMATOZOA

Morphology Parameters	N total	Mean	Standard Deviation	Minimum	Median	Maximum
Head Major Axis (μm)	291	9.08	0.56	7.59	9.03	10.62
Head Minor Axis (μm)	291	4.73	0.38	3.84	4.73	5.69
Tail Length (μm)	291	62.44	3.04	45.18	62.96	67.71

4.3.2 Cell Viability

Fig.18 a/b demonstrated that the live and dead sperm cell after Calcein AM/ propidium iodide (PI) staining. Recent studies^{130–132} confirmed that the flow rate and the corresponding shear rate has influenced the cell viability in microfluidic devices. Increasing the shear rate in

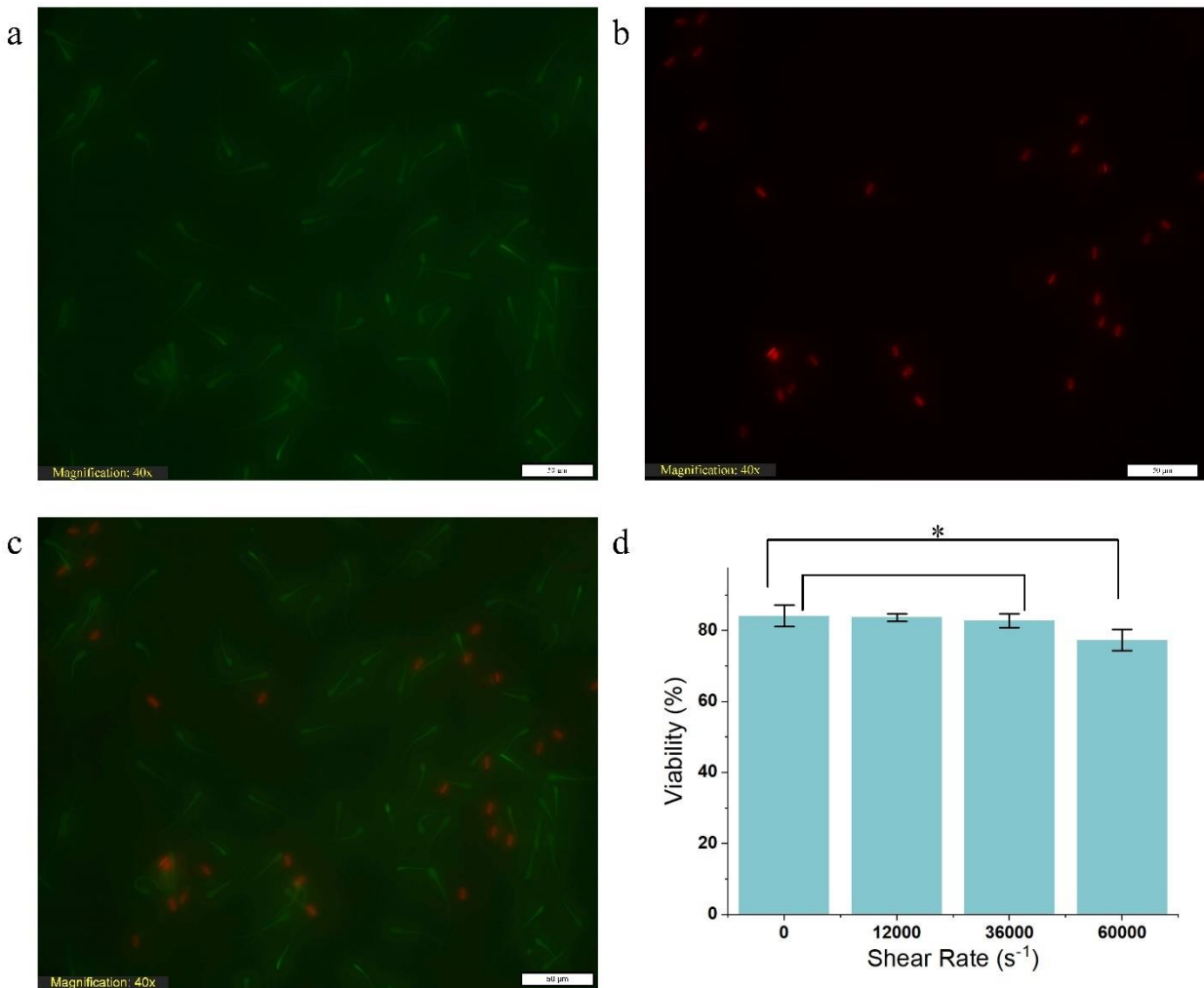


Figure.18 Live/Dead stain of sperm cells. (a) The live and (b) dead sperm cells were fluorescently labeled by Calcein AM and PI with green and red color respectively. (c) The composed image of live and dead. (d) Viability of the sperm cells at 60000 s^{-1} was not significantly lower than 0 s^{-1} ($n=3$). $*p < 0.05$.

flow caused increased shear stress surround cells and an increase in cell death. The shear rate equation was expressed as:

$$\gamma = \frac{2Q}{h\omega^2} \quad (13)$$

Comparing the cell viability in range of shear rate shown in **Fig.18d**, cell viability after flowing through the device with the shear rate of 60000 s^{-1} ($250 \text{ }\mu\text{L}/\text{min}$) not significantly decreased the sperm cell viability ($p \sim 0.05$). These viability results suggest that the spiral device focused sperm cells maintain the cell viability and morphology.

4.3.3 Sperm Cell Head and Tail Isolation

The cell migration mechanism can be explained by the hydraulic forces balance in spiral

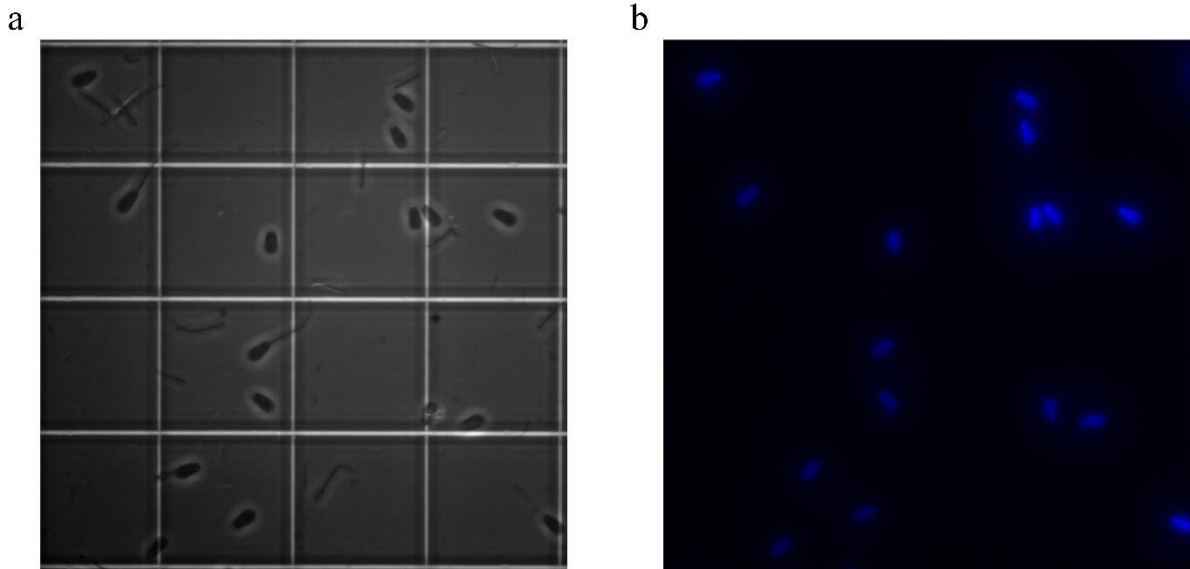


Figure.19 Tail-off sperm cell preparation from raw spermatozoa. (a) Bright field image of the tail-off cells after isolation from microtip sonicator. (b) The corresponded fluorescent stain image. The isolation efficiency is $94.4\% \pm 3.2\%$ by measuring 1684 cells ($n=10$).

channel. A sperm cell consists of a larger size and asymmetrical shape of head and a thin-long tail which are characterized in previous section. To investigate the effects of the head and tail on sperm migration in flow, we need to isolate sperm tails away from the head. The **Fig. 19a** illustrated that sperm tails were successfully chopped off. The tail-off sperm cells were fluorescent labeled by using Hoechst 33342 shown in **Fig.19b**. The isolation efficiency is 94.4% \pm 3.2% by measuring 1684 cells (n=10).

4.3.4 Effects of Shape and Tail on Sperm Cell Migration

Dean coupled inertial focusing behavior was proposed by Kuntaegowdanahalli⁷⁸ that the determining factor of particle equilibrium position is the ratio of F_L/F_D , where the larger particle equilibrates closer to the inner-wall of the channel than smaller particle. The curvature induced Dean vortices introduce an asymmetric velocity profile in spiral rectangular and result in asymmetric distribution of the hydraulic forces, which is expected to a focus cell along their largest diameter and shapes to minimize shear, leading to alternation of equilibrium positions. The balance of inertial and Dean forces that determines the particle and cell stream lateral position depends on the size and shape(citations). Most of the microfluidic devices reported in literature mimic the cell migration by using spherical particles. However, asymmetrical cells that do not experience similar force balance as spherical particle, also due to the asymmetrical shape that alters the equilibrium positions in flow.

To probe asymmetric shape effects and disassemble the size impacts on ellipse head motion, we selected fluorescent polystyrene spherical particles with diameter of 7.32 μm , 4.16 μm and 2.01 μm , the intact sperm cells, and tail-off cells were individually introduced through the inlet of the spiral device with channel dimensions 75 $\mu\text{m} \times$ 25 μm ($w \times h$). We recorded the fluorescent streak trace images of in wide range of flow rates from 10 to 250 $\mu\text{L}/\text{min}$ with

accorded Re from 3.3 to 83.3 in PBS at the outlet. For each of the stacked fluorescent image, the flow direction is from left to right. The top-view fluorescent images in **Fig.20a** illustrate sperm cells with asymmetrical shape performed a different focusing behaviors as increasing the flow rates at outlet. As increasing the flow rates, spherical particles with diameters of 7.32 μm and 4.16 μm , with blockage ratios of $\beta > 0.07$, focused into one streamline and the lateral positions closer to the inner wall of the channel, which is in conformance to our previous study⁷⁸. Smaller particles with diameter of 2.01, with a blockage ratio of $\beta < 0.07$, randomly distributed throughout the channel. This can be explained that particle with $\beta < 0.07$ was flowed with the curvature induced the secondary Dean flow through the cross-section. To demonstrate the effects of the tail on sperm cell migration, intact and tail-off sperm cells will introduce into devices at same experiments conditions. Interestingly, comparing the migration behaviors of spherical particle and tail-off sperm cells from top-view, we found that the tail-off cells exhibited similar focusing behaviors as 4.17 μm spherical particles, while the larger asymmetrical head with a larger major axis (a) $\sim 9.08 \mu\text{m}$ and a smaller minor axis (b) $\sim 4.73 \mu\text{m}$. Although these streak fluorescent images visualized the particle and cells migration trajectories and positions at range of flow rates, they are not enough for helping on quantitative analysis the subtle changes on focusing behaviors.

To illustrate the quantitative measurements sperm cells lateral migration evolution, we measured and plotted fluorescent intensity line scans across the channel width at selected Dean numbers in **Fig.20b**. We observed that two symmetrical peaks to the centerline of channel width appeared at $De \sim 0.77$, suggesting sperm cells migration away from the center and sidewalls. As increasing the De to 5.13, the intensity near the outer wall raised and formed one peaks, due to a stronger Dean effect. While the thin-long tail distinctly differences the equilibrium lateral

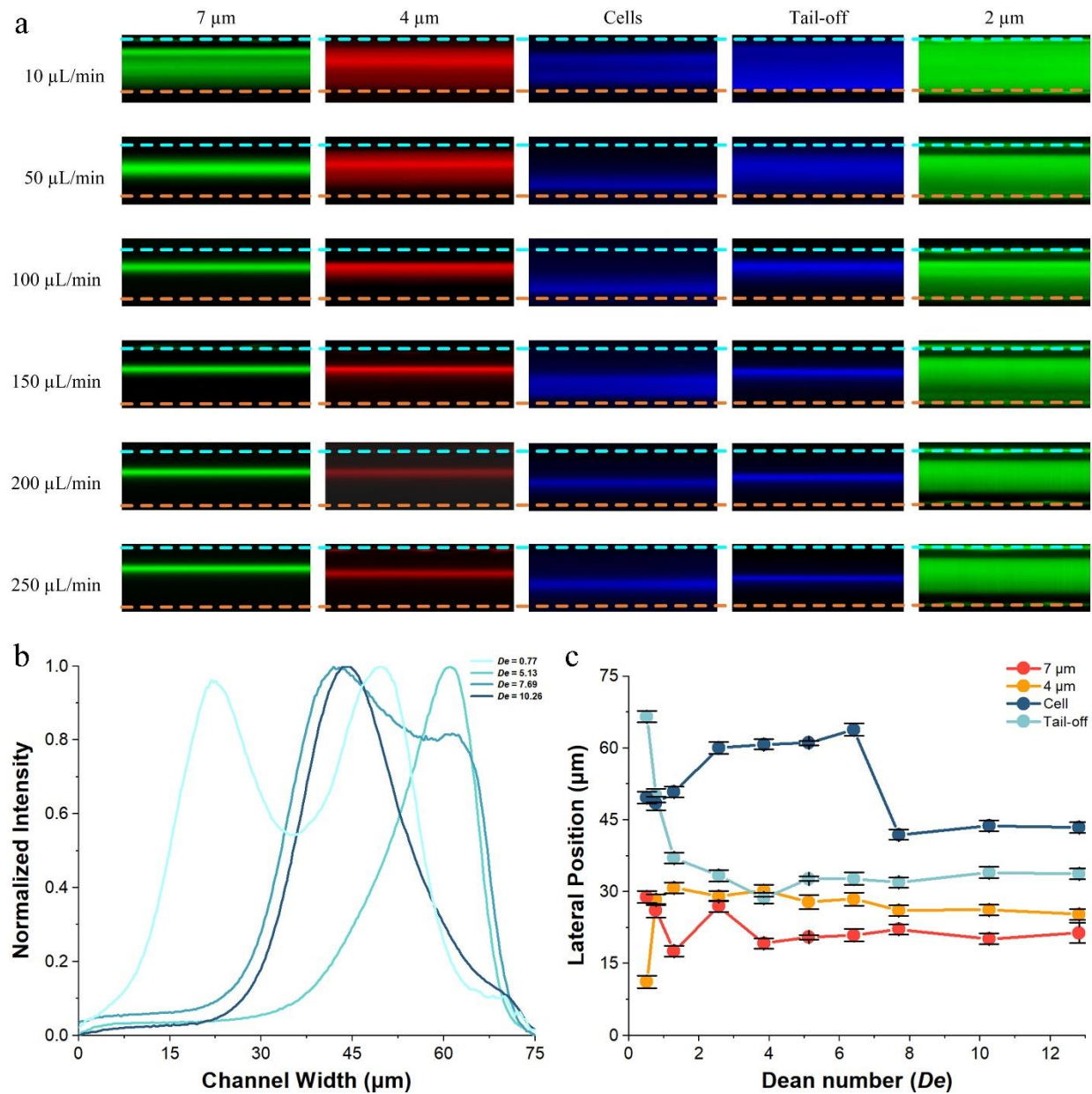


Figure.20. Top view focusing dynamics of spherical particles and asymmetrical sperm cells. (a) Stacked fluorescent streak images illustrate spherical particles, tail-off cells, and sperm cells focusing dynamics at outlet. Teal and orange dash lines indicates the inner wall and outer wall of the channel. Spherical particles with diameters of 7.32 μm , and 2.01 μm labeled as green and 4.16 μm as red. The asymmetrical intact sperm cells and tail-off cells were labeled as blue. The left column indicates the flow rates of the experiments. The light blue and orange dash lines represent the inner wall and outer wall of the channel. (b) Measured fluorescent intensity profiles of sperm cells across the channel width at selected De from 0.77 to 10.26, clearly illustrating the lateral migration evolution. (c) Particles, tail-off cell, and sperm cell lateral migration as function of Dean number.

position. This can be explained that the Dean drag force dominates on thin-long tail following with the secondary Dean flow yield a new force balance near the outer wall of the channel. Interestingly, at $De \sim 6.15$, the intensity near the outer wall decreased, suggesting diminution of sperm cells and their migration toward to the center of the channel. This can be partially explained that the increased F_D pushed sperm cells with the thin-long tail toward the bottom and top walls from the centerline of the channel height, where the Dean vortices toward the center of the channel width. This is validated by further increasing $De > 10.26$, the intensity near the center of channel width grew, indicating the sperm cells migration toward to the center of the channel. Interestingly, the sperm cells performed a dual migration direction which is dependent on the De . This strongly suggests that the thin-long tail enhances the Dean effects on intact sperm cell lateral migration results sperm cell follow the Dean vortices across the channel.

In addition, **Fig.20c** shows the lateral positions of spherical particles, tail-off cells, and sperm cells as a function of Dean number at the device outlet. Due to the dispersal distribution, 2 μm spherical particle is not included. We observed that 4 μm and tail-off cells exhibited a similar trajectories as increasing flow rates, while 4 μm lateral positions closer to the inner wall. In contrast to straight channel, Hur *et al* claimed that the asymmetry in shapes would not significantly contribute to the variation in equilibrium lateral position¹³³. However, in spiral channel, we found the asymmetrical shape of the sperm head with a larger major axis alters the lateral position. In our previous study, the spherical particles migrate toward the inner wall of the channel due to curvature induced Dean drag force and the equilibrium position depends on the ratio of F_L/F_D . In curved microfluidics channels, the secondary flows appear within the cross-section and induce a drag force, F_D , which scaling with the particle size and viscous drag coefficient¹³⁴. On the one hand, drag force increases in proportion to the cross-sectional area of

the body and in proportion to ρU^2 . On the other hand, surface friction increases in proportion to the surface area of the body and in proportion to μU^{135} . Therefore, the F_D differs in drag coefficient which is expected to sperm cell. Thus, this can be explained that the asymmetrical tail-off sperm cells experienced a stronger F_D force, leading to the lateral position shift away from the inner wall towards the center of the channel. On the other hand, the asymmetrical tail-off cells experienced higher secondary Dean drag force as they have a larger major axis when their orientation is vertical to the Dean vortices.

4.3.5 Shape and Tail Effects on Vertical Migration

Similarly, the hydraulic forces along the channel height can also influence particle and sperm cell focusing behaviors along the channel height. Toner¹¹⁷ and others¹¹⁸ suggested that two focusing positions are present along the channel height at the outlet. Asymmetrical cell migration along the channel height remains unclear due to lack of direct observation. Additionally, the side-view imaging can aid on understanding the shape influences on sperm cells migration. Thus, we vertically mounted a spiral microchannel to visualize particles and sperm cells migration along the channel height at outlet. This approach was described on previous chapter. We next investigated migration of particles and cells along the channel height near the outlet. **Fig.21** presents the stack fluorescent images at the outlet of particles, sperm cells, and the tail-off cells at the flow rates range from 10 $\mu\text{L}/\text{min}$ to 250 $\mu\text{L}/\text{min}$ at outlet from side-view. The staked fluorescent images confirm that 7.32 μm and 4.16 μm spherical particles, tail-off cells, and sperm cells present two streams appearing along the channel height, suggesting two positions in the cross-section. This inertial focusing behavior of larger particles from side-view remain two stable positions over the range of flow rates, which is consistent with previous studies^{117,118}. For smaller 2 μm particles, with a blockage ratio of $\beta < 0.07$, particles remained in random

distribution across the channel height. Tail-off sperm cells with major axis $\sim 9.08 \mu\text{m}$ consistently exhibited similar focusing behaviors as $4.17 \mu\text{m}$ spherical particles from top-view and side-view. Interestingly, at lower flow rates, $10 \mu\text{L}/\text{min}$ and $50 \mu\text{L}/\text{min}$, intact sperm cells with tail concentrated near the center of the channel. At flow rate $> 100 \mu\text{L}/\text{min}$, the two distinct streams appeared near the centerline and we measured the vertical positions of the two streams along the channel height. The data in **Fig.21b**. illustrate that the sperm cells focused into a single stream near the centerline with $De < 6.15$ from side-view. For the observation of top-view, one single stream focused near the outer wall of the channel, suggesting a single stream at the cross-section of the channel at range of $2.56 < De < 6.15$. Note that the Dean drag is toward the outer wall near the vertical centerline, which leads to the sperm cells lateral migration toward the outer wall of the channel. On the other hand, as $De > 6.15$, the single stream of sperm cells split into two near the centerline of the channel height, where the sperm cells gradually moved toward the horizontal centerline from top-view (**Fig.20**). These two streams near the bottom and top walls where Dean drag is toward the center, which leads to the sperm cells migrate toward the horizontal center of the channel. Additionally, the gap distance of sperm cells is greater than spherical particles and tail-off cells at higher De shown in **Fig.21c**. This suggests that sperm cells experienced a stronger F_L which push them away from the centerline of the channel. Due to the $F_L \propto a_p^4$ with direction away from the centerline, the orientation of the cells may strongly impact on the hydraulic force and yield the differences vertical positions. On the other hand, the asymmetrical sperm cells may experience a higher secondary F_D force with the longer tail when their orientation is vertical to the Dean vortices. We next investigated the asymmetrical cell orientation dynamics in spiral channel.

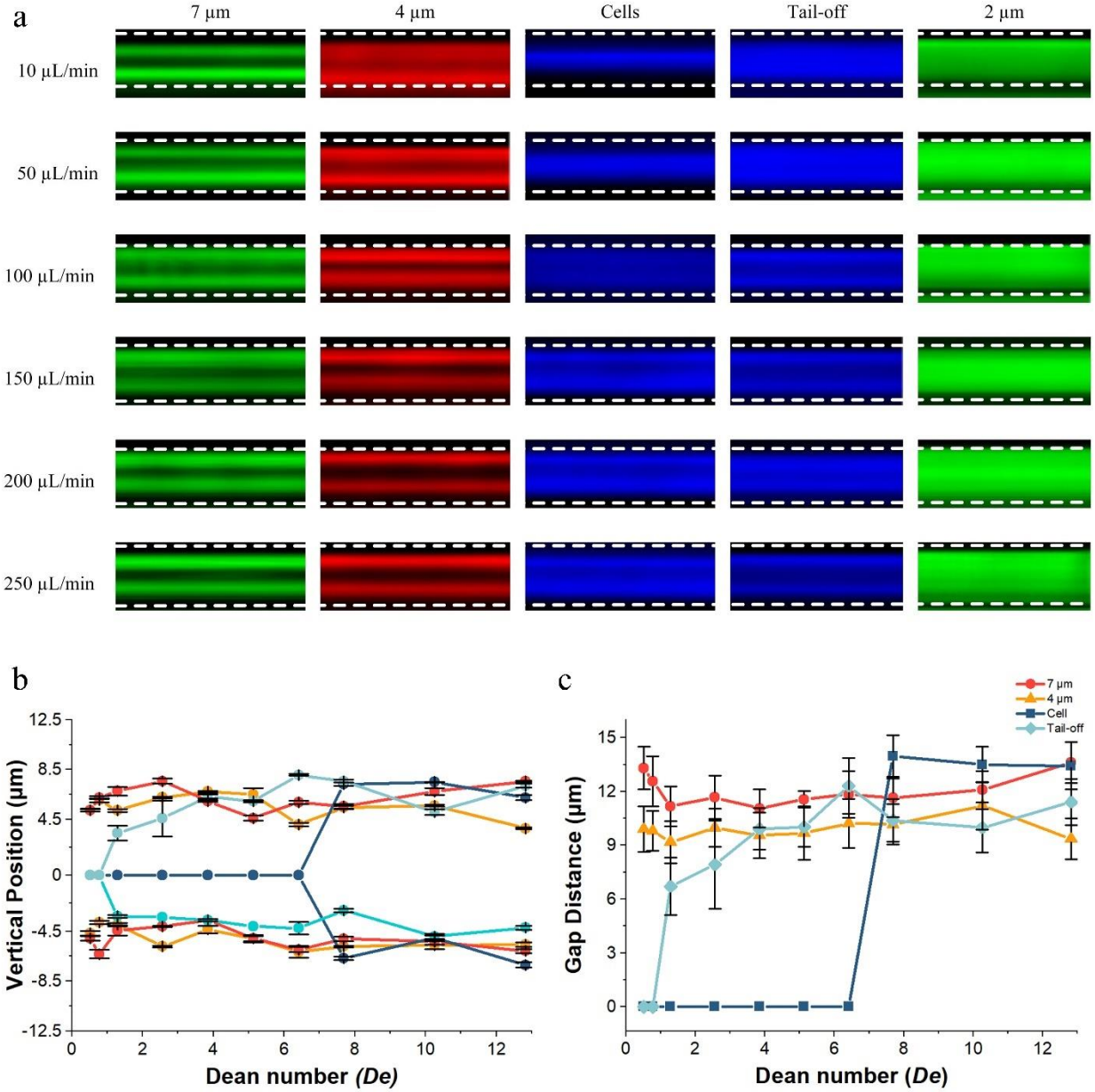


Figure.21 Side-view focusing evolution of spherical particles and asymmetrical sperm cells. (a) Stacked fluorescent streak images illustrate spherical particles, tail-off cells, and sperm cells focusing dynamics at outlet. White dash lines labeled the channel top and bottom walls. (b) Vertical position as function of Dean number. The ± 12.5 indicates the normalized vertical position of the $25\ \mu\text{m}$ channel height. (c) Gap distance of particles, tail-off cells, and sperm cells as a function of Dean number. The red, orange, teal, and dark blue represents the $7\ \mu\text{m}$, $4\ \mu\text{m}$, tail-off cell, and sperm cells respectively. Each point of the plots collected from a triple measurement at outlet. Due to channel deformation, empirical $\pm 2\ \mu\text{m}$ systematical error bars added in (d).

4.3.6 Cell orientation and alignment

The spherical particle presents the same area and size to the oncoming fluid independent as its orientation. However, due to the asymmetrical shape, sperm cells display varying area and size depending on its orientation which impact on the magnitude of hydraulic forces and alternate the focusing positions. Asymmetrical cells and ellipsoid particles usually exhibit differences motions and orientations in shear flows depending on the applied Re in straight channel^{49,136,137}. While sperm cells with long tail in curvature included secondary flow spiral channel has rarely been studied.

To investigate the orientation of sperm cells in flow, we measured sperm cell orientation index (OI) which is defined as the ratio of the major axis (M) to minor axis (m). We measured and calculated the OI of the sperm cells and classified as Flat-on ($1.5 < M/m < 2.6$), Edge-on ($4.3 < M/m < 7$), and Misaligned ($2.7 < M/m < 4.2$). The OI obtained from a typical bright field image, which is corresponded to the line scan in fluorescent images from top-view, is shown in **Fig.22a** at $De \sim 5.13$. The three sperm cell orientations are illustrated in this figure. The Flat-on orientation indicates that the sperm cell head is aligned with x-y plane. The Edge-on orientation suggests that the major axis (a) is parallel to the x-y plane and the sperm cell head is rotated with the major axis. The Misaligned orientation indicates that the sperm cell head is not aligned with x-y plane and rotated with major and minor axis.

Fig.22b shows the orientation of sperm cells distribution in spiral channel at range of De from 2.05 to 12.31. In flow with lower $De < 4.11$, only 49% of sperm cells exhibited Flat-on orientation and aligned with x-y plane. As the De increased to 6.15, 91% of the sperm cells were aligned with x-y plane with Flat-on orientation. Only 4% of the sperm cells are Misaligned. This suggests that the sperm cell alignment was readily achieved. Note that the sperm cells were

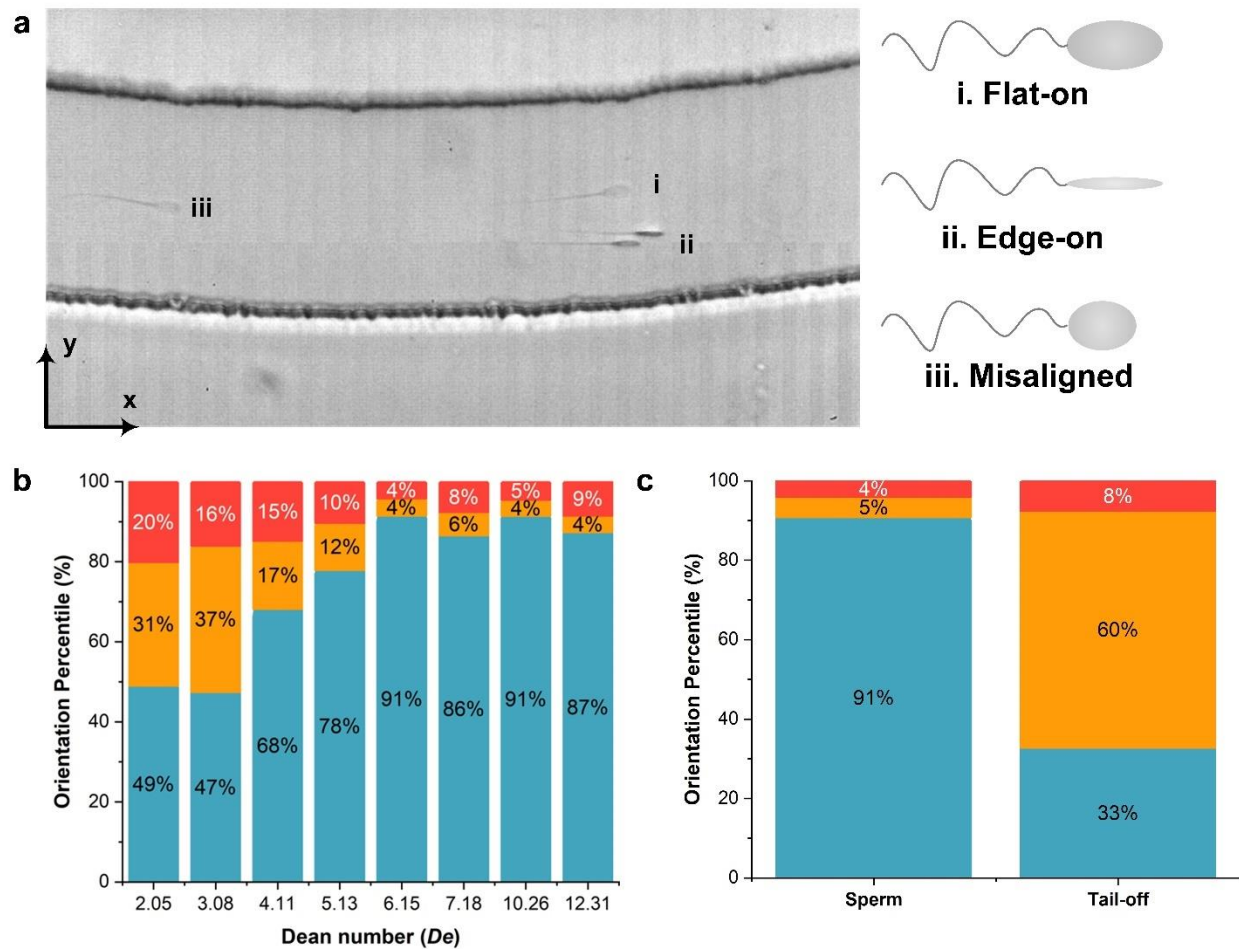


Figure.22 Cells orientation distribution in spiral channel.(a) High-speed camera bright field image of sperm cell at $De \sim 5.13$ illustrate sperm cell orientation and schematic of the flat-on, edge-on, and misaligned orientations of sperm cells.(b) The sperm cell orientation distribution at range of Dean number.(c) Sperm cell and tal-off cell orientation distribution at $De \sim 10.26$. Flat-on, Edge-on, and Misaligned orientations are labeled as blue, orange, and red respectively. The total measured number of sperm cells is $N = 3362$.

focused into two streams from one stream along the channel height at high De from side-view in **Fig.21**. This suggests that the Dean effects take place on sperm cell vertical migration where the F_D drag the sperm cells toward the bottom and top walls that cause sperm cell aligned with the x-y plane without any dimensional rotation. From top-view, the lateral position of sperm cells was gradually migrated toward the center of the channel. Our results agree with the previous study that aligned ellipsoid shape of particles without freely rotation followed in Jeffery orbits in which the ellipsoid particles are periodically pushed toward the center of the channel⁴⁹. In addition, as the sperm cells aligned with x-y plane, lateral position was gradually migrated from outer wall to centerline of the channel width as $De > 6.15$ in **Fig.22b**. Prohm *et al.* performed simulation studies that when prevent the particle from rotating, particle experiences a lift force always shifts the lateral equilibrium position toward the center of the channel. These results further indicate the aligned sperm cell near the bottom and top walls experiences F_D and F_L with same direction which toward the center of the channel as being responsible for sperm cell lateral migration.

Ellipsoid particles exhibit tumbling movement in inertial flow, leading to an alternate focusing position due to the different rotational motion^{137,138}. However, sperm cells may exhibit a different rotation motion due to the long tail. To insight the tail effects on sperm cells orientation, **Fig.22c** demonstrated the orientation distribution of sperm cells and tail-off cells at $De \sim 10.26$. 91% of sperm cells were Flat-on orientation, suggesting majority of the sperm cells aligned with x-y plane. However, the Flat-on orientation of tail-off cell dramatically reduced to 33% but 60% of the tail-off cells were Edge-on. Only 4% increased of Misaligned orientation without tails. This agrees with Li *et al.* claimed that higher aspect ratio, ellipsoid shaped, cells are easier to align with flow direction with a tumbling motion in straight channel¹³⁶. These results suggests that the long tail strongly reduced the sperm cell rotation along the major axis.

4.3.7 General Focusing Mechanism

Fig.23 illustrates sperm cells focusing in spiral microchannel with the diagrams indicating the key forces involved in sperm cell equilibration. Due to the curvature induced the secondary Dean flow, sperm cells experience two counter-rotating Dean vortices in the top and bottom halves of the channel. Note that the vortices toward the inner wall of the channel near the top and bottom walls, whereas the direction changed to outer wall near the center of the channel. Three top-view orientations schematics of sperm cells are presented to indicate the sperm cell orientation in flow. Near the side-walls, the secondary flow generates a vertical force in both vortices. Due to the long tail $\sim 60 \mu\text{m}$, the sperm cells experience higher secondary Dean effects and thus the sperm cells across both arms of the vortex with two opposing Dean drag forces must be considered to impact on migration behaviors.

Sperm cells focusing in spiral channel presents dual direction of lateral migration in depending on the Dean number **Fig.20**. We defined the critical Dean number (De_c) as the sperm cell lateral migration direction changed from outward to inward. For example, in $75 \mu\text{m} \times 25 \mu\text{m}$ spiral channel, sperm cells lateral position migrated toward outer wall at $De < 6.15$ and when the $De > 6.15$ the sperm cells migrated towards the center of the channel. Thus, the critical Dean number (De_c) is 6.15. Meanwhile, as the $De > 6.15$, 91% of sperm cells were Flat-on orientation, suggesting sperm cells focusing with free rotation as $De > De_c$ in **Fig.22**. Therefore, we propose that the sperm focusing manifests in three regimes in spiral channel depending on the De_c . At $De < De_c$, the sperm cells focused into two streams closer to the outer wall of the channel and one bulk stream near the centerline of the channel height. Three orientations likely even distributed near in flow. The sperm cell is subjected to the F_D and F_L with same direction, which leads to a net force acting on particle toward the outer wall of the channel. As a result, these positions are

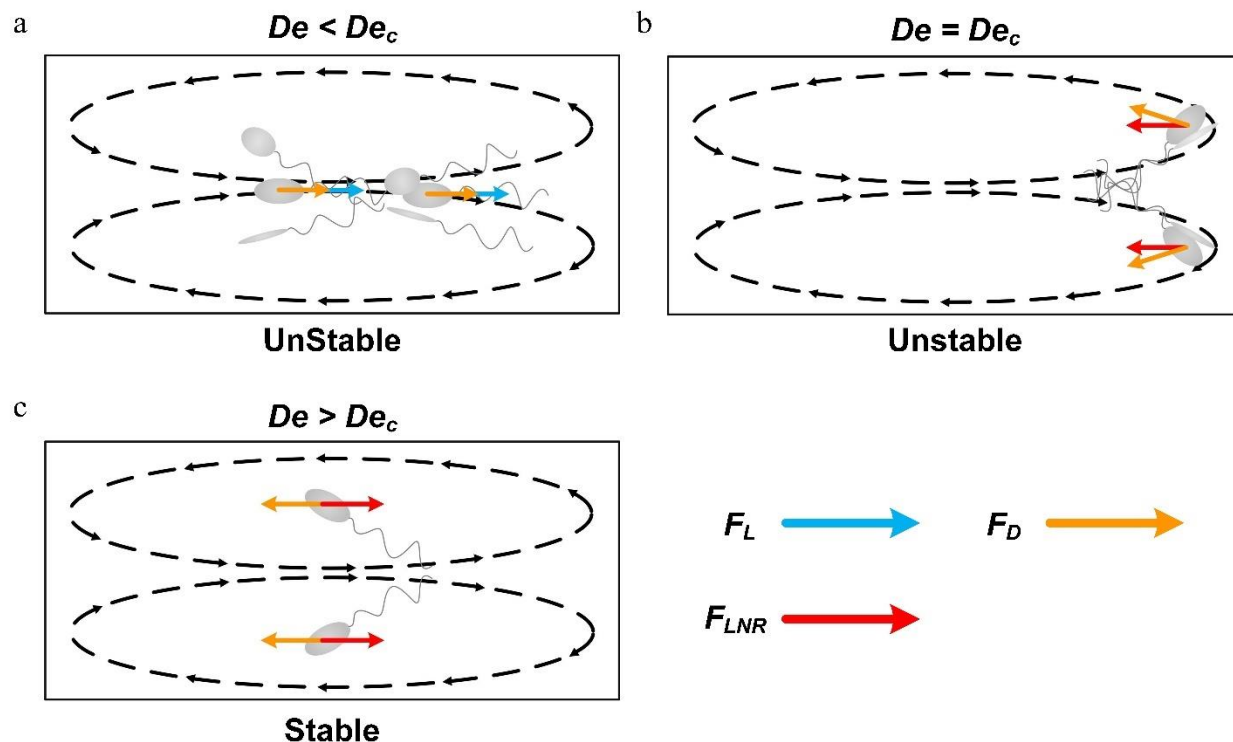


Figure.23. General force mechanics on sperm cell migration depending on the critical Dean number. Schematics images illustrate the sperm cells focusing positions and the corresponded force balance in low aspect ratio spiral channel with dimension of $75 \mu\text{m} \times 25 \mu\text{m}$ at (a) $De < De_c$, (b) $De = De_c$, and (c) $De > De_c$. Blue, orange, and red arrows indicate the inertial lift force F_L , Dean drag force F_D , and lift force with no rotation F_{LNR} , respectively. The schematics of sperm cell orientations are same as in Fig.21.

unstable because the force balance is not zero, illustrated in **Fig.23a**. The sperm cell migrates toward the outer wall of the channel, due to the long tail enhanced the Dean effects in lateral position. As increasing the $De = De_c$, the long and thin tail means that the sperm cells span both the top and bottom Dean vortices. Note near the outer wall of the channel, the Dean vortices with vertical directions toward the top and bottom walls, yielding one stream split to two streams near the top and bottom walls from side-view. Meanwhile, 91% of sperm cells were Flat-on orientation, suggesting that the sperm cell aligned without freely rotation, which alters the lift

force with no rotation, F_{LNR} , toward the center of the channel¹³⁹. Similarly, for the sperm cell near the outer wall of the channel, F_D and F_{LNR} with same direction causes unstable positions and the sperm cells to start its inward migration (**Fig.23b**). This vertical movement and sperm cell alignment is responsible for the inward migration. While the $De > De_c$, as the sperm cells span in the top and bottom walls, the lateral position change from outer half to center of the channel, leading to a force balance shown in **Fig.23c**. Near the center of the channel width, due to the sperm cell alignment, the F_D and F_{LNR} have opposite directions near the top and bottom walls. As a result, the balance of F_D and F_{LNR} is responsible for the inward and outward migration of sperm cell and the stronger Dean effects due to the long tail drags the sperm cells to the outer wall of the channel, resulting outward migration. The sperm cell alignment modifies the F_{LNR} direction, resulting in two final equilibrium position.

4.3.8 Critical Dean Number

We observed the migration direction of sperm cells in spiral channels changes from outward to inward over a certain threshold of the Dean number (De), which we defined as the critical Dean number (De_c). For $De < De_c$, the sperm cell migrates toward the outer half of the channel, whereas tail-off cells focused in the inner half of the channel, suggesting the long tail attached sperm cells in Dean vortices followed the curvature induced Dean vortices. Due to the same direction of F_L and F_D , the imbalanced hydraulic force pushed sperm cell outward. For $De = De_c$, the aligned sperm cell with no rotation modified the F_L to F_{LNR} which toward the center of the channel and the Dean vortices with vertical direction split sperm cells to top and bottom of the channel. The net force toward the center of the channel and swifts the migration direction from outward to inward.

Fig.24 shows the sperm cell lateral positions at range of De in spiral channel with

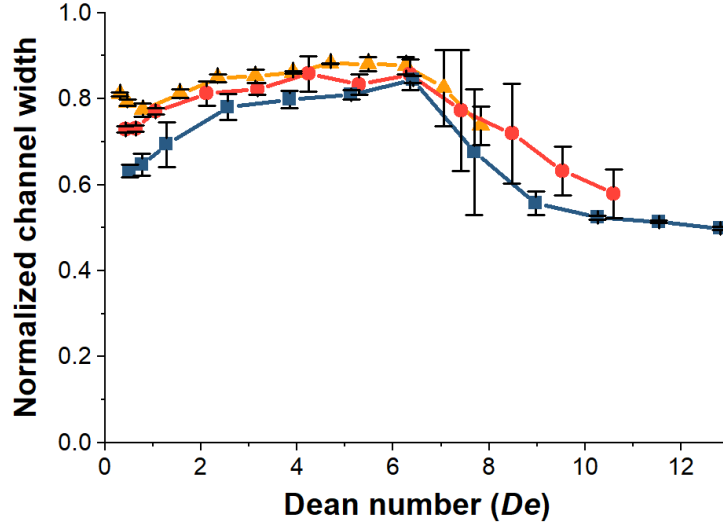


Figure.24 Plot of the normalized lateral positions of sperm cell streams in spiral channels. The orange, red, and blue color represent the spiral channel with dimensions of $150 \mu m \times 25 \mu m$, $100 \mu m \times 25 \mu m$, and $75 \mu m \times 25 \mu m$, respectively.

dimensions of 75×25 ($AR=0.33$), 100×25 ($AR=0.25$), and 150×25 ($AR=0.17$). We observed that sperm cell initially migrated in outward at low Dean number and the migration direction transitionally changed to inward as increasing Dean number. We also observed the $De_c \sim 6.5$ for sperm cell is independent of the channel AR . As a result, the De_c determines the sperm cell migration direction and alignment in spiral channel which is highly dependent on the asymmetrical shape and long tail.

4.4 Summary

In this work, we experimentally demonstrated migration of sperm cells in spiral microchannel in top and side view. We found that the sperm cell migration direction and

alignment depend on the critical Dean number (De_c) in spiral low AR rectangular channel. Analyses of the sperm cell, tail-off cell and spherical particle lateral and vertical migration demonstrated that the asymmetrical shape and long tail play an important role in sperm cell migration. Our results illustrate the underlying hydraulic forces balance of sperm cell migration in cross-section. Ultimately, we anticipate that these results will offer a useful guide for inertial microfluidics device design for improving efficiency of sperm focusing, sorting, and cytometry applications.

CHAPTER 5

CONCLUSIONS AND FUTURE WORK

5.1. Summary

In this work, particles migration dynamics were tested in spiral channels with initial radii of curvature at range of 1 mm to 6 mm, Elastic number (El) at a broader range from 0 to 117, and particle diameters at range of 7 μm to 25 μm with blockage ratio from 0.088 to 0.3. The results suggests that the particle equilibrium position strongly depended on device curvature and that Dean effects played an important role on particle migration, where increasing De leads to reduction of multiple streamlines to one and improvement in focusing quality. The elasticity of fluids significant alternate particle focusing behaviors, dividing into three regimes. When $El < 1$, in this inertial regime, particles progressively form two streams along the channel downstream due to the inertial effects. When $1 < El < 50$, particles initially focused into three streams transition to one stream. In this elasto-inertial fluid regime, the elastic force F_E balances inertial lift F_L and Dean drag F_D , resulting in equilibrium position at the channel centerline. When $El > 50$, particles rapidly migrate into a single stream (at 0.7 cm downstream) and gradually move toward the outer wall along the downstream length. In this viscoelastic fluid regime, the elastic force F_E completely dominates in the vertical direction as inertial force is negligible ($Re = 0.36$ and $El = 117$ for 5000 ppm PEO). Particles with different sizes experience differing degrees of drag, leading to different disappearance sequences of the side streams observed in the transition stage between the low and high flow rate cases.

After exploring the broad range of device design, fluids, and particle parameters, this work provides the first experimental and simulation proof of particle 3-T-1 focusing evolution along the channel downstream length. The numerical results demonstrated that vortices are modified due to the fluid elasticity (due to N2), leading to lateral asymmetry of velocity magnitude in secondary flow. The secondary flow is stronger near the inner wall. The balance of the elastic force and inertial force is responsible for the formation of the three streams (six positions) and the net drag force due to the secondary flow brings the side stream to the center, resulting in two final equilibrium positions. Consequently, the lateral position of the final focused streams is not permanent, depending on the evolution of the secondary flow as evidenced in the fluorescent images near the end of the channel.

Due to the asymmetrical shape, the emission intensity from the narrow edge approximately twice that of the flat face¹²⁰, which significantly impacts on results of the fluorescent labeled sperm cells from current cytometry flow aided IVF. Therefore, effective cell sorting and consistent cell orientation is critical. Therefore, precise manipulation of sperm cell position, focusing, and alignment is the essential processes of IVF and improve fertilization and ongoing pregnancy rates¹⁴⁰. Additionally, due to the limited source of asymmetrical and cell-like shape particles, it is difficult to explore the shape effects and not ideally to mimic cells migration by using the spherical particles. Therefore, spermatozoa cells were used to investigate the mechanism of asymmetrical shape effects on lateral migration.

The shape and tail effects on migration were proved by comparing the spherical particles (diameter of 7 μm , 4 μm , and 2 μm) lateral and vertical migration. This work found that 4 μm and tail-off cells exhibited a similar trajectories as increasing flow rates, while 4 μm lateral positions closer to the inner wall. In our previous study, the spherical particles migrate toward

the inner wall of the channel due to curvature induced Dean drag force and the equilibrium position depends on the ratio of F_L/F_D . The asymmetrical tail-off sperm cells experienced a stronger F_D force, leading to the lateral position shift away from the inner wall towards the center of the channel. On the other hand, the asymmetrical tail-off cells experienced higher secondary Dean drag force as they have a larger major axis when their orientation is vertical to the Dean vortices.

The sperm cell orientation distributions were measured within the spiral channel as a variation of De . In flow with lower $De < 4.11$, only 49% of sperm cells exhibited Flat-on orientation and aligned with x-y plane. As the De increased to 6.15, 91% of the sperm cells were aligned with x-y plane with Flat-on orientation. Only 4% of the sperm cells are Misaligned. The results found that the sperm cell was aligned by the Dean effects that cause sperm cell aligned with the x-y plane without any dimensional rotation, indication the aligned sperm cell near the bottom and top walls experiences F_D and F_L with same direction which toward the center of the channel as being responsible for sperm cell lateral migration. Comparing the orientation distribution of sperm cell and tail-off cell that the long thin tail strongly reduced the sperm cell rotation along the major axis. As a result, the balance of F_D and F_{LNR} is responsible for the inward and outward migration of sperm cell and the stronger Dean effects due to the long tail drags the sperm cells to the outer wall of the channel, resulting outward migration. The sperm cell alignment modifies the F_{LNR} direction, resulting in two final equilibrium position. We also observed the critical De_c determines the sperm cell migration direction and alignment in spiral channel which is highly dependent on the asymmetrical shape and long tail.

Overall, this work presented a model of particle lateral migration in viscoelastic fluids, which should allow an improved understanding of the underlying mechanisms of Dean-coupled

viscoelastic focusing. The investigation of cell shape and tail effects should offer a new tool which can be used in precise separation applications for sperm cells. Ultimately, this work should yield guidelines for improved design of microfluidic devices for handling asymmetric cells, and perhaps to a broader acceptance of the viscoelastic microfluidics devices.

5.2. Future Work

Previous work⁴⁷ investigated the evolve of the curvature included secondary vortices across the low aspect ratio spiral devices. However, the Dean vortices dynamics in high aspect ratio (HAR) spiral devices have not been studied yet. Study of the phenomenon of the evolution of the secondary flows in high aspect ratio spiral channels will improve the understanding of the Dean effects on particle and cell sorting and potentially assist in manipulation of the Dean vortices and the interaction of the hydraulic forces to achieve a 3D focusing. To determine the secondary Dean vortices dynamics in high aspect ratio spiral channel, a three-inlet system will be fabricated to provide $1/3^{\text{rd}}$ of dye at input to visualize the vortices development. We need to use confocal microscopy to acquire the cross-section images at multiple positions through the channel downstream length. This enable to observe the development trend of secondary Dean vortices, which expect to perform different from the low aspect ratio channels in our previous work⁴⁷. By measuring the fluorescent trajectories along the channel downstream length, the Dean vortices velocity profile will be obtained. The results will provide critical information about the Dean vortices evolution which helps on understanding of the focusing mechanism in spiral channels and provide an better concept of particle/cell focusing in spiral channel.

Design and optimization of spiral microfluidic chip based on the knowledge gained from this work will enable to separate red blood cells from spermatozoa. RBCs often contaminate

seminal fluid during the testicular sperm extraction (TESE) procedures, which enriches the number of non-motile cells and adversely impacts the results of fertility screening. The conventional sperm separation approaches take advantage of the motility of sperm cells. Feng *et al* developed a spiral microfluidic device to separate RBCs from sperm TESE sample. However, the viability of sperm cells is uncertain under the influence of the shear stress in fluids. Only in this work, the sperm cell viability before and after flowing in device were tested using Calcein AM. The results showed that the shear rate viability has little effect on sperm cell's viability. The influence of cell viability under high flow rates and shear rates are still unclear, which deserves more attention from academic society.

REFERENCES

1. Di Carlo, D. Inertial microfluidics. *Lab Chip* **9**, 3038–3046 (2009).
2. Alix-Panabières, C. & Pantel, K. Challenges in circulating tumour cell research. *Nat. Rev. Cancer* **14**, 623–631 (2014).
3. Watanabe, M. *et al.* Isolation and molecular analysis of circulating tumor cells from lung cancer patients using a microfluidic chip type cell sorter. *Cancer Sci.* **109**, 2539–2548 (2018).
4. Gossett, D. R. *et al.* Label-free cell separation and sorting in microfluidic systems. *Anal. Bioanal. Chem.* **397**, 3249–3267 (2010).
5. Karabacak, N. M. *et al.* Microfluidic, marker-free isolation of circulating tumor cells from blood samples. doi:10.1038/nprot.2014.044
6. Bhagat, A. A. S., Kuntaegowdanahalli, S. S. & Papautsky, I. Inertial microfluidics for continuous particle filtration and extraction. *Microfluid. Nanofluidics* **7**, 217–226 (2009).
7. Bhagat, A. A. S., Kuntaegowdanahalli, S. S. & Papautsky, I. Continuous particle separation in spiral microchannels using dean flows and differential migration. *Lab Chip* **8**, 1906–1914 (2008).
8. Bhagat, A. A. S. *et al.* Microfluidics for cell separation. *Med. Biol. Eng. Comput.* **48**, 999–1014 (2010).
9. Toner, M. & Irimia, D. Blood-on-a-Chip. <http://dx.doi.org/10.1146/annurev.bioeng.7.011205.135108> **7**, 77–103 (2005).
10. Zhou, J., Mukherjee, P., Gao, H., Luan, Q. & Papautsky, I. Label-free microfluidic sorting of microparticles. *APL Bioeng.* **3**, 041504 (2019).
11. Whitesides, G. M. The origins and the future of microfluidics. *Nat.* **442**, 368–373 (2006).
12. Stone, H. A. & Kim, S. Microfluidics: Basic issues, applications, and challenges. *AIChE J.* **47**, 1250–1254 (2001).
13. Hejazian, M., Li, W. & Nguyen, N. T. Lab on a chip for continuous-flow magnetic cell separation. *Lab Chip* **15**, 959–970 (2015).

14. Xia, N. *et al.* Combined microfluidic-micromagnetic separation of living cells in continuous flow. *Biomed. Microdevices* 2006 84 **8**, 299–308 (2006).
15. Wu, D., Qin, J. & Lin, B. Electrophoretic separations on microfluidic chips. *J. Chromatogr. a* **1184**, 542 (2008).
16. Yu, L. *et al.* Microfluidic chip-based cell electrophoresis with multipoint laser-induced fluorescence detection system. *Electrophoresis* **28**, 4741–4747 (2007).
17. Aghaamoo, M., Aghilinejad, A., Chen, X. & Xu, J. On the design of deterministic dielectrophoresis for continuous separation of circulating tumor cells from peripheral blood cells. *Electrophoresis* **40**, 1486–1493 (2019).
18. Hu, X. *et al.* Marker-specific sorting of rare cells using dielectrophoresis. *Proc. Natl. Acad. Sci. U. S. A.* **102**, 15757–15761 (2005).
19. Gao, Y., Wu, M., Lin, Y. & Xu, J. Acoustic Microfluidic Separation Techniques and Bioapplications: A Review. *Micromachines* 2020, Vol. 11, Page 921 **11**, 921 (2020).
20. Antfolk, M. & Laurell, T. Continuous flow microfluidic separation and processing of rare cells and bioparticles found in blood – A review. *Anal. Chim. Acta* **965**, 9–35 (2017).
21. MacDonald, M. P., Spalding, G. C. & Dholakia, K. Microfluidic sorting in an optical lattice. *Nat.* 2003 4266965 **426**, 421–424 (2003).
22. Ricárdez-Vargas, I., Rodríguez-Montero, P., Ramos-García, R. & Volke-Sepúlveda, K. Modulated optical sieve for sorting of polydisperse microparticles. *Appl. Phys. Lett.* **88**, 121116 (2006).
23. Yamada, M., Nakashima, M. & Seki, M. Pinched flow fractionation: continuous size separation of particles utilizing a laminar flow profile in a pinched microchannel. *Anal. Chem.* **76**, 5465–71 (2004).
24. Cox, E. C., Sturm, J. C., Huang, L. R. & Austin, R. H. Continuous Particle Separation Through Deterministic Lateral Displacement. *Science* (80-.). **304**, 987–990 (2004).
25. Zhou, J. *et al.* Isolation of circulating tumor cells in non-small-cell-lung-cancer patients using a multi-flow microfluidic channel. *Microsystems Nanoeng.* **5**, (2019).
26. Wang, X. & Papautsky, I. Size-based microfluidic multimodal microparticle sorter. *Lab Chip* **15**, 1350–1359 (2015).
27. Nagrath, S. *et al.* Isolation of rare circulating tumour cells in cancer patients by microchip technology. *Nature* **450**, 1235–1239 (2007).
28. Zhou, J. & Papautsky, I. Fundamentals of inertial focusing in microchannels. *Lab Chip* **13**, 1121–1132 (2013).

29. Nivedita, N. & Papautsky, I. Continuous separation of blood cells in spiral microfluidic devices. *Biomicrofluidics* **7**, (2013).
30. Amini, H., Lee, W. & Di Carlo, D. Inertial microfluidic physics. *Lab Chip* **14**, 2739–2761 (2014).
31. Kulasinghe, A., Zhou, J., Kenny, L., Papautsky, I. & Punyadeera, C. Capture of circulating tumour cell clusters using straight microfluidic chips. *Cancers (Basel)*. **11**, 1–11 (2019).
32. Liberale, C. *et al.* Integrated microfluidic device for single-cell trapping and spectroscopy. *Sci. Rep.* **3**, (2013).
33. Karimi, A., Yazdi, S. & Ardekani, A. M. Hydrodynamic mechanisms of cell and particle trapping in microfluidics. doi:10.1063/1.4799787
34. Chien, S. *et al.* Blood viscosity: Influence of erythrocyte aggregation. *Science (80-.)*. **157**, 829–831 (1967).
35. Chien, S., Usami, S., Dellenback, R. J. & Gregersen, M. I. Blood viscosity: Influence of erythrocyte deformation. *Science (80-.)*. **157**, 827–829 (1967).
36. Owen, D. H. & Katz, D. F. A review of the physical and chemical properties of human semen and the formulation of a semen simulant. *Journal of Andrology* **26**, 459–469 (2005).
37. Berret, J. F. Local viscoelasticity of living cells measured by rotational magnetic spectroscopy. *Nat. Commun.* **7**, (2016).
38. Ho, B. P. & Leal, L. G. Migration of rigid spheres in a two-dimensional unidirectional shear flow of a second-order fluid. *J. Fluid Mech.* **76**, 783–799 (1976).
39. Yang, S., Kim, J. Y., Lee, S. J., Lee, S. S. & Kim, J. M. Sheathless elasto-inertial particle focusing and continuous separation in a straight rectangular microchannel. *Lab Chip* **11**, 266–273 (2011).
40. Xiang, N., Ni, Z. & Yi, H. Concentration-controlled particle focusing in spiral elasto-inertial microfluidic devices. *Electrophoresis* **39**, 417–424 (2018).
41. Nam, J., Lim, H., Kim, D., Jung, H. & Shin, S. Continuous separation of microparticles in a microfluidic channel via the elasto-inertial effect of non-Newtonian fluid. *Lab Chip* **12**, 1347–1354 (2012).
42. Xiang, N. *et al.* Fundamentals of elasto-inertial particle focusing in curved microfluidic channels. *Lab Chip* **16**, 2626–2635 (2016).
43. Lee, D. J., Brenner, H., Youn, J. R. & Song, Y. S. Multiplex particle focusing via hydrodynamic force in Viscoelastic Fluids. *Sci. Rep.* **3**, 3–10 (2013).

44. Kumar, T. *et al.* High throughput viscoelastic particle focusing and separation in spiral microchannels. *Sci. Rep.* **11**, 8467 (2021).
45. M.A., W. R. D. XVI. Note on the motion of fluid in a curved pipe. <https://doi.org/10.1080/14786440708564324> **4**, 208–223 (2009).
46. M.A., W. R. D. LXXII. The stream-line motion of fluid in a curved pipe (Second paper). <https://doi.org/10.1080/14786440408564513> **5**, 673–695 (2009).
47. Nivedita, N., Ligrani, P. & Papautsky, I. Dean Flow Dynamics in Low-Aspect Ratio Spiral Microchannels. *Sci. Rep.* **7**, 1–10 (2017).
48. Hur, S. C., Henderson-Maclennan, N. K., McCabe, E. R. B. & Carlo, D. Di. Deformability-based cell classification and enrichment using inertial microfluidics †. doi:10.1039/c0lc00595a
49. Masaeli, M. *et al.* Continuous Inertial Focusing and Separation of Particles by Shape. doi:10.1103/PhysRevX.2.031017
50. Li, M., Muñoz, H. E., Goda, K. & Di Carlo, D. Shape-based separation of microalga *Euglena gracilis* using inertial microfluidics OPEN. doi:10.1038/s41598-017-10452-5
51. Xiang, N. *et al.* Fundamentals of elasto-inertial particle focusing in curved microfluidic channels. *Lab Chip* **16**, 2626–2635 (2016).
52. Seo, K. W., Byeon, H. J., Huh, H. K. & Lee, S. J. Particle migration and single-line particle focusing in microscale pipe flow of viscoelastic fluids. *RSC Adv.* **4**, 3512–3520 (2014).
53. Hulsén, M. A., Villone, M. M., Greco, F., Maffettone, P. L. & D’Avino, G. Particle motion in square channel flow of a viscoelastic liquid: Migration vs. secondary flows. *J. Nonnewton. Fluid Mech.* **195**, 1–8 (2012).
54. Hur, S. C., Choi, S. E., Kwon, S. & Carlo, D. Di. Inertial focusing of non-spherical microparticles. *Appl. Phys. Lett.* **99**, 044101 (2011).
55. Miyamoto, D. T., Ting, D. T., Toner, M., Maheswaran, S. & Haber, D. A. Single-cell analysis of circulating tumor cells as a window into tumor heterogeneity. *Cold Spring Harb. Symp. Quant. Biol.* **81**, 269–274 (2016).
56. Tian, F. *et al.* Label-free isolation of rare tumor cells from untreated whole blood by interfacial viscoelastic microfluidics. *Lab Chip* **18**, 3436–3445 (2018).
57. Liu, C. *et al.* Field-Free Isolation of Exosomes from Extracellular Vesicles by Microfluidic Viscoelastic Flows. *ACS Nano* **11**, 6968–6976 (2017).
58. Seo, K. W., Kang, Y. J. & Lee, S. J. Lateral migration and focusing of microspheres in a microchannel flow of viscoelastic fluids. *Phys. Fluids* **26**, (2014).

59. Liu, C. *et al.* Size-Based Separation of Particles and Cells Utilizing Viscoelastic Effects in Straight Microchannels. *Anal. Chem.* **87**, 6041–6048 (2015).
60. Liu, C. *et al.* Sheathless Focusing and Separation of Diverse Nanoparticles in Viscoelastic Solutions with Minimized Shear Thinning. *Anal. Chem.* **88**, 12547–12553 (2016).
61. Yang, S., Kim, J. Y., Lee, S. J., Lee, S. S. & Kim, J. M. Sheathless elasto-inertial particle focusing and continuous separation in a straight rectangular microchannel. *Lab Chip* **11**, 266–273 (2011).
62. Leshansky, A. M., Bransky, A., Korin, N. & Dinnar, U. Tunable nonlinear viscoelastic ‘focusing’ in a microfluidic device. *Phys. Rev. Lett.* **98**, 234501 (2007).
63. Lim, E. J. *et al.* Inertio-elastic focusing of bioparticles in microchannels at high throughput. *Nat. Commun.* **5**, (2014).
64. Xiang, N. *et al.* Fundamentals of elasto-inertial particle focusing in curved microfluidic channels. *Lab Chip* **16**, 2626–2635 (2016).
65. Kang, K., Lee, S. S., Hyun, K., Lee, S. J. & Kim, J. M. DNA-based highly tunable particle focuser. *Nat. Commun.* **4**, 1–8 (2013).
66. Leshansky, A. M., Bransky, A., Korin, N. & Dinnar, U. Tunable nonlinear viscoelastic ‘focusing’ in a microfluidic device. *Phys. Rev. Lett.* **98**, 1–4 (2007).
67. Kabanov, A. V., Vinogradov, S. V., Suzdaltseva, Y. G. & Alakhov, V. Y. Water-Soluble Block Polycations as Carriers for Oligonucleotide Delivery. *Bioconjug. Chem.* **6**, 639–643 (1995).
68. Otsuka, H., Nagasaki, Y. & Kataoka, K. PEGylated nanoparticles for biological and pharmaceutical applications. *Adv. Drug Deliv. Rev.* **55**, 403–419 (2003).
69. Veronese, F. M. & Mero, A. The impact of PEGylation on biological therapies. *BioDrugs* **22**, 315–329 (2008).
70. Ivanova, R., Lindman, B. & Alexandridis, P. Effect of pharmaceutically acceptable glycols on the stability of the liquid crystalline gels formed by poloxamer 407 in water. *J. Colloid Interface Sci.* **252**, 226–235 (2002).
71. Pal, S., Milano, G. & Roccatano, D. Synthetic Polymers and Biomembranes. How Do They Interact?: Atomistic Molecular Dynamics Simulation Study of PEO in Contact with a DMPC Lipid Bilayer. (2006). doi:10.1021/jp063418d
72. Sackmann, E. Supported membranes: Scientific and practical applications. *Science* (80-.). **271**, 43–48 (1996).
73. Ren, C., Nap, R. J. & Szleifer, I. The role of hydrogen bonding in tethered polymer layers. *J. Phys. Chem. B* **112**, 16238 (2008).

74. Segré, G. & Silberberg, A. Radial particle displacements in poiseuille flow of suspensions. *Nature* **189**, 209–210 (1961).
75. Carlo, D. Di, Edd, J. F., Humphry, K. J., Stone, H. A. & Toner, M. Particle Segregation and Dynamics in Confined Flows. (2009). doi:10.1103/PhysRevLett.102.094503
76. Zhou, J. & Papautsky, I. Resolving dynamics of inertial migration in straight and curved microchannels by direct cross-sectional imaging. *Biomicrofluidics* **15**, 014101 (2021).
77. Martel, J. M. & Toner, M. Particle focusing in curved microfluidic channels. *Sci. Rep.* **3**, 1–5 (2013).
78. Kuntaegowdanahalli, S. S., Bhagat, A. A. S., Kumar, G. & Papautsky, I. Inertial microfluidics for continuous particle separation in spiral microchannels. *Lab Chip* **9**, 2973–2980 (2009).
79. Berger, S. A., Talbot, L. & Yao, L. S. Flow in Curved Pipes. *Annu. Rev. Fluid Mech.* **15**, 461–512 (1983).
80. Bhagat, A. A. S., Kuntaegowdanahalli, S. S. & Papautsky, I. Continuous particle separation in spiral microchannels using dean flows and differential migration. *Lab Chip* **8**, 1906 (2008).
81. Chun, B. & Ladd, A. J. C. Inertial migration of neutrally buoyant particles in a square duct: An investigation of multiple equilibrium positions. *Phys. Fluids* **18**, (2006).
82. Nivedita, N. & Papautsky, I. Continuous separation of blood cells in spiral microfluidic devices. *Biomicrofluidics* **7**, (2013).
83. Ho, B. P. & Leal, L. G. Migration of rigid spheres in a two-dimensional unidirectional shear flow of a second-order fluid. *J. Fluid Mech.* **76**, 783–799 (1976).
84. Ahn, S. W., Lee, S. S., Lee, S. J. & Kim, J. M. Microfluidic particle separator utilizing sheathless elasto-inertial focusing. *Chem. Eng. Sci.* **126**, 237–243 (2015).
85. Liu, C. *et al.* Size-Based Separation of Particles and Cells Utilizing Viscoelastic Effects in Straight Microchannels. *Anal. Chem.* **87**, 6041–6048 (2015).
86. Tian, F. *et al.* Microfluidic co-flow of Newtonian and viscoelastic fluids for high-resolution separation of microparticles. *Lab Chip* **17**, 3078–3085 (2017).
87. Tian, F. *et al.* Label-free isolation of rare tumor cells from untreated whole blood by interfacial viscoelastic microfluidics. *Lab Chip* **18**, 3436–3445 (2018).
88. Lu, X. & Xuan, X. Continuous Microfluidic Particle Separation via Elasto-Inertial Pinched Flow Fractionation. *Anal. Chem.* **87**, 6389–6396 (2015).
89. Lu, X. & Xuan, X. Elasto-Inertial Pinched Flow Fractionation for Continuous Shape-

- Based Particle Separation. *Anal. Chem.* **87**, 11523–11530 (2015).
90. Nam, J. *et al.* Microfluidic device for sheathless particle focusing and separation using a viscoelastic fluid. *J. Chromatogr. A* **1406**, 244–250 (2015).
 91. Nam, J. *et al.* High-throughput malaria parasite separation using a viscoelastic fluid for ultrasensitive PCR detection. *Lab Chip* **16**, 2086–2092 (2016).
 92. Nam, J., Jang, W. S., Hong, D. H. & Lim, C. S. Viscoelastic Separation and Concentration of Fungi from Blood for Highly Sensitive Molecular Diagnostics. *Sci. Rep.* **9**, 3067 (2019).
 93. Cha, S. *et al.* Cell stretching measurement utilizing viscoelastic particle focusing. *Anal. Chem.* **84**, 10471–10477 (2012).
 94. Young Kim, J., Won Ahn, S., Sik Lee, S. & Min Kim, J. Lateral migration and focusing of colloidal particles and DNA molecules under viscoelastic flow. *Lab Chip* **12**, 2807–2814 (2012).
 95. Kang, K., Lee, S. S., Hyun, K., Lee, S. J. & Kim, J. M. DNA-based highly tunable particle focuser. *Nat. Commun.* **4**, 1–8 (2013).
 96. Lee, D. J., Brenner, H., Youn, J. R. & Song, Y. S. Multiplex Particle Focusing via Hydrodynamic Force in Viscoelastic Fluids. *Sci. Rep.* **3**, 3258 (2013).
 97. Mitragotri, S. & Lahann, J. Physical approaches to biomaterial design. *Nat. Mater.* **8**, 15–23 (2009).
 98. Gadêlha, H., Hernández-Herrera, P., Montoya, F., Darszon, A. & Corkidi, G. Human sperm uses asymmetric and anisotropic flagellar controls to regulate swimming symmetry and cell steering. *Sci. Adv.* **6**, eaba5168 (2020).
 99. Son, J. *et al.* Non-motile sperm cell separation using a spiral channel. *Anal. Methods* **7**, 8041–8047 (2015).
 100. Holm, S. H., Beech, J. P., Barrett, M. P. & Tegenfeldt, J. O. Separation of parasites from human blood using deterministic lateral displacement †. doi:10.1039/c0lc00560f
 101. Lu, X., Zhu, L., Hua, R. mao & Xuan, X. Continuous sheath-free separation of particles by shape in viscoelastic fluids. *Appl. Phys. Lett.* **107**, 264102 (2015).
 102. Mukherjee, P., Nebuloni, F., Gao, H. & Zhou, J. Rapid Prototyping of Soft Lithography Masters for Microfluidic Devices Using Dry Film Photoresist in a Non-Cleanroom Setting. (2019). doi:10.3390/mi10030192
 103. Lu, X. & Xuan, X. Continuous Microfluidic Particle Separation via Elasto-Inertial Pinched Flow Fractionation. *Anal. Chem.* **87**, 6389–6396 (2015).

104. Ebagninin, K. W., Benchabane, A. & Bekkour, K. Rheological characterization of poly(ethylene oxide) solutions of different molecular weights. *J. Colloid Interface Sci.* **336**, 360–367 (2009).
105. Kim, J., Hong, S. O., Shim, T. S. & Kim, J. M. Inertio-elastic flow instabilities in a 90° bent microchannel. *Soft Matter* **13**, 5656–5664 (2017).
106. Giesekus, H. A simple constitutive equation for polymer fluids based on the concept of deformation-dependent tensorial mobility. *J. Nonnewton. Fluid Mech.* **11**, 69–109 (1982).
107. Wang, J., Heuer, L. & Joseph, D. Aging properties of semidilute aqueous solutions of polyethylene oxide seeded with silica nanoparticles. *J. Rheol. (N. Y. N. Y.)*. **49**, 1303 (2005).
108. Rodd, L. E., Lee, D., Ahn, K. H. & Cooper-White, J. J. The importance of downstream events in microfluidic viscoelastic entry flows: Consequences of increasing the constriction length. *J. Nonnewton. Fluid Mech.* **165**, 1189–1203 (2010).
109. Bird, R. B. (Robert B. *Dynamics of polymeric liquids*. (Wiley, 1987).
110. Zhou, J. & Papautsky, I. Viscoelastic microfluidics: progress and challenges. *Microsystems Nanoeng.* **6**, (2020).
111. Martel, J. M. & Toner, M. Inertial Focusing in Microfluidics. *Annu. Rev. Biomed. Eng.* **16**, 371–396 (2014).
112. Zhang, J. *et al.* Fundamentals and applications of inertial microfluidics: a review. *Lab Chip* **16**, 10–34 (2015).
113. Li, G., McKinley, G. H. & Ardekani, A. M. Dynamics of particle migration in channel flow of viscoelastic fluids. *J. Fluid Mech.* **785**, 486–505 (2015).
114. Ookawara, S., Higashi, R., Street, D. & Ogawa, K. Feasibility study on concentration of slurry and classification of contained particles by microchannel. **101**, 171–178 (2004).
115. Ookawara, S., Street, D. & Ogawa, K. Numerical study on development of particle concentration profiles in a curved microchannel. **61**, 3714–3724 (2006).
116. Xiang, N., Dai, Q. & Ni, Z. Multi-train elasto-inertial particle focusing in straight microfluidic channels. *Appl. Phys. Lett.* **109**, (2016).
117. Martel, J. M. & Toner, M. Particle focusing in curved microfluidic channels. *Sci. Rep.* **3**, 1–8 (2013).
118. Guan, G. *et al.* Spiral microchannel with rectangular and trapezoidal cross-sections for size based particle separation. *Sci. Rep.* **3**, (2013).
119. Hossain, M. S. *et al.* Flow cytometry for the assessment of animal sperm integrity and

- functionality: state of the art. *Asian J. Androl.* **13**, 406 (2011).
120. Dean, P. N., Pinkel, D. & Mendelsohn, M. L. Hydrodynamic orientation of sperm heads for flow cytometry. *Biophys. J.* **23**, 7–13 (1978).
 121. Huang, H. Y., Huang, P. W. & Yao, D. J. Enhanced efficiency of sorting sperm motility utilizing a microfluidic chip. *Microsyst. Technol.* **23**, 305–312 (2017).
 122. Feng, H. *et al.* High efficiency rare sperm separation from biopsy samples in an inertial focusing device. *Analyst* **146**, 3368–3377 (2021).
 123. Rahi, A., Kazemi, M., Pishbin, E., Karimi, S. & Nazarian, H. Cross flow coupled with inertial focusing for separation of human sperm cells from semen and simulated TESE samples. *Analyst* **146**, 7230–7239 (2021).
 124. Johnson, L. A. & Schulman, J. D. The safety of sperm selection by flow cytometry. *Hum. Reprod.* **9**, 758–759 (1994).
 125. Vazquez, J. M. *et al.* Motility characteristics and fertilizing capacity of boar spermatozoa stained with hoechst 33342. *Reprod. Domest. Anim.* **37**, 369–374 (2002).
 126. Leahy, T. & Gadella, B. M. Sperm surface changes and physiological consequences induced by sperm handling and storage. *Reproduction* **142**, 759–778 (2011).
 127. Bhagat, A. A. S., Kuntaegowdanahalli, S. S. & Papautsky, I. Enhanced particle filtration in straight microchannels using shear-modulated inertial migration. *Phys. Fluids* **20**, 1–4 (2008).
 128. Li, M., Muñoz, H. E., Goda, K. & Di Carlo, D. Shape-based separation of microalga *Euglena gracilis* using inertial microfluidics. *Sci. Reports 2017 71* **7**, 1–8 (2017).
 129. Sperm - Molecular Biology of the Cell - NCBI Bookshelf. Available at: <https://www.ncbi.nlm.nih.gov/books/NBK26914/>. (Accessed: 2nd July 2022)
 130. Armistead, F. J., Gala De Pablo, J., Gadêlha, H., Peyman, S. A. & Evans, S. D. Cells Under Stress: An Inertial-Shear Microfluidic Determination of Cell Behavior. *Biophys. J.* **116**, 1127–1135 (2019).
 131. Connolly, S., McGourty, K. & Newport, D. The in vitro inertial positions and viability of cells in suspension under different in vivo flow conditions. *Sci. Reports 2020 101* **10**, 1–13 (2020).
 132. Fan, R. *et al.* Circulatory shear flow alters the viability and proliferation of circulating colon cancer cells. *Sci. Rep.* **6**, (2016).
 133. Hur, S. C., Choi, S. E., Kwon, S. & Carlo, D. Di. Inertial focusing of non-spherical microparticles. *Appl. Phys. Lett.* **99**, 1–4 (2011).

134. Tran-Cong, S., Gay, M. & Michaelides, E. E. Drag coefficients of irregularly shaped particles. *Powder Technol.* **139**, 21–32 (2004).
135. Juniper, M. P. *Fluid Mechanics 8.1 LIFT AND DRAG*.
136. Li, M. *et al.* Inertial focusing of ellipsoidal *Euglena gracilis* cells in a stepped microchannel. *Lab Chip* **16**, 4458–4465 (2016).
137. Qi, D. & Luo, L. Transitions in rotations of a nonspherical particle in a three-dimensional moderate Reynolds number Couette flow ARTICLES YOU MAY BE INTERESTED IN. *Phys. Fluids* **14**, 4440 (2002).
138. The motion of ellipsoidal particles immersed in a viscous fluid. *Proc. R. Soc. London. Ser. A, Contain. Pap. a Math. Phys. Character* **102**, 161–179 (1922).
139. Prohm, C., Zöller, N. & Stark, H. Controlling inertial focussing using rotational motion. doi:10.1140/epje/i2014-14036-y
140. Said, T. M. & Land, J. A. Effects of advanced selection methods on sperm quality and ART outcome: a systematic review. *Hum. Reprod. Update* **17**, 719–733 (2011).

APPENDIX

Re-Use Permissions

Chapter 2 of this thesis is adapted from my previous publication as Jian Zhou, Prithviraj Mukherjee, Hua Gao, Qiyue Luan, and Ian Papautsky. “Label-free microfluidic sorting of microparticles”. APL Bioeng. 3, 041504 (2019) with permission from APL Bioeng. APL applies the Creative Commons CC BY 4.0 license. Under this license, authors retain ownership of the copyright for their content to reprint and the license is automatically granted.

Figure 2d of this thesis is adapted from previous publication as Sathyakumar S. Kuntaegowdanahalli,^a Ali Asgar S. Bhagat,^a Girish Kumar^b and Ian Papautsky. “Inertial microfluidics for continuous particle separation in spiral microchannels” with permission from Royal Society of Chemistry in APPENDIX 1.

Figure 3 of this thesis is adapted from previous publication as Joseph M. Martel and Mehmet Toner. “ Inertial Focusing in Microfluidics”. Annu. Rev. Biomed. Eng. 2014. 16:371–96 with permission from Annual Review of Biomedical Engineering in APPENDIX 2.

APPENDIX 1

LICENSED CONTENT

Publication Title	Lab on a chip	Publication Type	e-Journal
Article Title	Inertial microfluidics for continuous particle separation in spiral microchannels.	Start Page	2973
Author/Editor	Royal Society of Chemistry (Great Britain)	End Page	2980
Date	01/01/2001	Issue	20
Language	English	Volume	9
Country	United Kingdom of Great Britain and Northern Ireland	URL	http://www.rsc.org/loc
Rightholder	Royal Society of Chemistry		

REQUEST DETAILS

Portion Type	Image/photo/illustration	Distribution	Worldwide
Number of Images / photos / illustrations	1	Translation	Original language of publication
Format (select all that apply)	Electronic	Copies for the disabled?	No
Who will republish the content?	Academic institution	Minor editing privileges?	No
Duration of Use	Life of current edition	Incidental promotional use?	No
Lifetime Unit Quantity	Up to 499	Currency	USD
Rights Requested	Main product		

NEW WORK DETAILS

Title	Viscoelastic and Inertial Focusing of Asymmetric Cells in Spiral Channels	Institution name	University of Illinois Chicago
Instructor name	Hua Gao	Expected presentation date	2022-07-22

ADDITIONAL DETAILS

Order reference number	N/A	The requesting person / organization to appear on the license	Hua Gao/University of Illinois Chicago
------------------------	-----	---	--

REUSE CONTENT DETAILS

Title, description or numeric reference of the portion(s)	Viscoelastic and Inertial Focusing of Asymmetric Cells in Spiral Channels	Title of the article/chapter the portion is from	Inertial microfluidics for continuous particle separation in spiral microchannels.
Editor of portion(s)	Kuntaegowdanahalli, Sathyakumar S.; Bhagat, Ali Asgar S.; Kumar, Girish; Papautsky, Ian	Author of portion(s)	Kuntaegowdanahalli, Sathyakumar S.; Bhagat, Ali Asgar S.; Kumar, Girish; Papautsky, Ian
Volume of serial or monograph	9	Issue, if republishing an article from a serial	20
Page or page range of portion	2973-2980	Publication date of portion	2009-10-20

APPENDIX 2

Order Date 20-Jul-2022
Order License ID 1249502-1
ISSN 1545-4274

Type of Use
Publisher

Republish in a thesis/dissertation
ANNUAL REVIEW OF BIOMEDICAL
ENGINEERING
Image/photo/illustration

Portion

LICENSED CONTENT

Publication Title	Annual review of biomedical engineering	Rightsholder	Annual Reviews, Inc.
Date	01/01/1999	Publication Type	e-Journal
Language	English	URL	http://arjournals.annualreviews.org/loi/bi...
Country	United States of America		

REQUEST DETAILS

Portion Type	Image/photo/illustration	Distribution	Worldwide
Number of images / photos / illustrations	1	Translation	Original language of publication
Format (select all that apply)	Electronic	Copies for the disabled?	No
Who will republish the content?	Academic institution	Minor editing privileges?	No
Duration of Use	Life of current edition	Incidental promotional use?	No
Lifetime Unit Quantity	Up to 499	Currency	USD
Rights Requested	Main product		

NEW WORK DETAILS

Title	Viscoelastic and Inertial Focusing of Asymmetric Cells in Spiral Channels	Institution name	University of Illinois Chicago
Instructor name	Hua Gao	Expected presentation date	2022-07-22

ADDITIONAL DETAILS

Order reference number	N/A	The requesting person / organization to appear on the license	Hua Gao/University of Illinois Chicago
------------------------	-----	---	--

REUSE CONTENT DETAILS

Title, description or numeric reference of the portion(s)	Viscoelastic and Inertial Focusing of Asymmetric Cells in Spiral Channels	Title of the article/chapter the portion is from	Inertial Focusing in Microfluidics
Editor of portion(s)	n/a	Author of portion(s)	Joseph M. Martel and Mehmet Toner
Volume of serial or monograph	16:371-396	Issue, if republishing an article from a serial	N/A
Page or page range of portion	372-392	Publication date of portion	2014-05-29

VITA

NAME: Hua Gao

EDUCATION: B.A., Biomedical Engineering, University of Cincinnati, Cincinnati, Ohio, 2016
M.S., Electrical Engineering, University of Cincinnati, Cincinnati, Ohio, 2016
Ph.D., Biomedical Engineering, University of Illinois Chicago, Chicago, Illinois, 2022

TEACHING: Department of Bioengineering, University of Illinois Chicago, Bioinstrument, 2017 and 2018
Department of Bioengineering, University of Illinois Chicago, Bioinstrument Lab, 2019
Department of Bioengineering, University of Illinois Chicago, Biomaterials, 2021

HONORS: Pre-doctoral Education for Clinical and Translational Scientists Program Award, 2020

PROFESSIONAL MEMBERSHIP: Center for Advanced Design and Manufacturing of Integrated Microfluidics

ABSTRACTS: H.Gao, J. Zhou, and I. Papautsky, “Effects of particle size and fluid elasticity on elasto-inertial migration in spiral channel,” 24th International Conference on Miniaturized Systems for Chemistry and Life Sciences (MicroTAS 2019), Online, October 2020

H. Gao, J. Zhou, and I. Papautsky, “Lateral focusing in viscoelastic flow in spiral channels,” 23th International Conference on Miniaturized Systems for Chemistry and Life Sciences (MicroTAS 2019), Basel, Switzerland, October 2019

H. Gao, J. Zhou, and I. Papautsky, “Microfluidic Chips for Cell Positioning and Alignment,” Center for Advanced Design and Manufacturing of Integrated Microfluidics (CADMIM), Chicago, IL, September 2019

X. Wang, H. Gao, and I. Papautsky, “Sheath-flow-aided inertial microfluidic cell sorter for high-throughput blood sorting,” 20th International Conference on Miniaturized Systems for Chemistry and Life Sciences (MicroTAS 2016), Dublin, Ireland, October 2016

PUBLICATIONS: H. Gao, J. Zhou, M. Naderi, Z. Peng, I. Papautsky, “Evolution of Focused Streams in Viscoelastic Flow in Spiral Microchannels”, *Microsystem&Nanoengineering*, 2022.

F. Amadeo, P. Mukherjee, H. Gao, J. Zhou, I. Papautsky, “Polycarbonate Masters for Soft Lithography”, *Micromachines* 2021,12 (11),1392

J. Zhou, P. Mukherjee, H. Gao, Q. Luan, and I. Papautsky, “Label-free microfluidic sorting of microparticles,” *APL Bioengineering*, 2019,3,041504

P. Mukherjee, F. Nebuloni, H. Gao, J. Zhou, and I. Papautsky, “Rapid prototyping of soft lithography masters for microfluidic devices using dry film photoresist in a non-cleanroom setting,” *Micromachines*, 2019, 10(3), 192.

X. Wang, H. Gao, N. Dindic, N. Kaval, and I. Papautsky, “A low-cost, plug-and-play inertial microfluidic helical capillary device for high throughput flow cytometry,” *Biomicrofluidics*, 2017, 11(1).

PATENT: I. Papautsky, H. Gao, J. Zhou, and G. Kamalakshakurup, “Microfluidic system and method.” Filed March 15, 2022. Appl. No. 63/320,1